Shape and Reflectance Estimation from Dielectric Materials using Statistical Analysis and Polarisation

Lichi Zhang

Submitted for the degree of Doctor of Philosophy

University of York

Department of Computer Science

October 2012

Abstract

Polarisation has proven to be an effective method in the analysis of light reflection in computer vision. It plays an important role in separating reflectance components using cross polarisation settings. Some polarisation based methods have also been presented in the literature for surface orientation estimation, where the incident light is unpolarised.

This thesis aims at exploiting the polarising properties of surface reflection for computer vision applications. In particular, we focus on developing a framework for measuring the shape and reflectance information based on polarisation data. The polarised images are acquired using simple and low-cost devices, and the estimates are satisfactory compared with other surface characteristic methods such as shape from shading and stereo approaches. Statistical methods are also used to aid the computations, such as blind source separation (BSS), mutual information estimation, the iterated conditional modes method, etc.

Chapter 2 surveys the related literature in the fields of polarisation, reflectance function analysis, shape recovery, and pattern recognition. We also discuss other shape recovery techniques, such as shape from shading, photometric stereo, and geometric stereo. We make comparisons between these approaches to show their advantages and drawbacks.

In Chapter 3, we introduce the method of BSS, and show how to incorporate it into polarisation state estimation. The traditional method of using polarisation models for shape recovery and polarisation state estimation usually requires more than three images, normally 10 or more pictures in different polarisation angles. The proposed method solves these problems, and provides a robust way to measure polarisation state and refractive index information using only three images, and without the need to have polarisation angle information. We also demonstrate in the experimental section that the estimates using the proposed method offer significant improvements over existing polarisation based

approaches.

In Chapter 4, we extend the work in the Chapter 3 in a number of ways. Firstly, we present detailed review of the Fresnel theory in polarisation vision, and propose a novel polarisation model which considers both diffuse and specular reflections. Secondly, we develop a new novel criterion functions to be used in the Chapter 3, which improves its robustness and accuracy.

In Chapter 5, we also explore the shape recovery method using the polarised light. When the polarised light is transmitted through the polariser, it becomes fully polarised. The specular reflection part can be fully eliminated using the setting of "cross-polarisation". In this case the methodology is changed accordingly. This leads us to develop a new framework which firstly uses BSS for reflectance component separation, and then applies a polarisation model built specifically for this case. The polarisation model is based on Fresnel equation and Malus's law, which describes the reflection of polarised light when transmitting through the polariser in front of the viewer. It is also noted that the proposed framework reduces the noise in the zenith angle estimate, which we demonstrate in the experiments.

In Chapter 6 we consider an alternative way to estimate shape and reflectance properties using polarised light. Using the separated diffuse and specular reflection components obtained in Chapter 5, we use parametric reflectance models, that relate the reflectance intensity with the zenith angle when the parameter values are given. The reflectance models are only applied for either diffuse or specular reflections, and the two zenith angle estimates from the two components should be identical as they describe the same object. We use mutual information estimation and Newton's method to find their similarities and their parameter values measured by model fitting. The two estimates then are combined using a mixture model. We choose six reflectance models and compare their performance in this framework.

Contents

List of Figures

List of Tables

Acknowledgements

In my four years of PhD research there have been so many people who have supported me, guided me and helped me to conquer all the troubles and share laughs and happiness. Firstly I would like to express my great and sincere appreciation to my supervisor, Prof. Edwin R. Hancock, whose excellent guidance in academic research and paper writing is the main reason why I have been able to complete my PhD, and have carried out all these research. The knowledge I have learned from him will surely be very valuable in my future career. I would also like to thank my assessor Dr. William Smith for his great support in the field of shape recovery and reflectance estimation. I appreciate it very much that every time I come to his office for guidance, he is always kind and helps me sincerely.

I would also like to thank Dr. Gary Atkinson and Dr. Gule Saman for sharing their knowledge in polarisation with me, and correcting my mistakes in the study of polarisation vision. Dr. Peng Ren, Dr. Rui Huang and Dr. Jing Wu have given me much advice on studying and living in the UK, which I am very grateful for. My thanks also go to Filo Ottaway who helped me a lot in the PhD application, she is a very responsible academic secretary and I wish her luck in the future. I have made many friends in these four years, some of them have already left the UK, but I will not forget the joys and great memories.

Finally I would like to thank my parents for their kindness and help in supporting my study. The online chat with them every week has been the best medicine in curing my pressures in these years.

Declaration

I declare that the research described in this thesis is original work, which I undertook at the University of York during 2008 - 2012. Except where stated, all of the work contained within this thesis represents the original contribution of the author.

I declare that all the work in this thesis is solely my own, except where attributed and cited to other authors.

List of Publications

Journal Paper

- Lichi Zhang, Edwin R. Hancock: Robust Estimation of Shape and Polarisation using Blind Source Separation, Pattern Recognition Letters, 2013

Workshop and Conference Paper

- Lichi Zhang, Edwin R. Hancock, Jing Wu: Estimating Surface Characteristics and Extracting Features from Polarisation, SPR, 2012, **oral**
- Lichi Zhang, Edwin R. Hancock: Simultaneous Reflectance Estimation and Surface Shape Recovery Using Polarisation, ICPR, 2012
- Lichi Zhang, Edwin R. Hancock: A Comprehensive Polarisation Model for Surface Orientation Recovery, ICPR, 2012, **oral**
- Lichi Zhang, Edwin R. Hancock: Robust Shape and Polarisation Estimation using Blind Source Separation, CAIP, 2011
- Lichi Zhang, Edwin R. Hancock, Gary Atkinson: Reflection Component Separation using Statistical Analysis and Polarisation, IbPRIA, 2011

Chapter 1

Introduction

Accurately estimating and reproducing surface appearance is a task of pivotal importance in computer vision and graphics. Applications include the analysis and classification of surfaces based on estimates of the physical properties of the materials, and the rendering of realistic images from the estimates. The appearance of surfaces is determined by shape, colour and reflectance [36]. These intrinsic surface properties are independent of each other and affect the observed image intensity in a complicated way. There have been a number of attempts in the literature aimed at accurately measuring surface shape and reflectance. Many existing reflectance estimation methods are limited by their requiring high cost measurement systems, and a large number of input images. The direct measurement of the BRDF requires a gonioreflectometer [60]. The typical model is designed by Murray-Coleman and Smith, which is shown in Figure 1.1. It is cumbersome to use and quite expensive, so few facilities in the world can afford it.

Other available methods use complicated devices such as light stages and geometric domes to build reflectance functions from image intensity variations under different light source directions [25]. Recently Ma *et al.* [64] presented a method to estimate surface normal maps of an object using four spherical gradient illumination patterns from either diffuse or specular reflectance components. The technique relies on structured light, and hence adds scanning time and system complexity to the overload.

For shape reconstruction there are shape from shading [45], shape from focus [48], shape from texture [101], photometric stereo [37], geometry stereo [10], etc. Shape from shading and stereo methods are widely used in shape recovery, but they have drawbacks

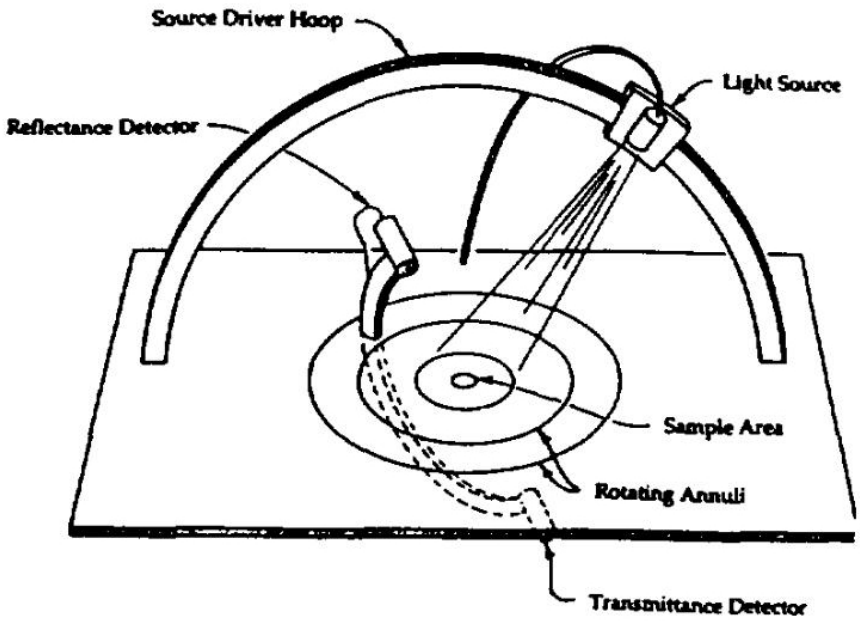

Figure 1.1: The gonioreflectometer having movable light source and photometer [60].

which make them unsuitable for our work. Shape from shading is proved to be an ill-posed problem, requires many constraints on input images to ensure the robustness of the performance, and is known to produce poor estimates. Stereo techniques, such as LiDAR, Mesa and Kinect, require complicated algorithms support, and special acquisition devices which are usually high cost.

In this thesis we consider polarisation methods for shape and reflectance estimation, as it is relatively simple for acquisition and estimation, and can produce fairly decent results, as shown in [2]. Our goal here is to investigate the polarisation vision and employ statistical methods into the traditional ways of shape from polarisation, which can improve the robustness and accuracy of the estimation.

1.1 Polarisation

The polarisation of light is one of the wave properties which describes oscillation directions of the particles [46]. It was first discovered by the mathematician Étienne-Louis Malus in 1808, who also developed Malus's law introduced in Chapter 5. In our daily life many lights are partially or fully polarised, though we are unable to observe it since human eyes are insensitive to this phenomenon. Figure 1.2 shows the transmission of a

light ray through a linear polariser. When the polariser is rotated to a specific orientation, part of the light whose wave orientation is perpendicular to the polariser angle is blocked.

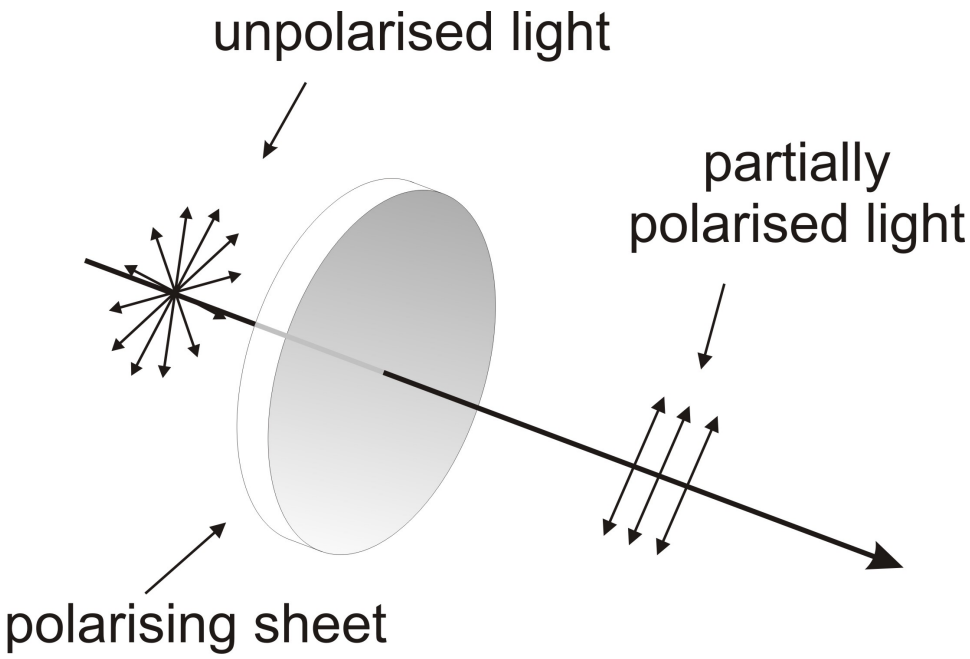

Figure 1.2: Transmission of a light-wave through a linear polariser.

The best known application of polarisation technology is polarised sunglasses based on the principles of Brewster's angle, which are made of one linear polarisation filter set in vertical direction. As the wave vibration directions of most lights that make people glare are horizontal, therefore it is blocked by the sunglasses, and protect the eyes from harmful sunshine.

Polarisation is also widely applied in photography, in which the photographers usually use a polariser to eliminate specularity glare from the surfaces, such as water or other non-metallic objects. There are two types of polarisers: linear and circular, which transform unpolarised light into linearly and left-handed circularly polarised light, respectively. These two different kinds of light can hardly be distinguished by the human eyes. Figure 1.3 shows the effect when using a polariser, which is quite useful when a photographer wants to eliminate specularities from the lake and make the scene under the water visible.

In academic domains, polarisation is applied as a measurement tool in the research areas of astronomy, optics and crystallography [116]. The first contribution of polarisation to computer vision was proposed by Koshikawa in [57], in which the underlying physics

(a) Unpolarised Image

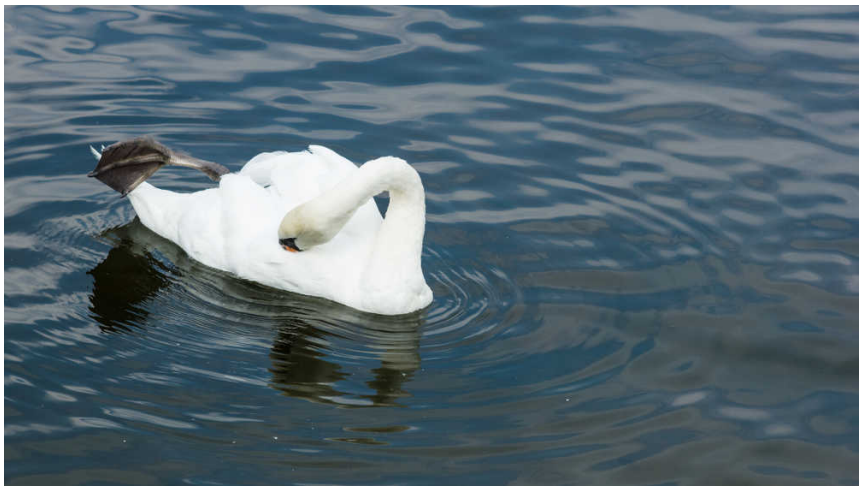

(b) Polarised Image

Figure 1.3: Difference between images that are taken with or without polariser. Brightness in (b) is adjusted to show that the specularity of the lake is removed and the stones underneath become visible.

of polarisation imaging is outlined. Koshikawa developed a polarisation reflectance model for measuring shape based on Mueller calculus and the Stokes vectors.

Later, Wolff and Boult developed the Fresnel reflectance model for polarisation vision. It is based on the Fresnel theory, which predicts the way in which polarised light interacts with surface layers [117]. For dielectrics, polarisation may arise in two different ways. In the case of specular polarisation, initially polarised light is reflected in the specular direction. For diffuse polarisation, initially unpolarised light is refracted into the surface and then re-emitted, thereby acquiring a degree of spontaneous polarisation. In both cases, the zenith angle of the reflected or re-emitted light is constrained by the degree of polarisation, and the azimuth angle is constrained by the phase angle. Figure 1.4 shows the diagram of the azimuth and zenith angle with respect to the surface of the object. The azimuth angle of the surface normal is the angle between the direction of surface normal projection onto the image plane and a selected reference direction, whose value ranges from 0° to 360°. The zenith angle, on the other hand, is the angle between the surface normal and the viewing direction, the range is from 0° to 90°.

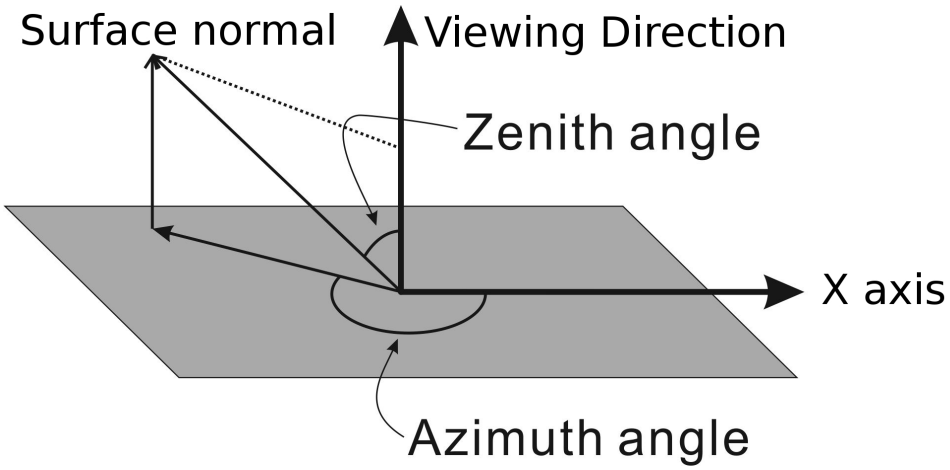

Figure 1.4: The diagram of the zenith and azimuth angle.

However, there are several problems for polarisation based methods: firstly, they require several polarised images taken in different polariser orientations, meaning the inputs are acquired at different times, which becomes problematic when measuring human faces and palms that are not static. The problem is exacerbated as the existing shape from polarisation methods usually needs more than 10 pictures to achieve robustness against noise from CCD sensor of camera or other factors. [71].

It is noted that in this thesis we proposed a blind source separation algorithm in Chapter 4 which requires only three input images for the polarisation estimation. In the experimental section we demonstrate its robustness. There are six polarised images in all for the selected objects, whose polariser angles are 0, 30, 60, 90, 120 and 150 degrees. We select three images as input for the method and check if the results are stable. We have tested all combination and the results are presented in Figure 4.11. The phase angles results are stable, the difference are mainly caused by noise in the input image but they are sufficient for process of shape recovery and other computer vision applications. In the future work we will also concentrate on testing its robustness by running parallel optical channels in the camera.

Secondly, there are two ambiguity issues that have to be resolved in the computation: the first is for the specular Fresnel model, which has two zenith angle solutions corresponding to one DOP value; the second is the phase angle ambiguity which is described in Chapter 6. Thirdly, the problem of reflectance estimation using polarisation is rarely addressed. Atkinson and Hancock [4] proposed a method for reflectance function estimation, but it only considers the diffuse Fresnel model and is only applied for constant-albedo Lambertian surfaces.

1.2 Contribution

This thesis presents research on reflectance and shape estimation using polarisation. The material of objects under study is assumed to be dielectric, and the surface is optically smooth, its albedo is uniform. We have developed frameworks when the incident light is polarised or unpolarised, using statistical methods to aid the process of computation, which can solve the problems outlined in the last section.

The polarisation methods we propose are aimed at incorporating blind source separation (BSS) into the polarisation estimation. The traditional method of using a polarisation model on shape recovery and polarisation state estimation usually requires more than three images, normally 10 or more pictures in different polarisation angles, whose values should also be known. The proposed method solves these problems, and provides a robust way to measure the polarisation state and refractive index value using only three images,

and without the need to have information about the polarisation angles. We use the BSS method in Chapter 3 and Chapter 5, and the criterion functions are built accordingly to the polarisation vision theory.

Next, we show how to cast the problem of shape from polarisation from the degree of polarisation (DOP) estimates. According to dichromatic theory there are two reflection types: diffuse and specular. Existing polarisation models are created based on these two reflectance, but they both have advantages and weaknesses. In Chapter 4, we present a novel polarisation model that considers both types and combines them together using a mixture model. In Chapter 5, as the incident light is polarised, we develop another polarisation model based on Malus's Law, and show in this case that the noise is also reduced.

In this thesis we have provided shape and reflectance estimation frameworks for two cases: using unpolarised or polarised incident light. When the light source produces unpolarised light, the viewer will observe reflected light from the object which is partially polarised. The zenith angle can be estimated using traditional Fresnel reflectance models, and the specularity generally can hardly be eliminated. On the other hand, if the incident light is polarised before being reflected from the surface, it will become fully polarised, the highlight is eliminated using cross-polarisation settings, and existing Fresnel reflectance models cannot be used directly for shape recovery. In Chapter 3 and Chapter 4 we focus on the case using unpolarised light, while in Chapter 5 and Chapter 6 we use polarised incident light instead, and blind source separation method is applied for reflectance component separation.

We have also developed a novel two-step method for reflectance parameter estimation in Chapter 6. In the first step, we determine the parameter values for the diffuse and specular reflectance models. In the second step we use a probabilistic framework to recover the shape from the estimated reflectance components. We make comparisons between six parametric reflectance models to decide which are the most suitable for the framework. We also present two applications that utilise the estimation results: one is to observe the reflectance properties variance on the surface, and the other is to use the estimates for feature extraction.

1.3 Thesis Outline

The remainder of this thesis is organised as follows:

In Chapter 2 we provide an overview of the relevant literature, which covers a number of research fields: polarisation, blind source separation, reflectance modelling, and statistical methods. We also discuss other shape recovery techniques, such as shape from shading, photometric stereo and geometric stereo. We compare these approaches to show their advantages and drawbacks.

In Chapter 3 we introduce the method of blind source separation (BSS), and show how to incorporate it into polarisation state estimation. In order to find accurate results in a fast way, we consider Newton's method for the iterative process, which guarantees rapid (quadratic) convergence. We also demonstrate in the experimental section that the method offers significant improvements over existing polarisation algorithms.

In Chapter 4 we extend the work in Chapter 3 in a number of ways. Firstly, we present a detailed review of the polarisation vision theory, and propose a novel polarisation model which consider both diffuse and specular reflections. Secondly, we provide an improved criterion function of Newton's method based on a different strategy in Chapter 3, which solves the problems of the BSS method introduced in Chapter 3, and its robustness and accuracy has also been improved.

In Chapter 5, we also explore the shape recovery method using the polarised light. When the polarised light is transmitted through the polariser, it becomes fully polarised. The specular reflection part can be fully eliminated using the setting of "cross-polarisation". In this case the methodology is changed accordingly. This leads us to develop a new framework which firstly uses BSS for reflectance component separation, and then applies a polarisation model built specifically for this case. The polarisation model is based on Fresnel equation and Malus's law, which describes the reflection of polarised light when transmitting through the polariser in front of the viewer. It is also noted that the proposed framework reduces the noise in the zenith angle estimate, which we show in the experiments.

In Chapter 6 we consider an alternative way to estimate shape and reflectance properties using polarised light. Using the separated diffuse and specular reflection components obtained in Chapter 5, we employ parametric reflectance models, that relate the

reflectance intensity to the zenith angle when the parameter values are given. The reflectance models are only applied to either diffuse or specular reflections, and the two zenith angle estimates from the two components should be identical as they describe the same object. We use mutual information estimation and Newton's method to find their similarities and their parameter values measured by model fitting. The two estimates then are combined using a probabilistic model. We choose six reflectance models and compare their performance in this framework.

Chapter 7 gives the conclusion of the thesis. A brief summary is presented on the introduced approaches, and we mention some applications that can use the proposed methods, and improvements which can be achieved based on this thesis.

Chapter 2

Literature Review

In this thesis, our goal is to develop frameworks which recover shape and reflectance properties using polarisation and statistical methods. The optic properties of polarisation become different when the incident light is polarised or unpolarised. We present two corresponding methodologies for the estimation. In Chapter 3 and Chapter 4 we show the approaches using unpolarised light, whilst in Chapter 5 and Chapter 6 the proposed methods use images taken under polarised light. In this chapter, we focus on the literature of polarisation vision in shape recovery, and present a survey of the existing literature that is involved in this thesis.

We commence in Section 2.1 with a brief introduction of polarisation and its theory in computer vision domain. In Section 2.3 we give details of current shape reconstruction techniques and the related references. In Section 2.4 we provide literature related to reflectance functions and modelling. In Section 2.5 we show the overviews of three statistical methods, that are widely used in this thesis, which are blind source separation, mutual information estimation and maximum *a posteriori* method.

2.1 Polarisation Light and Vision

In computer vision, polarisation is mainly recognised as a tool to separate reflectance components. When the incident light is polarised, the specular reflection will maintain the polarisation state, while the diffuse component that is scattered underneath or in the surface will be depolarised. Therefore, the two reflectance components can be separated

using two images acquired in the cross polarisation setting [25]. The first image is obtained by placing a vertical polariser on the light source and a horizontal polariser in front of the camera, while the second one is taken by placing both vertical polarisers on the two devices. The specularities in the first image will have only diffuse component without specularities, and the specular component can be calculated by the comparison of the two images. The effect of using cross polarisation setting is shown in Figure 2.1.

It is noted that Fresnel theory also plays an important role when the incident light is polarised, as the brightness of the image is also related to the surface normal information and refractive index value. Therefore in Chapter 5 we propose a novel polarisation model which includes the Fresnel coefficients and Malus's law, that describes the properties when polarised light is reflected from the surface of objects. Diffuse and specular reflection types of Fresnel magnitudes are included in the model as both cannot be negligible when using polarised light. Full details of the model can be found in Chapter 5, which describes the relationship between degree of polarisation value, zenith angle and refractive index information in Equation 5.11.

Nayar *et al.* [71] provided an algorithm for the separation of specular and diffuse reflections from images. The method adopts both techniques in color detection and polarisation to improve robustness. Ma *et al.* [64] utilised the method of polarisation in a higher level by using four spherical gradient illumination patterns to estimate surface normal maps apart from reflectance. They also presented two polarised lighting techniques, which allowed the diffuse and specular normal maps of an object to be measured independently.

Polarisation can also be applied to infer information concerning the reflectance properties of surfaces. For instance, Atkinson and Hancock have shown in [7] how diffuse polarisation can be used to estimate the bidirectional reflectance function. However, their method is computationally demanding, using simulated annealing to estimate the BRDF.

There have been a number of attempts in the literature, aimed at surface orientation estimation of objects using polarisation, where the incident light is unpolarised. The specular and diffuse reflections from the objects become partially polarised, and their values analysed by placing a linear polariser in front of the camera and rotating its orientation. Such effects can be exploited for shape recovery, which was first studied by Koshikawa

(a) full specularity highlights

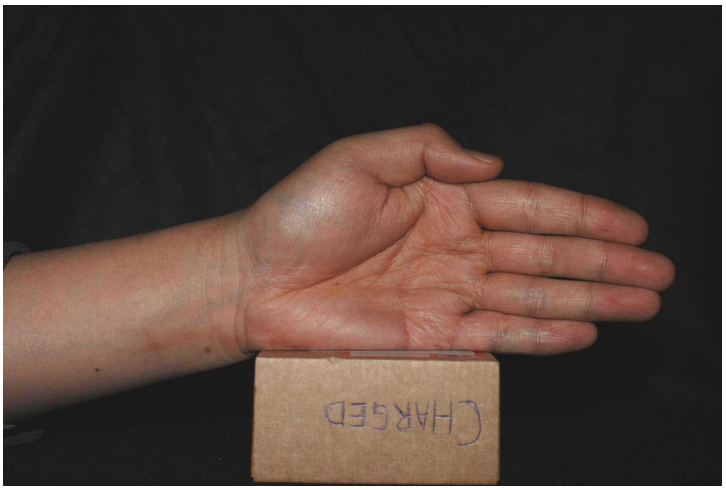

(b) highlight removed

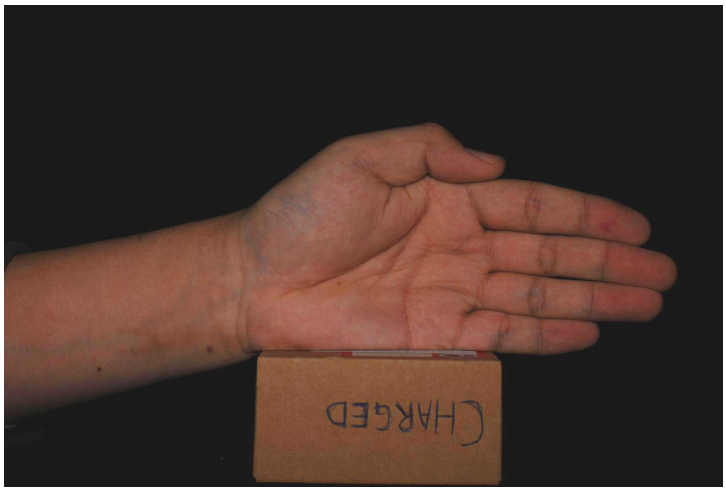

Figure 2.1: The images of human palm, the first image has both specular and diffuse reflections, while the other image has its specularities removed using cross polarisation setting.

in [57]. He proposed a polarisation model based on Mueller calculus. The method is complicated and requires circular polarised incident light. In early days of polarisation vision Stokes vector is also used to represent the polarisation state, which has four components: image intensity, degree of polarisation, phase angle and circular polarisation [43]. The last parameter is negligible for most situations, and is not considered in this thesis [2]. Currently, Fresnel theory is widely used for shape from polarisation, since the zenith angle of the reflected or re-emitted light can be constrained by the degree of polarisation, and the azimuth angle can be computed from the phase angle. Compared with the early work, methods based on Fresnel theory do not require circularly polarised lights and the use of Mueller calculus. Section 2.2.3 provides summary of the approaches that apply Fresnel theory for shape from polarisation.

The main problem of polarisation methods is the number of input images and the time spent for acquisition and calibration. Using a digital camera and a linear polariser, three or more images with different polariser orientations are needed [71]. The images must be in alignment, and this can be difficult to achieve if the object under study is not static. This problem is exacerbated for human subjects. One of the solutions to this problem is to construct purpose built polarisation cameras which shorten the image acquisition time [116] and by using PLZT (Polarised Lead Zirconium Titanate) devices [94]. In this thesis we focus on solving the problem by reducing the number of images requried for the measurement to three, which can also shorten the time of image acquisition.

2.2 Fresnel Theory

In this section, we present a thorough overview of Fresnel theory, which was firstly used in polarisation by Wolff and Boult to describe the direct reflection of electromagnetic waves with the given polarisation state of the incident light [117]. The technique is developed based on Fresnel reflection, which was discovered by Augustin-Jean Fresnel in 1819 for predicting reflection and refraction properties of light moving through different materials [56]. Here we start by introducing refractive index, which is one of the important concepts in Fresnel theory. Then we explore the theories of reflection and refractive rays that are relevant to Fresnel theory, and the approaches that apply Fresnel theory to shape from

polarisation.

2.2.1 Refractive Index

Refractive index is the ratio of the light's speed when it is transmitted from one medium to the other. The value of the refractive index is theoretically constant for all points in the surface, which generally ranges from 1 to 2.5. It is noted that the vacuum has the refractive index of 1, theoretically there is no known media whose value is less than 1. Refractive index varies in different wavelengths of incident light, and temperatures of the observed materials. According to [75] the refractive index value can be regarded as a complex number, its imaginary part represents the amount of light loss from material absorption during refraction. In this thesis we only discuss the real part of the refractive index, and ignore the influences of wavelength and temperature factors.

When the refractive index is measured, its value can be used for the process of material identification, surface shape estimation using Fresnel equations, and image rendering in computer graphics. However, the problem of estimating refractive index is rarely addressed in computer vision and image analysis. The measurement is particularly complicated when the shape of an object is not planar and surface normal has to be obtained beforehand [90]. Existing methods can be found in [91] and [40]. Tominaga and Tanaka [104] measured the refractive index using the Phong model. Later they proposed another estimation method in [105] which obtains the refractive index value on specular highlights from different illumination and viewing directions. The method requires high-cost devices and therefore cannot be implemented in our work.

Another attempt was addressed by Atkinson and Hancock [3], who used a refractometer for refractive index estimation. During acquisition the device emits a laser light to the object, which is reflected, then transmitted through a linear polariser and projected upon a white screen. When the incident light direction is equal to the Brewster angle, denoted as θ_B, the reflected light disappears as it is blocked by the polariser. The refractive index value can be computed from the Brewster angle using Snell's law $n = \tan\theta_B$, which is introduced in the next section. The work of Saman and Hancock [90] focuses on using photometric stereo, and assumes that the value of the refractive index is variable for different locations on the surface. The approach requires 19 images for each object, which

is not suitable in our works.

Recently, we have proposed a blind source separation framework for estimating polarisation in [123, 124], which can also be used in recovering refractive index value. The estimate is sensible for smooth objects such as plastic and fruit. However, the value becomes underestimated when the material of surfaces is sponge and plaster, as the degree of polarisation value is reduced by their roughness. We show the details of BSS approach in Chapter 3 and Chapter 4.

2.2.2 Refraction and Reflection

When the light arrives at a surface, part of its energy is reflected back to the air while the rest penetrates through the surface. The energy proportion of reflection and transmission can be predicted by Fresnel theory. The foundation of this theory is the Fresnel coefficients $r_\perp$ and $r_\parallel$, which has two components representing the lights that are perpendicular and parallel to the plane of incidence respectively. Given the refractive index values of a surface's medium, the reflection and transmission coefficients are computed with the aid of Snell's law. The Fresnel reflection model is created by the Fresnel coefficients with the degree of polarisation value, which can be applied for surface estimation.

Most of the lights from natural illumination are unpolarised, their wave oscillation directions are randomly distributed [43]. The two Fresnel coefficient values are identical for unpolarised light. The reflected light is partially polarised, which is a superposition of two parts. One remains unpolarised while the rest becomes fully polarised. The oscillation directions of waves for fully polarised light are identical and related to the azimuth angle of the surface normal. The orientation can be measured using a linear polariser, so that only part of the light which fits a particular polarisation state can be transmitted through the device.

The reflection and refraction of incident light when impinging on a surface is shown in Figure 2.2. It is noted that denote ψ_i and ψ_t as the incident and transmitted angles, the incident linearly polarised light can be fully transmitted through the medium with no reflections when it follows $\psi_i + \psi_t = 90^\circ$ [52]. Such an indent angle is equal to Brewster's angle [28], which can be estimated using Snell's law. Snell's law, also called the law of refraction, is used for predicting the incidence and refraction angle with the refractive

index values of the media under study [12]. The equation is given as follows:

$$n_i \sin \psi_i = n_t \sin \psi_t \tag{2.1}$$

where refractive index n_i and n_t represent the media of air and transmitted surface respectively. When the incident light is in the air, we can assume $n_i \approx 1$. Substituting $\psi_i + \psi_t = 90^\circ$ into Equation 2.1, the equation is rewritten as

$$\tan \psi_i = n_t \tag{2.2}$$

where it is concluded that the Brewster's angle ψ_B can be estimated from the refractive index value of surface's medium, using $\psi_B = \arctan n_t$.

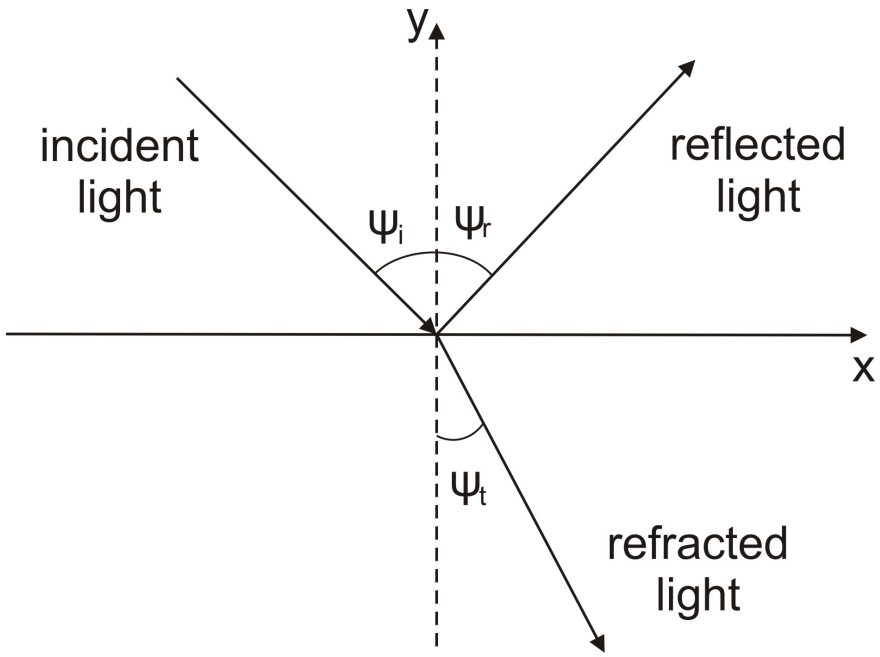

Figure 2.2: The incident, reflected and refracted rays.

2.2.3 Shape Estimation

One of the main contributions in this thesis is to propose novel frameworks for shape from polarisation based on Fresnel theory. In this section we presents a survey of the existing literature in the above field, and discuss their advantages and limitations. There are two common aspects in the recently published works on shape from polarisation methods [2].

Firstly, polarisation state is measured by several input images taken on different polariser angles. The intensity of the polarised image is changed by rotating a linear polariser placed in front of the digital camera, or liquid crystals as introduced in [116]. Secondly, "the phase of polarisation takes a central role" for the convenience of polarisation estimation.

According to [3] Fresnel theory can be applied to both diffuse and specular reflection types. Currently, there are two Fresnel polarisation models. These have been developed based on their corresponding reflection properties. Details of these two equations are presented in Chapter 4. The specular reflection is observed as a highlight area which does not occur across the whole surface. Therefore a special device is needed during image acquisition for the specular polarisation method. Saito *et al.* [88] resolve this problem by placing the subject inside a spherical diffuser, which is illuminated by several external lights in all directions. This ensures that the object receives the incident lights which are diffused by the device, and specularities are occured across the whole surface.

Another issue for shape from specular polarisation is that there is an ambiguity problem when measuring the zenith angle information. Wolff recovers the shape by combining the polarisation information from two views [115], Atkinson and Hancock [5] introduced a novel framework which solves the ambiguity problem with the aid of reflectance function analysis and image processing techniques, and doesn't require "salient surface features to obtain correspondence". The work of Miyazaki *et al.* [68] also takes pictures from two different views and compares their polarisation data. The method is applied for transparent surface, which is highly useful as shape information from transparent material is particularly hard to be estimated when using other shape recovery methods, such as SFS and stereo. Some geometric stereo techniques are also employed to improve estimation accuracy.

Diffuse reflection is occurred when the light that arrives at the surface is not reflected back directly, but re-emitted after several internal scattering in the surface. Compared with the method described above, the advantage of shape from diffuse polarisation method is that only a standard linear polariser, a light source and a standard camera are needed during image acquisition. Besides, the diffuse Fresnel model is much simpler and does not have the issue of the ambiguity problem. Early development includes the work of Wolff

and Boult in [117], which demonstrated how the diffuse polarisation model is applied in determining the surface orientation, especially in the part near the limbs of the objects under study.

Miyazaki *et al.* [69] proposed a systematic framework which measures shape, reflectance and texture map from the object under investigation. Firstly the surface normal is estimated from the degree of polarisation values using the Fresnel model, then the reflectance is measured using the simplified reflectance models and shape estimates. They also introduced an algorithm which computed a shading-free texture map based on the works of Tan *et al.* [102]. However, the framework requires large number of polarised images, and constraints are imposed in reflectance estimation process. Drbohlav and Sara [29] also proposed an approach using diffuse polarisation but the methodology lacks credibility as the experimental object presented is only a single opaque sphere. Atkinson and Hancock [3] introduced a shape from diffuse polarisation method which is similar to the works of Miyazaki *et al.* . However, it considers the inter-reflection phenomenon on the surface which is of significance for shape recovery, whilst in [69] it is ignored.

The drawbacks of using diffuse model are that the estimates are inaccurate due to noise in the degree of polarisation (DOP) measurements, which are small at most locations on the surface. Besides, it is also quite sensitive to the value of refractive index, therefore the measurement of refractive index information is required before the polarisation estimation, while as it can be negligible for specular reflection [2]. Rahmann and Canterakis [83] [84] avoid the problem by using only the phase angle information of the reflected light. The proposed method requires images taken from two views, and both diffuse and specular reflections are considered. However, there is no demonstration of its performance on objects with complicated geometry.

To solve the problem of weak tolerance on noise mentioned above, in this thesis we concentrate on applying the Fresnel theory on images using polarised light instead, with the aid of Malus's law. As far as we are concerned there is few literature concerning this topic, as the models using unpolarised light cannot be fitted in this case, and new polarisation model has to be proposed instead. Both the diffuse and specular reflections have to be considered, as the specular reflectance component in the image is no longer negligible. Besides, the specular component is fully polarised, while as the diffuse component

Reference	Proposed by	Reflection Type	Brief Description
[88]	Saito *et al.*	Specular	Using a spherical diffuser in image acquisition to ensure that specularities can cover the whole surface.
[115]	Wolff	Specular	Taking images from two views for resolving the zenith angle ambiguity problem.
[5]	Atkinson and Hancock	Specular	Based on [115], with reflectance analysis and image processing techniques.
[68]	Miyazaki *et al.*	Specular	Based on [115], optimised for transparent materials.
[117]	Wolff and Boult	Diffuse	Demonstrating how to estimate shape from diffuse polarisation.
[69]	Miyazaki *et al.*	Diffuse	Based on [117], provides framework for reflectance, texture and shape estimation, constraints are made in zenith angle histogram.
[3]	Atkinson and Hancock	Diffuse	Based on [69], considers the inter-reflection phenomenon on the surface.
[83] [84]	Rahmann and Canterakis	Specular and Diffuse	Discarding refractive index information, images are taken from two views, no proof of validity to be applied for general objects.

Table 2.1: The list of shape from polarisation methods based on Fresnel theory.

remains depolarised. Mueller [70] investigates and compares the difference of reflections when using polarised and unpolarised light, and shows how to eliminate specular surface reflectance in both cases. However, the work only concentrates on reflectance separation instead of shape recovery. Terrier and Devlamik [103] introduced a polarisation model which considers Fresnel equations, and estimated polarisation orientations from images using polarised light, with a polarising cube beam splitter to separate Fresnel coefficients. Also this work does not consider the application of shape recovery. Debevec *et al.* [25] proposed a method which recovers shape using polarised light by separating reflectance components using cross-polarisation setting, and estimated the surface normal by BRDF reflectance models. In Chapter 5 we proposed a novel polarisation model for shape recovery which considers the Malus's law, and demonstrate its validity in the experimental section.

It is also noted that one of the disadvantages of shape from polarisation methods is that there is a two-way ambiguity when estimating azimuth angle from the phase of polarisation. Further discussion is in Section 3.2.2, in this thesis we attempt to resolve this with the aid of shape from shading method, which is proposed in Section 6.3.3. Table 2.1 summarises the shape recovery methods mentioned in this section which include Fresnel theory.

2.3 Shape Reconstruction

Shape estimation from images is a key problem in computer vision which has been studied for several decades. It is requisite for reflectance estimation, as it determines the geometry of light reflection from an object. In this section, we only concentrate on the methods of shape from shading and stereo, which are relevant to the proposed methods in this thesis. The main difference between the two methods is that the stereo requires more than one image in different acquisition conditions, while only one image is enough for shape from shading. It is noted that shape from polarisation method can also be regarded as one of the stereo techniques, as it also requires more than one image input, and faces similar issues with stereo.

2.3.1 Shape from Shading

Shape from shading (SFS) was first formulated by Horn [45] for finding the brightness equation, which is the reflectance model that is related to the surface normal estimates. Many SFS methods use the Lambertian model for its simplification [119], but it produces incorrect results when recovering shapes from surfaces that have specular highlights. Ragheb and Hancock [81] focused on incorporating a specular reflectance model using an iterated conditional modes algorithm, and separating reflectance components for surfaces without colour variations.

The SFS method has been proven to be an ill-posed problem [98], meaning it is theoretically impossible to recover shape from general objects using only shading information. Its performance is vulnerable to surfaces if containing complicated textures, as it is hard to distinguish grey colour texture from the shading. There are also two problems for shape from shading methods. First is the bas-relief ambiguity problem [11], in which the surface height cannot be obtained directly using the method. Secondly, the convex-concave ambiguity problem [18], from which SFS will produce incorrect results if it is unknown whether the object has convex or concave surface. These two problems render it impractical for recovering shape from general objects. Therefore, assumptions should be made on the surface geometry, illumination conditions and reflectance properties.

However, SFS still plays an important role in applications where strong constraints

are made, accuracy is not highly required, and only one image can be provided. For example, SFS was applied for measuring the surface height map of the moon [86], and is now widely applied in terrain analysis [15]. Many SFS methods are developed in face shape recovery, in which the shape of faces is known as convex, the albedo map is not complicated, and the surface height is roughly known. Smith and Hancock [99] introduced a framework that applies statistical methods on shape recovery, which can recover satisfactory shape information.

2.3.2 Stereo

Stereo can be divided into two categories, photometric stereo and geometric stereo. Using photometric stereo technology, the images acquired have different illumination directions, while the location of the viewer is fixed. On the other hand, for geometric stereo the viewing directions are different in each input, while their illumination conditions are identical. Compared with the polarisation-based method, which requires only one camera and one light source, the requirements of devices for photometric stereo and geometric stereo are much higher.

In the geometric stereo method, an algorithm is needed to match the pixels in one image to the points in the other inputs having the same locations on the surface. There are several methods suggested in literature for this matching problem, which can be classified into two categories: local and global [19]. For local methods only small regions or points in each image are compared, which include block matching, gradient-based optimisation and feature matching [19]. The weakness of local method is that the process can be disturbed by regions that have uniform texture. The block matching method compares only a small specific region between the input images using variants of cross-correlation or robust rank metrics. Gradient-based optimisation compare the regions using differential equation and squared differences. Feature matching overcomes the weaknesses of block matching and gradient method which are sensitive to locally ambiguous regions, that it firstly chooses the regions for comparisons by feature extraction from the images. Lowe introduced the shape-invariant feature transform (SIFT) in [63], in which the points are matched regardless of the scale and rotation of images.

For the global method, the constraint is relaxed and focused instead on the entire im-

age area. There are several stereo matching approaches which are regarded as global methods: dynamic programming, intrinsic curves and graphs cuts. The most widely used method is dynamic programming, which compares the scan-line of input images and makes the ordering and smoothness constraints for optimisation. Graph matching is the most promising method, which firstly transforms images into graphs and finds similarities between the estimates. Details of method development can be found in [21]. Global method can solve the problems that are occurred in local method, though they requires more computational works and is thus less efficient. Further details are not discussed here as the proposed methods in this thesis are not related to the geometric stereo.

The photometric stereo method uses the reflectance model that considers incident light direction. The surface normal information is computed from the intensity values of the images using the model, the estimates from all images are combined and the error is corrected [122]. Ma *et al.* [64] introduced a rapid acquisition method for surface normal information using four images taken under different gradient illumination conditions. The first three light directions follow x, y and z coordinate orientations. For the fourth condition, incident lights are emitted from all directions which have identical brightness. Thus the image is eliminated of shading and only albedo information remains. Basri *et al.* [8] recovered shape information in uncalibrated photometric stereo, in which the lighting condition is unknown. Principal component separation is used to extract features from the images acquired, which is transformed in the form of a four harmonics matrix.

Unlike geometric stereo, the photometric stereo method can be developed easily, and produces results that are better than SFS. Another advantage is that the computation is relatively fast compared with geometric stereo, as the process of matching is usually time-consuming. However, the method of geometric stereo plays a better role in capturing shape information from moving objects, as during image acquisition several cameras are placed in different locations which can take pictures simultaneously.

There are two weaknesses for the stereo methods compared with the SFS method. Firstly, it requires more than one image and in many cases such a requirement is impossible to meet. Secondly, the majority of stereo methods require complicated devices such as the geometry dome and the light stage described in [25]. However, due to its performance in acquiring accurate shape and reflectance information, the stereo method is now widely

used in the film industry and 3D game development. Besides, there are some technologies of stereo which can reduce the size and cost of the acquisition device, such as Kinect [97].

2.3.3 Surface Height Acquisition

The methods of shape recovery introduced in this chapter generally only recover surface normal information, which is the orientation on any positions of the surface in the form of needle map. The height map, or sometimes regarded as the depth map, can be computed using integration methods. The easiest implementation is to use gradient computation, which can only be applied to synthesised images and is very sensitive to noise [17]. Frankot and Challappa [35] developed a much more robust approach, which also measures surface depth by using gradient fields and projecting them onto the nearest integrable solution. The method is implemented by the Fourier basis function, which makes it tolerable to noise.

The alternative way for measuring surface height, which is mostly used in this thesis, is the shapelets method that was introduced by Kovesi [58]. The method is simple to implement and tolerate noise much better than the approach proposed by Frankot and Challappa. It treats the azimuth and zenith angles separately in the process of surface height acquisition. Therefore, the method can deal with azimuth angle ambiguity, or even produce the results without the need of azimuth angle estimate. It is very convenient for shape from polarisation method, as the azimuth angle is hard to obtain. In Chapter 4 and Chapter 5 we apply the shapelets method in recovering surface height from the zenith angle estimates. The results produced have demonstrated its validity.

2.4 Surface Reflectance Acquisition

The reflectance of an object is generally defined as the angular distribution of light reflected from the object surface for a specific incident illumination [33]. Research into the reflectance estimation in computer vision has attracted a significant amount of attention for several decades. In this section we provide a brief summary on the existing literature. There are two categories of methods in this field: firstly the measurement based on reflectance functions, which are described in Section 2.4.1 and Section 2.4.2. Secondly, we

use the dichromatic model which assumes there are diffuse and specular components in the reflectance, and reflectance can thus be measured using parametric reflectance models.

2.4.1 Reflectance Functions

Reflectance is usually quantified by either the bidirectional reflectance distribution function (BRDF) or the bidirectional surface scattering reflectance distribution function (BSSRDF). The BRDF was first introduced in the 1970s [73]. BRDF assumes that for every material surface, the light is reflected from the same position as it arrives at the surface. This approximation has the advantage in its simplicity, and is valid for describing the properties of materials like metal, but fails for translucent materials and neglects the effect of subsurface scattering.

The function of BRDF contains six variables to be considered, two for incident angles ψ_i, γ_i and two for reflected angles ψ_r, γ_r. The other two are the wavelength and polarisation of the incident radiation, which is considered as one parameter e_{hd} for simplicity. The equation is written as follows [73]:

$$L_r(\psi_r, \gamma_r) = \int_0^{2\pi} \int_0^{\pi/2} L_i(\psi_i, \gamma_i)\ e_{hd}(\psi_i, \gamma_i; \psi_r, \gamma_r)\ \cos\psi_i\ \sin\psi_i\ d\psi_i\ d\gamma_i \qquad (2.3)$$

The BSSRDF extends the BRDF to incorporate the effects of subsurface scattering, which relaxes the assumption and enables subsurface scattering. The light penetrates through the surface at one position and is scattered in the subsurface until it is reflected back at somewhere else. In computer graphics, using the BRDF reflectance models can only render the appearance of objects which are hard and opaque without translucent effects, such as metal and plastic. Reproducing reflectance properties for materials like human skin and leaves is beyond its capacity. In theory, BSSRDF can be used to solve the problem, but its weakness lays in this complexity when solving the full radiative transfer equation. Early time of study in BSSRDF uses technologies of Monte Carlo ray tracing [59] or photon mapping [27], which are all time-consuming.

The utility of the BSSRDF was significantly increased by Jensen *et al.* [53], who simplified the subsurface light scattering problem by using a dipole approximation. BSSRDF measurement is complex and applied mainly on specialised acquisition devices [114]. In

this thesis the objects under study are assumed as dielectric materials, therefore only two reflection coefficients are considered, which are specular and diffuse lights, and we only focus on surface characteristics estimation using the BRDF.

Materials of metal are also not concluded for estimation, which is quite different from the dielectrics in the reflectance properties [113]. The metallic surfaces have a distinct appearance from the dielectric materials due to the electrical productivity of metals, while as the dielectrics lack. Besides, the reflectance of metal surfaces contains a high proportion of specularity, whose brightness is independent of the incident angle. On the other hand, dielectrics have a relatively low specular reflectance.

2.4.2 Reflectance Measurements

There have been a number of attempts in the literature aimed at accurately measuring reflectance. The direct measurement of the BRDF requires a gonioreflectometer [60], which is designed according to the formulation in BRDF, and has four degrees of mechanical freedom to measure the complete function. The data acquired from comprehensive BRDF measurements is quite essential for the correct modelling of surface reflectance. However, the reflectance estimation using gonioreflectometer is difficult and high cost.

There is another device developed by the lighting systems research group at Lawrence Berkeley laboratory (LBL), which used imaging technology for BRDF measurements and produced the results relatively fast and simple. Ward [112] presented a detailed introduction about this LBL imaging gonioreflectometer, the methods for the measurements, and also the problems that occurred. The technology is limited in that it can only estimate the reflections near grazing angles, and does not have much capacity in measuring “more polished surfaces with sharp specular peaks”.

Later, Marschner [67] introduced a new image-based process for measuring the BRDF of homogeneous surfaces ”rapidly, completely, and accurately”. In the method several pictures need to be taken in various directions of illumination light with constant view and posture of the object. It only needs a light source and a digital camera, and the calibration process has to be done beforehand. Marschner also measured the reflectance of human skin, and put a baseball cap on the subject’s head to be captured, to be the reference for the relative positions of the camera, the human subject and the light source.

Sato *et al.* [91] developed a method which resembles geometric stereo. It can acquire the images with the same source light locations and directions while the sample rotates, and uses a simple reflectance model to fit to the data.

Measuring subsurface scattering properties of the skin is necessary, as the information in age is hidden behind the thickness of skin layers [30] [24], which is one of the main aspects that affect the lights scattered inside the skin. Revealing such information would help the research in finding the relationships between age and the reflectance of the subjects. Schmitt *et al.* [92] measured reflectance of skin surface by placing two optical fibres on both sides of the subject, and used a photoamplifer to measure the outgoing radiances from the fibbers. Weyrich *et al.* [114] presented a measurement system using the BSSRDF model, and assumed that the surface is homogeneous and of a high density. The system uses a linear fibber detector designed by [32], which was proved to be suitable for human skin subsurface scattering reflectance measurements.

Debevec *et al.* [25] introduced the method to measure the reflectance variations in human skin from thousands of light sources with different viewpoints. Then they used the database as a reflectance model to render the image of the subject under different illumination backgrounds. The rendered images are hard to distinguish from the pictures taken from the real-world, but the costs of the experiment and establishment of the database is quite huge.

2.4.3 Diffuse and Specular Reflections

In order to provide a simpler and more practical way for reflectance estimation and image rendering in computer vision, Shafer [93] proposed the dichromatic reflection model (DRM) which is an approximation to the BRDF function. In this case, parametric reflectance models are employed for shape recovery and reflectance measurements. The model assumes that reflection can be classified into two categories: diffuse and specular. Consider I as the image intensity, and I_s and I_d as the specular and diffuse components, the equation is written as follows:

$$I = I_s + I_d = k_s f_s(\psi_s, \gamma_s, \boldsymbol{E}_s) + k_d f_d(\psi_d, \gamma_d, \boldsymbol{E}_d) \; . \tag{2.4}$$

where k_s and k_d are specular and diffuse albedo maps representing colour variations independent of shading, and f_s and f_d are reflectance models related to the zenith angle ψ_s ψ_d, azimuth angle γ_s γ_d and parameter set $\boldsymbol{E}_s$ $\boldsymbol{E}_d$ respectively. When light arrives at a surface, part of it undergoes isotropic subsurface scattering before being re-emitted which is denoted as diffuse reflection. The remainder is reflected in a specular manner. Figure 2.3 shows their way of reflecting. It is noted that the intensity distribution of specular reflection is affected by the viewing direction, while it is not for the diffuse case.

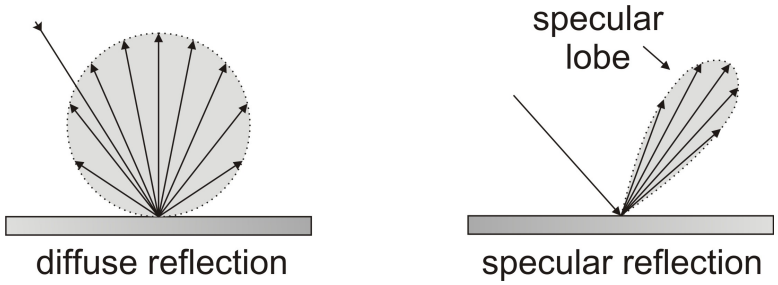

Figure 2.3: The reflections of diffuse (left) and specular (right).

The specular spike is the area on the surface which is highlighted, whose direction is decided by both viewing and incident light orientation. Denote $\overrightarrow{L}$ as the light-source direction, and $\overrightarrow{V}$ as the viewing direction, the reflected orientation of specular spike is

$$\overrightarrow{N_S} = \frac{(\overrightarrow{L} + \overrightarrow{V})}{||\overrightarrow{L} + \overrightarrow{V}||} . \tag{2.5}$$

The geometry of the specular reflection is shown in Figure 2.4. $\overrightarrow{H}$ is the bisector of angle between $\overrightarrow{L}$ and $\overrightarrow{V}$, proposed by Blinn as one of the parameters in the Blinn-Phong model [14] for describing the specular reflectance. It is shown in the figure that viewing direction must be known before estimating $\overrightarrow{N_S}$ as, it is influenced by both $\overrightarrow{L}$ and $\overrightarrow{V}$. Compared with the diffuse components, it is more difficult to measure surface normal information from specular reflections. In this thesis we simplify the problem that all the images used for experiments are acquired following the retro-reflection setting, as the viewing and light directions are identical.

The ratio of intensities between specular and diffuse in the image is mainly decided by the surface roughness. In extreme case that the object is made of metal and ideally smooth, there are no diffuse reflections available, and the specular component becomes a tiny

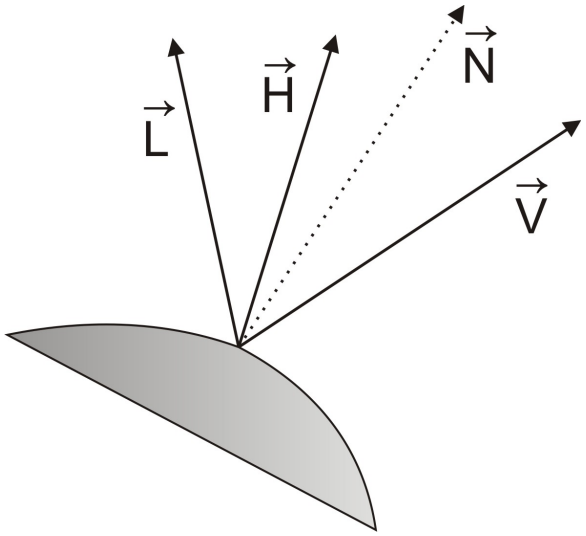

Figure 2.4: The direction of specular reflection from the surface.

shinning highlight on the surface. On the other hand, for surfaces of full roughness such as plaster and terracotta, hardly any specularity can be observed and the whole reflectance intensity follows Lambert's law.

Only a few surfaces have only either diffuse or specular reflection [34]. When performing reflectance estimation from images, the process can be simplified if the two components are separated beforehand. Polarisation is the ideal solution for this work. The components can be separated accurately and robustly following the cross polarisation setting introduced in Section 2.1. The approach does not need information on refractive index, however it requires at least two polarised images whose polariser angles are 0 and 90 degrees. However, in many cases only one image input is available for estimation. Ragheb and Hancock [78] present the method to remove highlights, or specul1ar parts, in the pictures without using polarisation but method of SFS instead. There is only one image required but the method is only suitable for objects without complicated textures.

Lin and Lee [61], on the other hand, separate the diffuse and specular components using photometric stereo, whilst simultaneously recovering surface height. In common with Ragheb and Hancock, they also used the Cook-Torrance model for reflectance model fitting, but eventually opted for the Lafortune model for reasons of greater flexibility when dealing with multiple reflection components. Wu and Tang [121] have extended this method to deal not only with specular and diffuse components, but also with a subsurface

scattering component.

After reflectance components separation, we employ parametric reflectance models for shape recovery and reflectance measurements. In this thesis we use the following models which are widely used: Lambertian model [34], Phong model [76], Torrance-Sparrow model [106], Cook-Torrance model [22], Oren-Nayar model [74] and Beckmann and Kirchhoff model [9].

2.4.4 Parametric Reflectance Models

There are many parametric reflectance models available in the literature, among which the simplest and best known is probably Lambert's law [34]. This model of diffuse reflectance ignores the presence of roughness and specularities, together with all other reflectance properties, except the albedo and the two orientations of incidence and surface normal of the object. Denote k_L as the diffuse albedo map, and ψ the zenith angle, the zenith angle distribution of Lambertian model is written as

$$I_L(\psi) = k_L \cos\psi \ . \tag{2.6}$$

The Phong model, which focuses on modelling the distribution of the specular reflectance component, is also well known for its parametric simplicity [76]. It is one of the oldest reflectance models that consider specular reflection. The Phong model assumes that the surface is smooth, and controls both the shininess of the specular highlight and the size of the specularity area on the surface by the parameter e_P. It is an empirical model, which was not developed following physical laws. Denote k_P as the specular albedo maps, the equation of specular term used in this thesis for the zenith angle distribution of Phone model is:

$$I_P(\psi) = k_P \cos^{e_P}\psi \ . \tag{2.7}$$

Roughness is an important reflectance property, which leads modifications through angular blur of the specular component together with the intensity distributions for the diffuse component. There are two reflectance models that use parameters to specify the roughness of a surface. The first is the Torrance-Sparrow (T-S) model [106] and the

second is the Oren-Nayar model [74]. The T-S model simplifies the reflectance measurements by assuming that the surface consists of mirror-like micro-facets in random orientations. It was developed for accurate performance, especially for non-Lambertian objects. Therefore, the equation of the T-S model is much more complicated than that of the Phone model. In order to obtain more robust results, the reflectance equation is simplified following two constraints. Assuming that the value of the Fresnel term is equal to one, and denoting k_{TS} as the specular albedo map, the zenith angle distribution of the specular term of simplified reflectance model becomes

$$I_{TS}(\psi) = \frac{k_{TS}}{\pi} \frac{Y \cdot O_{TS}(\psi)}{\cos^2 \psi} \ . \tag{2.8}$$

where Y is the geometrical attenuation factor given by $Y = \min[1, 2\cos^2 \psi]$, and O_{TS} is the facet slope function, modelled using a Gaussian distribution given by

$$O_{TS} = \exp(-\psi^2 / e_{TS}^2) \ . \tag{2.9}$$

Cook and Torrance (C-T) modified the T-S model by using the Beckmann distribution to model the facet slope distribution. The improvements in the Cook-Torrance model make it more robust for the reflectance estimation process. The facet slope function of the C-T mode is denoted as O_{CT}, which is given as follows [22]:

$$O_{CT} = \frac{\exp(-\tan^2(\psi)/e_{TS}^2)}{\pi e_{TS}^2 \cos^4(\psi)} \ . \tag{2.10}$$

Another reflectance model based on the C-T model was proposed by He *et al.* in [42], which is a comprehensive physical model that considers many physical phenomena such as polarisation, surface roughness, masking/shadowing and energy. Ngan et.al. [72] conducted a survey of the existing BRDF reflectance models, which are the Phong model, the C-T model, the T-S model, the He model and etc. . They compared the performance of the reflectance models using a metal ball. The experimental results showed that the C-T model and the He model performed best. In this section, we decided not to use the He model in the reflectance model, as the complexity of the equation is unsuitable for the reflectance fitting process.

The Oren-Nayar (O-N) model has been proven to accurately predict the reflections of rough surfaces, such as concrete, plaster, sand and etc. . The model has extended

Lambert's law by adopting the roughness parameter, and has estimated the reflectance by derivation from the micro-facet model, introduced by Torrance and Sparrow in [106]. The roughness property of the surface is specified by the parameter e_{ON}, which is the standard deviation value of the Gaussian distribution for the facet slope, with ranges within $[0, \frac{\pi}{2}]$. Denote k_{ON} as the diffuse albedo map, we simplify the zenith angle distribution of O-N model, which is given by

$$I_{ON}(\psi) = \frac{k_{ON}}{\pi} \cos(\psi)[\alpha(e_{ON}) + \beta(e_{ON}) \sin\psi \tan\psi] \; . \tag{2.11}$$

where α and β are parameter coefficients for the O-N model defined in [74]. The approximation of the two coefficients is written as

$$\alpha(e_{ON}) = 1 - 0.5\frac{e_{ON}^2}{e_{ON}^2 + 0.33} \; , \tag{2.12}$$

$$\beta(e_{ON}) = 0.45\frac{e_{ON}^2}{e_{ON}^2 + 0.09} \; . \tag{2.13}$$

Another reflectance model that also considers roughness was introduced by Beckmann and Kirchhoff (B-K) [9]. The B-K model is a purely physics-based model, which is well known in optics physics. However, limited work has been done in applying the model to reflectance estimations. In [82], the B-K model is suitable for predicting the reflection of a surface that is either smooth, slightly rough or very rough. The equation of the B-K model is different in these two cases, in this section we consider only the one for estimating slightly rough surface.

The weakness of the B-K model is that it fails to predict the reflection of wide-angle scattering and large angles of incidence [80]. Vernold and Harvey proposed a modified version of the B-K model which solves the problem [82]. They replaced the geometrical factor in the B-K model with a Lambertian term ($\cos\psi$). This modification relies on empirical observations, and does not follow any physical laws. In [82] it is shown that, for some materials the B-K model performs better for reflectance estimation than the O-N model. Here, we apply the Vernold-Harvey version of the B-K model for estimating specular reflections, and the performance is demonstrated in [80]. Ragheb and Hancock proposed a simplified B-K model following several constraints [82], given as:

$$I_{BK}(\psi) = \frac{e_T^2 e_\lambda^2}{16\pi e_A e_\rho^2 \cos\psi} \exp(\frac{-e_T^2 \tan\psi^2}{4e_\rho^2}) \ . \tag{2.14}$$

where the roughness parameter of the B-K model is denoted as e_ρ, which is the root-mean-square height deviation of the surface. e_λ is the wavelength. e_A is the parameter which determines the roughness category of the plane sheet [100]. e_T is the correlation length that the values of either the Gaussian or the exponential correlation function is lower than $1/e$. Assume that the parameter e_A is a constant value, and denote $k_{BK} = e_\lambda^2/(4\pi e_A^2)$ and $e_{BK} = e_T^2/(4e_\rho^2)$, the simplified zenith angle distribution of the B-K model is given as:

$$I_{BK}(\psi) = k_{BK} e_{BK} \exp(-e_{BK} \tan^2\psi)/\cos\psi \ . \tag{2.15}$$

In Chapter 6 we introduce a shape and reflectance measurement framework, in which there are two reflectance models required to estimate from diffuse and specular components respectively. In this thesis they are chosen from the above six models, and several experiments have been conducted to demonstrate if which are mostly compatible with the proposed framework.

2.5 Statistical Methods

One of the novel contributions for the shape and reflectance estimation methods in this thesis is that the algorithms are developed with the aid of statistical methods. Therefore, the methods proposed have improvements in robustness and accuracy over traditional ways. In this section we provide literature for the following three technologies, which are mostly used in this thesis: blind source separation, mutual information estimation, and maximum *a posteriori* method.

2.5.1 Blind Source Separation

The method of blind source separation (BSS) was first formulated in [54]. In BSS we aim to extract the underlying source signals from a set of linear mixtures, where the mixing matrix is unknown [55]. The input mixture is regarded as a multivariate data matrix, and linear transformations are applied to identify the underlying geometry. There are several

widely used linear transformations, including principal component analysis (PCA) and independent component analysis (ICA). PCA locates the directions of maximal variance in the input matrix. ICA estimates the similarities between the extracted components using a mutual information criterion and produces a more robust separation.

BSS has been exploited in several domains including signal processing, neural networks and speech source separation. In computer vision, BSS has been applied to a number of reflectance separation problems, including the removal of reflections from transparent glass surfaces. Examples include the works in [31] and [16], which use sparse ICA to perform the separation and achieve better results at the expense of a more complicated algorithm. Umeyama and Goldin have extended the method of Bronstein *et al*, using two polarised images, and separated the diffuse and specular reflectance components [110]. The method requires two polarised images using different polariser angles, mutual information estimation is applied as a criterion function for separation, and the unknown polariser orientation information can also be obtained. However, there are two problems with their method. Firstly, it can only be used in cases where the brightness of specularities for the two input images is different, which is difficult to meet if the source light is unpolarised, for example the input images shown in Figure 3.7. Secondly, the information contained in the phase angle is not used. This is an important factor in polarisation vision, and compromises the accuracy of the separation. Our work of BSS method is based on the method of Umeyama and Goldin, which was developed following the polarisation vision techniques, and solved the problems addressed above.

2.5.2 Mutual Information Estimation

Mutual information is one of the main topics in information theory, its notion is discussed in [1, 23]. In computer vision and image processing the techniques of measuring mutual information are generally applied in image similarity estimation [87], image alignment [111] and image registration [65]. It was first developed by Woods *et al.* [118] in the 1990s, and further extended by Hill *et al.* [44]. They developed a 2D joint histogram that describes intensity distributions of two images and their relationship in plots. The advantage of using mutual information is that large differences in small areas of image inputs only have a little influence on the similarity result, therefore it can tolerate error.

However, it considers only the values of pixels instead of their positions; therefore, the method is unable to estimate image geometry similarity. Russakoff *et al.* [87] solved this issue by introducing the regional mutual information method which also considers neighbourhood regions of pixels.

The methodology of mutual information is based on the concept of entropy, which is regarded as the amount of information the observed input can provide [77]. For example the image, which has the constant intensity value for all pixels, has the lowest entropy value. There is almost no information inside. On the other hand, when the intensities of image are randomly distributed, a high entropy value can be yielded from it. It was originally studied in the domain of information theory, and Hatley [41] applied it in computer vision for measuring information quantity during image transmission. The weakness of the method proposed is that it assumes all information has the same priority, which makes it unusable in application. Shannon improved the model in [96] which has weighted coefficients computed by the probability of the information that occurs. Shannon entropy is now widely used during the process of mutual information estimation, which is presented in Chapter 4.

2.5.3 Maximum *a posteriori* Estimation

The optimisation method is applied for the process of estimating maximum *a posteriori* (MAP) probability information. Besag [13] introduced the iterated conditional modes (ICM) algorithm for analysis on the dirty pictures. The ICM method is an iterative process which calculates local maximum results following a "greedy strategy". It is simple and effective, though the optimisation results are notoriously poor.

Ragheb and Hancock [79] developed a MAP estimation method for separating specular and diffuse reflectance by estimating their mixing proportions using a Bayesian framework, and hence recovered improved shape from the diffuse component. However, the method is confined to situations in which the there is little variation in surface albedo, i.e. there is little or no surface texture. This renders it in-practical for real world applications. However, their ideas do provide the starting point for a more robust probabilistic algorithm based on the use of polarisation information. In this thesis we have developed several ICM methods for estimating MAP using probabilistic models.

2.6 Conclusions

In this chapter we have presented literature in computer vision which is relevant to our work. The methods are compared with the alternatives, and we have analysed their strengths and limitations. We summarise them in this section and propose our possible solutions, which are the contributions introduced in the subsequent chapters.

Shape and reflectance estimation has been studied for decades and huge amounts of methods have developed accordingly. In this thesis we investigate four shape reconstruction methods, which are SFS, photometric stereo, geometric stereo and shape from polarisation method. All of these approaches have their own advantages and weaknesses. SFS is widely used for its low requirements of acquisition devices, and only one image is enough for the process. However the method itself is an ill-posed problem [98]. Many constraints have to be made and its applications are usually limited to constant-albedo Lambertian surfaces and simple illumination environment. The shape estimate also lacks accuracy and is not reliable enough to be used in further processes.

Photometric stereo and geometric stereo, on the other hand, have the strength which the SFS method lacks. As previously mentioned, both methods perform perfectly in recovering shape information, but also require high-cost devices for acquisition. The method of geometric stereo is more difficult to develop as images taken from cameras in different locations have to be matched. In this thesis we have mainly used polarisation technologies, and shape from shading methods in some parts of the proposed frameworks. We haven't used stereo methods as those are beyond the scope of this thesis.

Polarisation has been demonstrated to be an effective method for shape reconstruction using Fresnel theory. After three polarisation states are measured from several polarised images taken in different polariser orientations, there are two Fresnel polarisation models available for computing zenith angle from value of degree of polarisation. The diffuse model is preferred in polarisation vision, as the ambiguity problem for specular model has to be resolved and the spherical diffuser introduced in [68] is a prerequisite for acquisition.

The advantages of the polarisation-based method are as follows: firstly, unlike stereo methods, it only requires one light source and one camera for capturing photos, thus the cost for the experiments can be greatly reduced. Secondly, the results produced are far superior to the SFS method. However, it still needs several image inputs which cannot be

taken simultaneously, which might be troublesome for non-static subjects, such as human faces and palms. Another problem is the ambiguity problems for estimating azimuth angle from the phase angle estimate. Besides, the shape from polarisation method cannot produce results with the same accuracy as the stereo.

Broadly speaking there are two different ways of reflectance estimation: using special devices such as the gonioreflectometer or geometry dome for measuring reflectance functions directly, or using dichromatic models, which is more convenient and low-cost. In this thesis, we choose the solution of dichromatic models and applied parametric models for the measurements. According to the dichromatic model, the reflectance can be classified into two components: diffuse and specular. The two components have their corresponding reflectance models which can compute zenith estimate from component intensity, as shown in Section 2.4.4. The proposed method is based on an assumption, that if the parameter values of the chosen models are correct, the two zenith angle estimates from the diffuse and specular components become identical.

Using mutual information estimation and Newton's method, we develop an iterative method, that in each step the zenith angle estimates from diffuse and specular components are compared, and the parameter values of the reflectance models are adjusted using Newton's method, to make the two estimates as close to each other as possible. The criterion function in the Newton's method is the mutual information estimation of the two zenith angle results. Details of the contributions are presented in 6.

In this thesis, we used polarisation-based methods for shape and reflectance estimation, as it perfectly suits our needs. Although the polarisation approaches have problems as described above, they can be resolved with the aid of statistical methods. We used the BSS method proposed in Chapter 3, so that the number of images required is reduced to only three. This can greatly speed up the acquisition process and thus the alignment problem is avoided. In the BSS algorithm we applied mutual information estimation to measure the similarities, which gives a better result than least square fitting as also shown in Chapter 3. We have constructed three probabilistic models using the ICM method presented in Chapter 4, Chapter 5 and Chapter 6.

Chapter 3

Polarisation Estimation using Blind Source Separation

In this chapter we focus on estimating polarisation status from images taken under unpolarised light. Traditional methods apply the Fresnel theory on shape from polarisation, which use the Fresnel coefficient for predicting ratios of reflected and transmitted light when it arrives at a surface. Theoretically three images are enough for polarisation measurements. However, in practice more images are required for de-noising.

We propose a novel method which incorporates statistical methods (especially BSS) and Newton's method into the estimation of the polarisation image. It does not require the polariser angle information, thus we can use polarising filters for shape from polarisation instead of relying on polariser, making the technology of shape from polarisation more convenient in some applications. The two key ideas underpinning the approach are to use weighted singular value decomposition (SVD) to compute the polariser angles, and to use a mutual information criterion function to optimise the weights. We calculate the surface normal information using the Fresnel equation, and iteratively update the values of weighting matrix and refractive index to a recover surface shape. In this chapter we also give a brief overview on the polarisation vision and BSS which are relevant to the proposed method.

As mentioned in Chapter 2 the Fresnel theory can estimate surface shape from both diffuse and specular reflections. Both the two corresponding Fresnel models have advantages and disadvantages and can be applied in different cases. In this chapter we only

focus on the diffuse model, as it only requires simple image acquisition devices. In Chapter 4 more sophisticated discussions and analysis are presented, in which we develop another criterion functions for Newton's method, and a novel Fresnel model is proposed which considers both diffuse and specular reflections.

Contribution

The principal contributions in this chapter are:

- Commencing from the method of Umeyama and Goldin introduced in Section 2.5.1, we show how to accurately estimate polarisation state without prior knowledge of the input polariser orientations.
- Our method is based on a mutual information criterion, which is optimised with respect to determine the polariser angles and other parameters using Newton's method rather than exhaustive search, thus giving a relatively fast iterative procedure.
- Our method is also referred from the Fresnel theory. This leads to an iterative process that interleaves the processes of estimating shape based on the current polarisation state measurement, and updating the polarisation estimation based on the current shape estimate.
- We also show how to use the proposed method to estimate refractive index, and prove that the results are physically reasonable.

Chapter Outline

The outline of this chapter is organised as follows. We commence by introducing polarisation vision and BSS, and show how to incorporate them into the proposed method in Section 3.1. Section 3.2 presents a brief overview of Fresnel theory and how it is applied to estimate the zenith and azimuth angle from the polarisation state estimates. Section 3.3 provides the iterative process based on Newton's method, and Section 3.4 shows the details of experimental results.

3.1 Polarisation Estimation

In this section we show how to estimate polarisation using BSS. We commence by using a sequence of images collected with varying polariser angles. From these we aim to robustly estimate the polarisation states from the reflected light, which is also known as *polarisation image*. The polarisation image plays an important role in this thesis which consists of three components, namely mean-intensity $\bar{I}$, degree of polarisation (DOP) ρ and phase ϕ. It is noted that human vision is insensitive to the phase and DOP intensities. Wolff [116] measured the polarisation image information from only three images collected with polariser orientations of approximately 0, 45 and 90 degrees. Denote I_0, I_{45} and I_{90} as the three inputs, the three parameters of polarisation are obtained using the following equations

$$\begin{aligned} \phi &= (1/2)\tan^{-1}(\frac{I_0 + I_{90} - 2I_{45}}{I_{90} - I_0}) + 90^\circ \\ &\quad \text{if } (I_{90} < I_0)[\text{ if } (I_{45} < I_0)\phi = \phi + 90^\circ \text{ else } \phi = \phi - 90^\circ] \,, \end{aligned} \tag{3.1}$$

$$\bar{I} = I_0 + I_{90} \,, \tag{3.2}$$

$$\rho = \frac{I_{90} - I_0}{(I_{90} + I_0)\cos 2\phi} \,. \tag{3.3}$$

The application is limited due to its specific requirement on polariser angles. An alternative approach is to use the transmitted radiance sinusoid (TRS) equation [117]. Here more than three images can be used to estimate the polarised image and eliminate the effects of noise. However, the method cannot be applied when the subjects are not static, as it will become problematic for image alignment. Recently [89] introduced a method to estimate the polarisation image in a robust way, which improves the results when the number of the images taken is large, but still performs poorly when only three polarised images are used in computation.

3.1.1 Observations through the Polariser

As stated in Chapter 2, polarisation is the wave properties of light describing its oscillation directions. When the unpolarised light impinges on a surface, part of the light is reflected which becomes partially polarised. Such effects can be observed by using a linear polar-

ising filter, as the light intensity has a transmitted radiance through the polariser, which oscillates sinusoidally as the polariser angle θ is rotated [117]. The polariser orientation ranges from 0 to 180 degrees. The pixel brightness is maximum when the polariser is aligned with the phase angle (which corresponds to the angle of maximum transmission), and is minimum when the polariser angle is set to the Brewster angle (at which the light becomes perfectly polarised). Denote $I_{\max}$ as the maximum brightness, $I_{\min}$ the minimum brightness and ϕ the phase angle of the reflected light, the measured intensity follows the TRS equation [71]:

$$\begin{aligned} I(\theta) &= \frac{(I_{\max}+I_{\min})}{2} + \frac{(I_{\max}-I_{\min})}{2}\cos(2\theta - 2\phi)\ , \\ &= \frac{(I_{\max}+I_{\min})}{2} + \frac{(I_{\max}-I_{\min})}{2}\cos 2\theta \cos 2\phi + \frac{(I_{\max}-I_{\min})}{2}\sin 2\theta \sin 2\phi\ . \end{aligned} \tag{3.4}$$

where θ is the polariser angle. Figure 3.1 illustrates this relationship. It is noted that without the linear polarised component the TRS equation becomes a constant value for every polariser angles, whereas if there is no unpolarised component the value of $I_{\min}$ reaches 0.

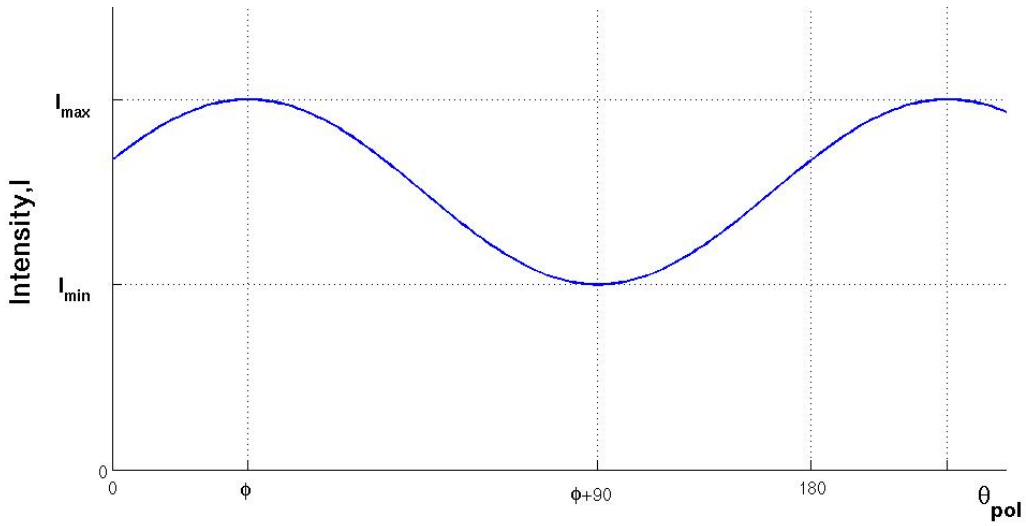

Figure 3.1: The equation of transmitted radiance sinusoid.

In this chapter we work with three $N_x \times N_y$ images captured under different polariser orientations θ_1, θ_2 and θ_3. Each image is converted into a long-vector of length $N_x N_y$.

The long-vectors are the columns of the observation matrix $\boldsymbol{X}$, which is composed of the following column vectors:

$$\boldsymbol{X} = [x_1, x_2, x_3] \, . \tag{3.5}$$

where x_i is the long-vector formed by stacking the columns of the i-th polarisation image. Consider the matrix

$$\begin{aligned} \boldsymbol{C} &= [(\frac{J_{max} + J_{min}}{2}), (\frac{J_{max} - J_{min}}{2} \cos 2\phi), (\frac{J_{max} - J_{min}}{2} \sin 2\phi)] \\ &= [c_1, c_2, c_3] \, . \end{aligned} \tag{3.6}$$

where J_{max} and J_{min} are long-vectors of length $N_x N_y$ that contain $I_{\max}$ and $I_{\min}$ as elements. The three components of $\boldsymbol{C}$ are represented by c_1, c_2 and c_3, hence we can have J_{max}, J_{min} and ϕ by

$$\phi = \frac{1}{2} \tan^{-1}(\frac{c_3}{c_2}) \, , \tag{3.7}$$

$$J_{max} = c_1 + \sqrt{c_2^2 + c_3^2} \, , \tag{3.8}$$

$$J_{min} = c_1 - \sqrt{c_2^2 + c_3^2} \, . \tag{3.9}$$

Define $\boldsymbol{A}$ as the mixing coefficient matrix determined by the three polariser orientations, which is written as

$$\boldsymbol{A} = \begin{bmatrix} 1 & \cos 2\theta_1 & \sin 2\theta_1 \\ 1 & \cos 2\theta_2 & \sin 2\theta_2 \\ 1 & \cos 2\theta_3 & \sin 2\theta_3 \end{bmatrix} \, . \tag{3.10}$$

Hence c_1, c_2 and c_3 can be determined by

$$\boldsymbol{X} = \boldsymbol{C}\boldsymbol{A}^T \, . \tag{3.11}$$

As the input matrix $\boldsymbol{X}$ is known, the polarisation state can be obtained if the three polariser angles measurements are correct.

3.1.2 The Method of Blind Source Separation

In this paper we use the method of BSS to find the unknown parameters (i.e. the polariser angle settings). It is generally applied to separate mixed signals into independent components, where the mixtures are linear. Usually problems of BSS are solved by ICA, which was developed for extracting features from non-linear data [50]. Detailed information about ICA and its developments are summarised in [49]. The method is extended from PCA, which was invented by Karl Pearson as a linear dimension reduction technique [51].

The difference between PCA and ICA is that PCA finds uncorrelated components from the matrix with the largest variances, therefore it can be applied in de-noise process. On the other hand, the components extracted from ICA may not be the principal features from the input data, but as nearly statistically independent of each other as possible. There is no order among the components computed from ICA. Several methods in computer vision utilise ICA for computing independent components, e.g. Tsumura *et al.* [107–109] developed a framework of skin colour from Asian subjects and applied ICA to separate hemoglobin and melanin pigmentation layers. In brain signal processing it is used for analysing EEG and MEG signal process [66].

Our aim is to find the correct mixing matrix $\boldsymbol{A}$, in which the values J_{max}, J_{min} and ϕ follow the constraints provided by the theory of polarisation. For our framework the approach of ICA is inappropriate to be applied as there is no proof that the three components c_1, c_2 and c_3 are independent. To implement BSS, we commence by applying SVD to the data matrix $\boldsymbol{X}$, which is also known as Karhunen-Loève transform, or the Hotelling transform [26]. This method is one of the main steps from PCA, and is generally used to decompose the input matrix into two smaller matrices. We choose it for feature extraction as it can eliminate noises and unwanted features from the image inputs, and produce robust results.

When performing component analysis, it is normal to centre the data matrix. However, here we cannot perform this operation since it will distort the diffuse reflectance component. Also, as [110] shows, using SVD for component separation without whitening remains valid according to experimental results. The SVD of the data matrix $\boldsymbol{X}$ gives

$$\boldsymbol{X} = \boldsymbol{U}\boldsymbol{D}\boldsymbol{V'}^{T} . \tag{3.12}$$

where $\boldsymbol{U}$ is the $N_x N_y \times 3$ left eigenvector matrix, $\boldsymbol{D}$ the 3×3 diagonal matrix of singular values, and $\boldsymbol{V}$ the 3×3 right eigenvector matrix. We let $\boldsymbol{S'} = \boldsymbol{U}\ \boldsymbol{D}$ to simplify the equation. $\boldsymbol{V'}$ is given as

$$\boldsymbol{V'} = \begin{bmatrix} v_{11} & v_{12} & v_{13} \\ v_{21} & v_{22} & v_{23} \\ v_{31} & v_{32} & v_{33} \end{bmatrix} . \tag{3.13}$$

Our aim in this chapter is to adjust $\boldsymbol{V'}$ and $\boldsymbol{S'}$ so that they can be equal to $\boldsymbol{A}$ and $\boldsymbol{C}$, which are the two matrices we need to obtain. There are two steps needed in the proposed method, firstly the determinant values of $\boldsymbol{V'}$ and $\boldsymbol{S'}$ are corrected, and secondly we use a weight matrix $\boldsymbol{W}$ to adjust the values in the two matrices, while as their determinants remain unchanged. We employ a scaling coefficient μ in the first step, $\boldsymbol{V}$ and $\boldsymbol{S}$ are the results using the following equations

$$\boldsymbol{S} = \mu \boldsymbol{S'} , \tag{3.14}$$

$$\boldsymbol{V} = \mu^{-1} \boldsymbol{V'} . \tag{3.15}$$

When the determinant of $\boldsymbol{S}$ is correct, the component s_1 in $\boldsymbol{S} = [s_1, s_2, s_3]$ should be equal to c_1 in $\boldsymbol{C} = [c_1, c_2, c_3]$, which is the mean value of maximum and minimum intensity as shown in Equation 3.6. Here we assume that the mean value of three input images denoted as $\bar{x} = (x_1 + x_2 + x_3)/3$ is equal to c_1, therefore we have a simple expression for computing the scaling factor μ:

$$\mu = \text{mean}(\frac{\bar{x}}{s_1}) . \tag{3.16}$$

In the second step, denote $\boldsymbol{W}$ as a 3×3 weight matrix, then we can write

$$\boldsymbol{S} = \boldsymbol{C}\boldsymbol{W}^{-1} , \tag{3.17}$$

$$\boldsymbol{V} = \boldsymbol{A}\boldsymbol{W}^{T} . \tag{3.18}$$

We impose the constraint that the value of the determinant of $\boldsymbol{W}$ is unity, which leads to the following condition

$$|\boldsymbol{A}| = |\boldsymbol{V}| \,. \tag{3.19}$$

where we assume that the correct value of the determinant of $\boldsymbol{A}$ is equal to that of $\boldsymbol{V}$, as given in [110]. Experimentally, we find that without this constraint, the estimation process becomes unstable and the recovered results are inconsistent with the image contents. Thus the elements of $\boldsymbol{S}$ can be determined by SVD, giving the unknown elements of the matrix $\boldsymbol{A}$ which are determined by θ_1, θ_2 and θ_3. In fact, the value of θ_3 can be obtained when the values of θ_1 and θ_2 are known using Equation 3.10, Equation 3.18 and the constraint Equation 3.19, which gives

$$\left| \begin{pmatrix} 1 & \cos 2\theta_1 & \sin 2\theta_1 \\ 1 & \cos 2\theta_2 & \sin 2\theta_2 \\ 1 & \cos 2\theta_3 & \sin 2\theta_3 \end{pmatrix} \right| = |\boldsymbol{V}| \,. \tag{3.20}$$

Therefore, the number of parameters required to be estimated is reduced to 2.

3.2 Shape Estimation

When the incident light is unpolarised, after subsurface scattering and remission from the surface it becomes partially polarised. Generally speaking the polarisation state of the outgoing light has four degrees of freedom, which are the intensity of reflected light, the phase angle, DOP and the circular polarisation, which is considered to be negligible here. The mean intensity represents the image brightness if acquired without the polarising filters. The phase angle is the polariser orientation that maximum light transmission is permitted. As the oscillation orientation of the polarised light corresponds to the azimuth angle, it is also related to the value of the phase angle.

The degree of polarisation measures the proportion of how much initially unpolarised light becomes linearly polarised on reflection. It becomes 1 when the light is fully polarised, and 0 if unpolarised. Its value is determined by $I_{\min}$ and $I_{\max}$, the maximum and minimum intensities of the TRS, which is described in Section 3.1.1. The difference $I_{\max} - I_{\min}$ shows the magnitude of reflected light that is linearly polarised. The definition of DOP is given as follows [3]:

$$\rho = \frac{I_{\max} - I_{\min}}{I_{\max} + I_{\min}} \,. \tag{3.21}$$

3.2.1 Zenith Angle Estimation

In this chapter we choose the diffuse Fresnel polarisation model for surface estimation, as the equation has no zenith angle ambiguity problem and the devices for image acquisition are simple and low-cost. The model is based on the works in [3], [117] and [69]. According to the Fresnel theory [117] the diffuse polarisation occurs when part of the unpolarised light penetrates the surface, gets refracted back after subsurface scattering and becomes partially polarised. Therefore, the DOP value is relatively lower than specular polarisation, and harder to measure. It is also noted that multiple scattering from microfacets can also produce diffuse reflection, which although small for most of the smooth materials, cannot be predicted by the diffuse polarisation model.

As mentioned in Chapter 2, the Fresnel polarisation model is constructed from Fresnel coefficients. As there are two refractions which occur in diffuse polarisation, we employ Snell's law [69] as it describes the direction of light when transmitted from one medium to the other. The diffuse Fresnel model introduced in [3] shows that the polarisation is determined by two parameters: the refractive index n and the zenith angle ψ. The refractive index is the measure of the ratio of the speed of light in a vacuum to that in a medium. It is an important physical property that determines the optical characteristics of the observed material. The zenith angle is one of the values in surface normal, which is the angle between the light source direction and surface normal. The equation is written as follows:

$$\rho = \frac{(n - 1/n)^2 \sin^2 \psi}{2 + 2n^2 - (n + 1/n)^2 \sin^2 \psi + 4 \cos \psi \sqrt{n^2 - \sin^2 \psi}} \,. \tag{3.22}$$

It is concluded from Equation 3.21 and Equation 3.22 that if the refractive index n is known, the zenith angle ψ can be determined by measurements of $I_{\max}$ and $I_{\min}$. A more sophisticated overview of Fresnel theory is presented in Chapter 4.

3.2.2 Azimuth Angle Estimation

As mentioned in Section 3.2 the azimuth angle can be computed using the phase angle of the polarisation image. However, since the phase angle only ranges from 0° to 180°, a directional ambiguity must be resolved beforehand.

One way of resolving the ambiguity is to use two views and combine information so as to constrain the plane orientation. Rahmann computes the polarisation states separately from both views and compares the results [83], the technique is further investigated and applied to transparent objects in [68]. Atkinson and Hancock [7] used photometric stereo to solve the ambiguity problem. The method is proved robust, although it requires additional images collected at different illumination orientations.

A second approach is to make the assumptions concerning object shape based on local convexity or concavity [3, 69]. However, this approach lacks robustness. The ambiguity problem is one of the main issues in shape from polarisation. In this chapter it is beyond the scope of discussion as we only concentrate on polarisation status measurements. In Chapter 6 we present a method which can solve the ambiguity problem in a robust way, with the aid of shape from shading.

3.3 Iteration Process

In this section we present the iterative method to estimate shape and polarisation information. There are three parameters to be estimated which are the polariser angles θ_1, θ_2 and the refractive index n. We may calculate them by exhaustive search [110], which will give a globally optimal solution, but is also time-consuming. Here we solve the problem by employing the Newton's method for its rapid (quadratic) convergence. Stated succinctly, we use the quasi-Newton algorithm to find the local maximum and minimum values in the given function.

3.3.1 Newton's Method

Newton's method requires initial values of the parameters for estimation, and criterion function to be minimised. We initialise the parameters by setting $n^{(0)} = 1.4$ as this is

typical of the materials studied, and use the following constraint to compute $\theta_1^{(0)}$, $\theta_2^{(0)}$ and $\theta_3^{(0)}$:

$$\boldsymbol{A}^{(0)} = \boldsymbol{V} \ . \tag{3.23}$$

where the superscript is the iteration number. The second factor to be considered is the criterion function, as Newton's Method uses it to correct the values of three parameters. In this chapter we propose a strategy that estimates the similarity between the average intensity $\bar{I}^{(0)} = [I_{\min}^{(0)} + I_{\max}^{(0)}]/2$ and the diffuse reflectance component. The two estimates are similar with each other over most of the surface, except in the proximity of highlights. Ignoring specularities, we use Lambert's law to link diffuse reflectance to the estimated surface normal direction. As a result we can write

$$\bar{I}^{(0)} \propto \cos\psi^{(0)} \ . \tag{3.24}$$

We let $Z^{(0)} = \cos\psi^{(0)}$, where the superscript is the iteration number. According to (3.24), for every pixel in the image the value of $Z^{(0)}$ is monotone increasing with intensity value $\bar{I}^{(0)}$. As texture and highlight information is contained in $\bar{I}^{(0)}$, it is inadvisable to directly fit the values of $Z^{(0)}$ to $\bar{I}^{(0)}$ using Lambert's Law. Least square fitting method therefore is inappropriate to be applied here, as it is too sensitive to the case where there are large differences in relatively small areas of input images. The difference in the highlight area in this case will ruin the results. Instead, here we gauge their similarity using mutual information between their distributions as it can tolerate this problem. The aim is to find the set of parameters that maximise the distributional mutual information.

3.3.2 Mutual Information Estimation

To compute the mutual information the probability density functions for the two measures together with their joint distribution function are required. We compute the distributions of $Z^{(0)}$ and $\bar{I}^{(0)}$ using their associated normalised histograms, denoted as δ and ζ, respectively. The histogram presents the grey value distribution of the image, which is computed by counting the number of pixels available for every bin range, and dividing those numbers by the total sums of pixels in the image.

Both histograms are quantised into λ bins. It is noted that the value of λ determines the speed of estimation and accuracy of results. It cannot be too low as the information provided will become insufficient to the histogram. However, if it gets too large the histogram will be too sparse and vulnerable to the image noise. Rajwade *et al.* [85] proposed an approach which assumes the inputs as continuous surfaces. Here we simply set the number of λ as 100 as the process of Rajwade's approach is time-consuming. The Shannon entropy for the probability density functions is:

$$H = \sum_{i=1}^{\lambda} p_s(i) \log \frac{1}{p_s(i)} = -\sum_{i=1}^{\lambda} p_s(i) \log p_s(i) \ . \tag{3.25}$$

where $p_s(i)$ is the probability of density for bin i computed from the normalised histogram. According to the first definition of the Shannon entropy in Equation 3.25, the term $\log \frac{1}{p_s(i)}$ shows that the information amount is inversely related to the entropy value H. It is sensible because when the information provided is rarer, its importance becomes more to the whole data. For each information of the input data, the Shannon entropy equation also adds $p_s(i)$ as the weight representing the probability of information occurrence. In this chapter we use the second definition of Shannon entropy in Equation 3.25 for its simplicity.

The joint entropy describes the relationship between the two inputs, and it becomes minimised when the two inputs have one-to-one mapping. Denote $H(\delta, \zeta)$ as the joint entropy, and the two probability density of two images as p_δ and p_ζ, respectively. The equations of the joint entropy $H(\delta, \zeta)$, and the entropies for the two images $H(\delta)$ and $H(\zeta)$ can be calculated using the Shannon entropy written as

$$H(\delta) = -\sum_{i=1}^{\lambda} p_\delta(i) \log p_\delta(i) \ , \tag{3.26}$$

$$H(\zeta) = -\sum_{i=1}^{\lambda} p_\zeta(i) \log p_\zeta(i) \ , \tag{3.27}$$

$$H(\delta, \zeta) = -\sum_{i=1,j=1}^{\lambda,\lambda} p_{\delta,\zeta}(i,j) \log p_{\delta,\zeta}(i,j) \ . \tag{3.28}$$

To compute the joint probability distribution, we construct the joint normalised histogram $p_{\delta,\zeta}$, whose size is defined as $\lambda \times \lambda$. The relationship between $p_{\delta,\zeta}$, p_δ and p_ζ

is

$$p_\delta(i) = \sum_{j=1}^{\lambda} p_{\delta,\zeta}(i,j) \,, \tag{3.29}$$

$$p_\zeta(j) = \sum_{i=1}^{\lambda} p_{\delta,\zeta}(i,j) \,. \tag{3.30}$$

Hence the mutual information between the distributions is given by

$$B(Z^{(0)}; \bar{I}^{(0)}) = H^{(0)}(\delta) + H^{(0)}(\zeta) - H^{(0)}(\delta,\zeta) \,. \tag{3.31}$$

which leads to the joint entropy of these distributions.

3.3.3 Update Equation

In optimisation, Newton's method is applied to find the point whose gradient is equal to zero in the given function. The equation of Newton's method used in the iterative process can be generalised as follows:

$$\Theta^{(t+1)} = \Theta^{(t)} - \eta \boldsymbol{Q}[B^{(t)}]^{-1} \nabla B^{(t)} \,. \tag{3.32}$$

where Θ is the set that includes the parameters to be updated. In this section we have $\Theta^{(t)} = (\theta_1^{(t)}, \theta_2^{(t)}, n^{(t)})^T$. η is the step size and, in this thesis, we set $\eta = 1$, so that the Newton's method can converge quadratically.

Newton's method employs the inverse of the Hessian matrix to update the parameter values. Here the Hessian of the error-function is $\boldsymbol{Q}[B^{(t)}]$, and ∇B is its gradient. The Hassian matrix is a square and symmetrical matrix, which describes the local curvature of the given function. For example, in this section there are three parameters to update, and the criterion function is the mutual information estimation equation $B(F; \bar{I})$. The Hassian matrix $\boldsymbol{Q}$, therefore, is written as

$$\boldsymbol{Q} = \begin{bmatrix} \frac{\partial^2 B}{\partial \theta_1^2} & \frac{\partial^2 B}{\partial \theta_1 \partial \theta_2} & \frac{\partial^2 B}{\partial \theta_1 \partial n} \\ \frac{\partial^2 B}{\partial \theta_2 \partial \theta_1} & \frac{\partial^2 B}{\partial \theta_2^2} & \frac{\partial^2 B}{\partial \theta_2 \partial n} \\ \frac{\partial^2 B}{\partial n \partial \theta_1} & \frac{\partial^2 B}{\partial n \partial \theta_2} & \frac{\partial^2 B}{\partial n^2} \end{bmatrix} \,. \tag{3.33}$$

When there are more parameters to be calculated in Newton's method, the dimension of the Hassian matrix becomes higher, and it is time-consuming to compute its inverse matrix. Therefore, the quasi-Newton method, which is based on Newton's method, is proposed for solving this problem [95]. The advantage of using the quasi-Newton method is that it does not require the computation of inverse matrix of Hassian. Instead, it uses some methods that are the approximation of the Hassian matrix, such as DFP, BFGS and etc. Further discussion of the quasi-Newton method is beyond the scope of this thesis, here we use the Matlab implementation of the quasi-Newton method for computing parameters.

To conclude, the process of blind source separation method in this chapter is listed in Algorithm 3.1.

3.4 Experiments

In this section, we present an experimental evaluation of our novel method for shape recovery and refractive index estimation, and compare it with alternative methods. Firstly we introduce the approaches of image acquisition which are widly applied in this thesis. The only difference of image acquisition techniques in Chapter 5 and Chapter 6 is that they use polarised light instead of unpolarised light. We have ensured that all the issues in images acquisition are investigated and summarised in Section 3.4.1. Next we show the estimation results using the BSS method in this chapter, and demonstrate its validity by showing the error distribution of the estimates with the ground truth. We choose TRS fitting and method of Saman and Hancock for comparison, our proposed method is proved to perform better than the alternatives.

3.4.1 Image Acquisition

In the thesis we have three experimental devices for image acquisition, which are the light source, polariser and camera. Each one has some issues that might influence the intensities of input data. We have summarised all the problems which need to be investigated, and our solutions to fix those issues in Table 3.1.

Details of the solutions and experiments are provided, which are summarised into four parts: firstly we present the experimental set-up of the devices using the diagram, and our

Algorithm 3.1: The BSS method using Newton's method for polarisation estimation.

Input: The input matrix $\boldsymbol{X}$ containing intensities of three random polarisation images, using unpolarised light.

Output: Maximum and minimum intensities $I_{\max}$ and $I_{\min}$, refractive index n, phase angle ϕ.

begin

- Set the iteration $t = 0$;
- Compute $\boldsymbol{V}$ using SVD method in Equation 3.12;
- Initialise $n^{(0)} = 1.4$, and mixing coefficient matrix $\boldsymbol{A}^{(0)}$ using the constraint in Equation 3.23;
- Initialise $\theta_1^{(0)}$, $\theta_2^{(0)}$ and $\theta_3^{(0)}$ using Equation 3.10;
- **repeat**
  - Compute $\boldsymbol{C}^{(t)}$ using Equation 3.11;
  - Compute $J_{max}^{(t)}$ and $J_{min}^{(t)}$ using Equation 3.6, and convert into $I_{\max}^{(t)}$ and $I_{\min}^{(t)}$, respectively;
  - Compute $\rho^{(t)}$ using Equation 3.21;
  - Compute $\psi^{(t)}$ using Equation 3.22;
  - Compute $Z^{(t)} = \cos\psi^{(t)}$, and $\bar{I}^{(t)} = [I_{\min}^{(t)} + I_{\max}^{(t)}]/2$;
  - Compute mutual information estimation between $Z^{(t)}$ and $\bar{I}^{(t)}$, the result is $B(Z^{(t)}; \bar{I}^{(t)})$;
  - Update $\theta_1^{(t+1)}$, $\theta_2^{(t+1)}$ and $n^{(t+1)}$ using equation of Newton's method: $\Theta^{(t+1)} = \Theta^{(t)} - \eta \boldsymbol{Q}[B^{(t)}]^{-1}\nabla B^{(t)}$, where $\Theta^{(t)} = (\theta_1^{(t)}, \theta_2^{(t)}, n^{(t)})^T$;
  - Update $\theta_3^{(t+1)}$ using the constraint in Equation 3.20;
  - Set iteration $t = t + 1$;
- **until** $[B^{(t)} - B^{(t-1)}]^2 < \epsilon$;
- Compute $\boldsymbol{A}$ using Equation 3.10;
- Compute $\boldsymbol{C}$ using Equation 3.11;
- Compute J_{max} and J_{min} and ϕ using Equation 3.6, and compute $I_{\max}$ and $I_{\min}$ from J_{max} and J_{min}, respectively;

end

Device	Issue	Our solution
Polariser	attenuate light so camera hard to focus and images dim	use manual focus and fixed exposure.
Light Source	has wavelength distribution, might produce polarised light	test to confirm the properties of the source light.
Camera	distorted image brightness in jpeg file by gamma correction	use raw file and dcraw software to prevent the correction.

Table 3.1: The list of problems during image acquisition and the solutions.

solution to the polariser's problem. Then we have two experiments for demonstrating the properties of the source light, which is the wavelength and polarisation status respectively. In the end we describe the solution to the issue of camera, and show how the image are pre-processed to meet the requirements of the proposed methods.

Experimental Set-up

In order to demonstrate the performance and robustness of the proposed method, we have explored it on a variety of objects. Each object was illuminated in the camera viewing direction using an unpolarised collimated light source. A polariser is placed in front of the camera, and three images for each object are collected with different polariser angles. It is noted that we have lowered the position of the light source so that the angle κ between viewing and light direction is as small as possible, in order to fit retro-reflection settings. However, it cannot be so low that the light is then blocked by the camera.

We use manual focus, fixed shutter speed and aperture during the image acquisition. The reason is that the autofocus system is not working well as the light is attenuated, and the acquired image is dim when the light is transmitted through the polariser. Besides, the camera's auto focus and metering functions will try to adjust the settings every time it starts photographing, if manual focus and fixed exposure is not set.

Figure 3.2 shows the experimental set-up for the polarised image acquisition, which is also used in Chapter 4. The image acquisition setting in Chapter 5 and Chapter 6 is similar with what is shown in Figure 3.2, except that there is also a polarising filter placed in front of the light source. In order to avoid light influence from the environment, the images are taken in a dark room where the walls are painted black and the desk is covered with black cloth that absorbs light.

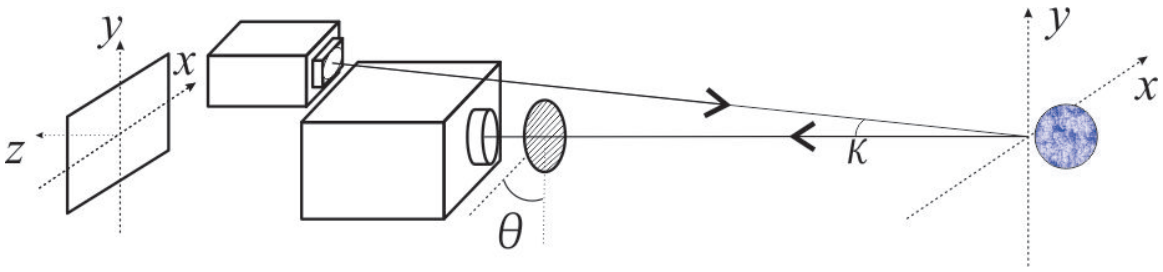

Figure 3.2: The experimental setup for image acquisition.

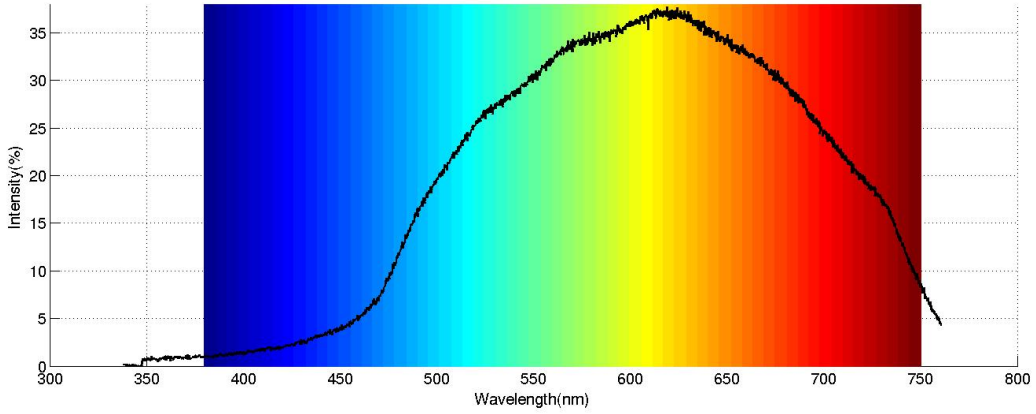

Figure 3.3: The plot of spectrum information for the halogen light used in this thesis.

Wavelength Property of the Light Source

The source light used in image acquisition is a halogen lamp[1], which consists of a glass filled with gas such as argon or nitrogen, and a tungsten filament. The wavelength spectrum of a typical halogen light is shown in Figure 3.3.

From Equations 3.21 and 3.22 it is clear that the measured polarisation depends on both the zenith angle of the surface and the refractive index of the material from which the surface is composed. It has been observed experimentally that the refractive index exhibits a wavelength dependence. Hence there is potentially variation of the measured polarisation at corresponding locations on the surface with wavelength.

The degree to which refractive index varies with wavelength depends on the material. For instance, the phenomenon is responsible for chromatic aberration in lenses. In Table 3.2 we give values of refractive index at different wavelengths taken from the literature for borosilicate glass and gypsum. Figure 3.4 shows how the polarisation varies

[1]Product information is in the web page: http://www.ld-didactic.de/phk/a.asp?a=45063&L=2

Table 3.2: Estimated refractive index of glass and gypsum using three different colour filters.

Colour	Wavelength	Glass	Gypsum
Red	671nm	1.51	1.52
Green	589nm	1.52	1.52
Blue	486nm	1.54	1.53

with zenith angle for refractive indices in the at wavelengths 671nm, 589nm and 486nm, which are typical of red, green and blue light. It is clear that in the case of gypsum, the variation in refractive index is very small, and the has an insignificant effect on the diffuse polarisation. In the case of borosilicate glass, the variations are larger, but the effect on polarisation is again small. Given that these to materials span the range of dielectrics studied in this thesis, the effect of wavelength variation is small and the halogen source can be used without a filter. Finally, it is also noted that Phuoc, Robles-Kelly and Hancock [47] have incorporated the wavelength dependence of refractive index into their spectro-polarimetric method for surface height recovery, and have found benefits when using a wide range of wavelengths extending beyond the visible.

Polarisation Status of the Light Source

Before we start the image acquisition, the source is tested to ensure that the light produced is unpolarised. To demonstrate we take photos of the light from the collimated source, with the polariser placed in front of the camera. There are seven images taken whose polariser angles are: $0°, 30°, 60°, 90°, 120°, 150°, 180°$. We compute the sum of intensities in each image and plot the values in Figure 3.5. The coefficient of variation, which is the ratio of the standard deviation to the mean of seven intensity values, is 0.0068, which shows that the difference between each image is too small and is mainly caused by noise. The plots in the figure do not follow the TRS equation, which also demonstrates that the light is unpolarised.

(a)

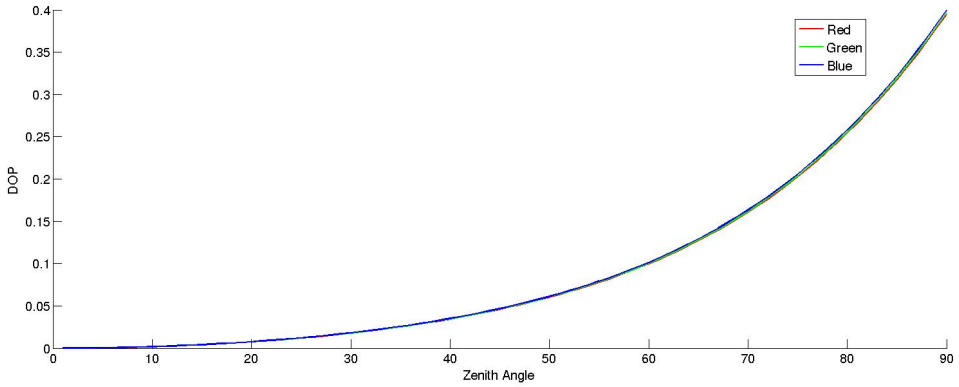

(b)

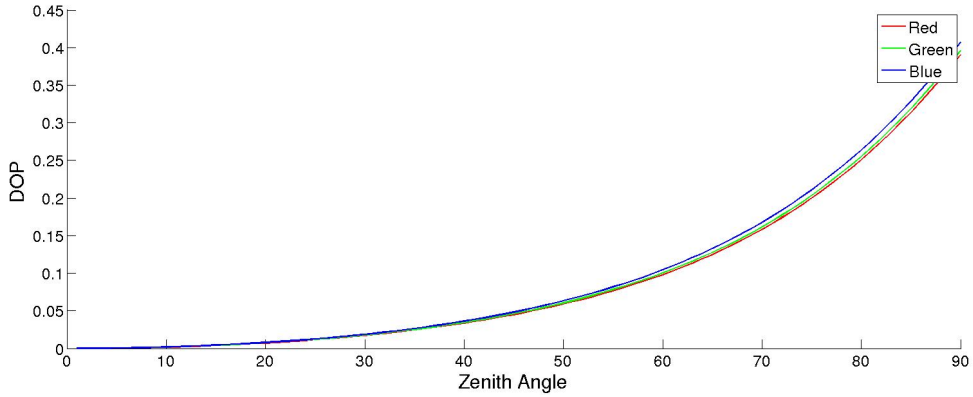

Figure 3.4: Functions of DOP versus zenith angle using red, green and blue lights. The first figure is for glass, while as the second one is for gypsum.

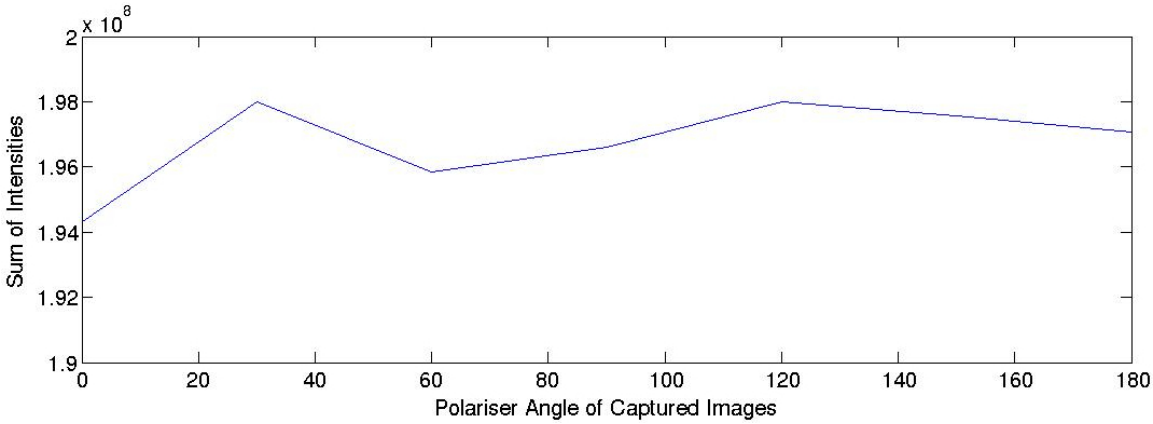

Figure 3.5: The sum of intensities from captured images in different polariser angles for demonstrating the property of source light.

Image Pre-processing

After image acquisition, we have obtained RGB colour images in which each of the pixels has three values representing the intensities of red, green and blue. In this thesis, we convert them to grey level and only focus on surface characteristics estimation from monochrome image inputs, as it is simple for computation. The intensities of the input images range from 0 to 1. The images are taken as raw files, so that its brightness comes directly from the sensor, and is not compressed and modified by the softwares in the camera.

We use the software dcraw to convert the files from raw format to JPEG so that they can be read by softwares such as Matlab in the computer. One of the advantages of using dcraw instead of other conversion software is that it can prevent the modification of gamma curve, which is a non-linear correction to the image intensities to fit with what human eyes observe the light. Figure 3.6 shows the gamma correction, the y axis shows the intensities of the raw file, while the x axis shows the intensities of JPEG file modified by the camera based on the raw file. The blue dots in the figure stand for the same points in the two files, which follows the gamma curve that can influence the shape and reflectance estimation process.

Following the instruction of dcraw software we use "-4" parameter in the command line, which "generates a linear 16-bit file instead of an 8-bit gamma corrected file" [2]. To ensure its validity we photographed a fixed scene and varied the exposure time of the camera, while as all the other settings remained unchanged. We have plotted exposure time versus pixel brightness for each pixel, which shows that the relationship was linear until the point of saturation.

3.4.2 Polarisation Result

The first experiment conducted is to estimate the shape and polarisation state using the proposed BSS method, following Algorithm 3.1. The objects under study are made from different materials, which are a plastic yellow duck, a porcelain bottle, a sponge ball and a plaster owl. Figure 3.7 shows the three input images of sponge ball taken under

[2]Quoted from the online manual of dcraw: http://www.guillermoluijk.com/tutorial/dcraw/index_en.htm.

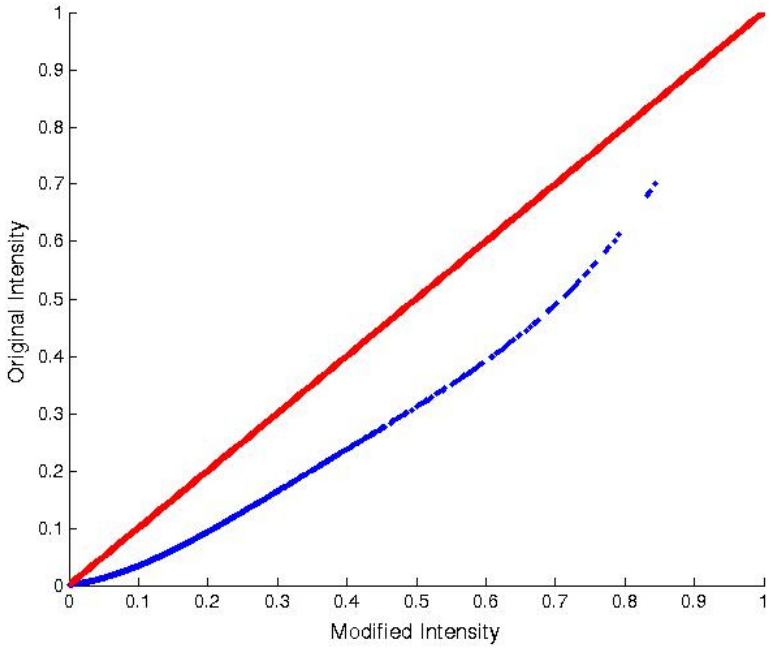

Figure 3.6: The gamma correction using dcraw. The red line shows when the intensity of the input image is equal to the correction result. The blue dots follows the gamma curve, which is used to convert images from raw data in the camera.

polariser angles of 0, 60 and 120 degrees, and we plot the intensity distribution of the row across the centre of the three images. The three images are similar with each other and hard to be distinguished by the eyes. Differences which are such small increases the susceptibility to noise in the estimation process. It is noted that input images for other objects have the same issue. Figure 3.8 shows the results. The four rows show the input image, polarisation, phase angle, and zenith angle for surface normal, respectively. The shape information in the fourth row is consistent with the subjective object shape. This demonstrates that the estimation process works well without the information concerning the polariser angles.

Next we explore the robustness of the method by randomly selecting three images from a longer sequence for the ball object, and check if the results remain unchanged. The polarisation orientations of the three sequences are: a)$30°, 90°, 150°$, b)$60°, 90°, 120°$, c)$0°, 30°, 120°$. The results are presented in Figure 3.9. Polarisation and zenith angles are stable under the selection of different polariser angles. However, there is an offset of 90 degrees in the phase angle. This suggests that we need to use constraints to consistently

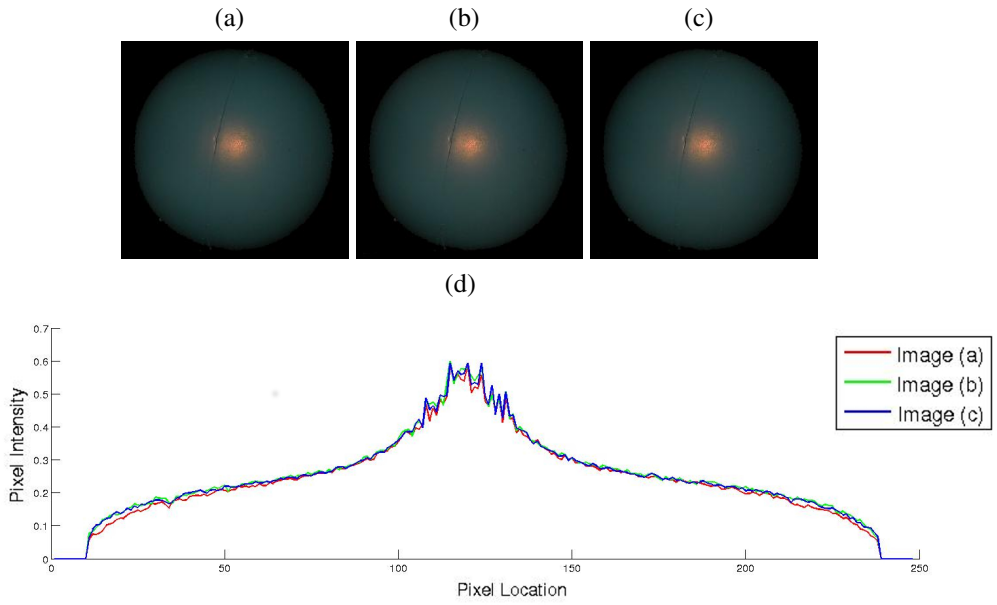

Figure 3.7: The input images taken under the polarisation orientations of 0, 60 and 120 degrees using unpolarised light (a,b,c). Figure (d) shows the intensity distribution of the row across the centre of the three images.

resolve this problem.

Then we compare our method with alternatives. We consider two methods, namely TRS fitting proposed by Nayar *et al.* [71] and the method of Saman and Hancock [89] in Section 2.2.1. We use the same three images to these two methods, and check whose results can correctly recover the polarisation information. In TRS fitting we use the curve fitting function in Matlab for computing the three polarisation parameters in TRS equation, while in Saman and Hancock we apply the method of moments using only three images. Figure 3.10 shows the results for the three methods for the sponge ball, the first row is for DOP and the second the phase angle. There are no significant differences between the three methods for estimating DOP, while our proposed method performs best for the phase angle, in which the distribution of the intensities is valid when representing the azimuth angles for the objects that range only from 0 to 180 degrees.

It is noted that we do not consider the method of Wolff in this experiment, because the TRS equation is actually extended from the Wolff's equation, and can be reformulated to be Wolff's equations in Equation 3.1, Equation 3.2 and Equation 3.3, when using three images whose polariser angles are 0, 45 and 90 degrees. Therefore we use TRS fitting

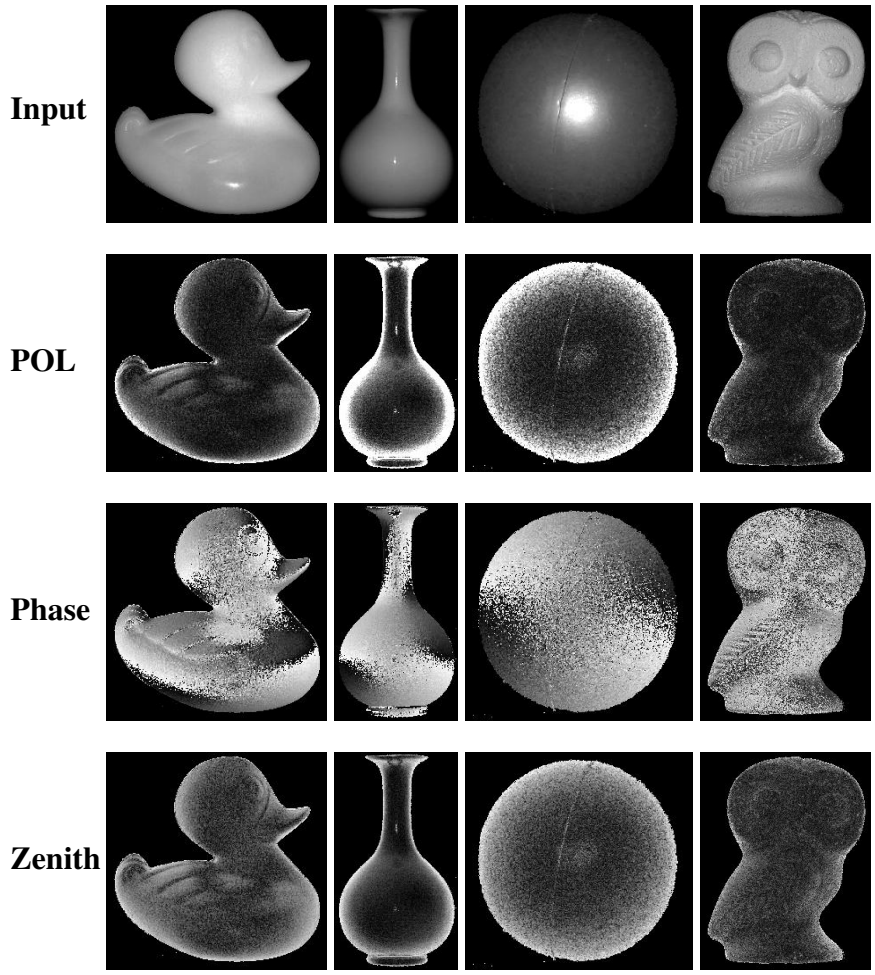

Figure 3.8: The result for shape from polarisation, the first column is one of the input images for each object, the second for DOP, the third for phase angle, and the fourth is for the result of zenith angle for the surface normal. Four rows are for different experimental objects. The brightnesses for all graphs are adjusted to be displayed clearly.

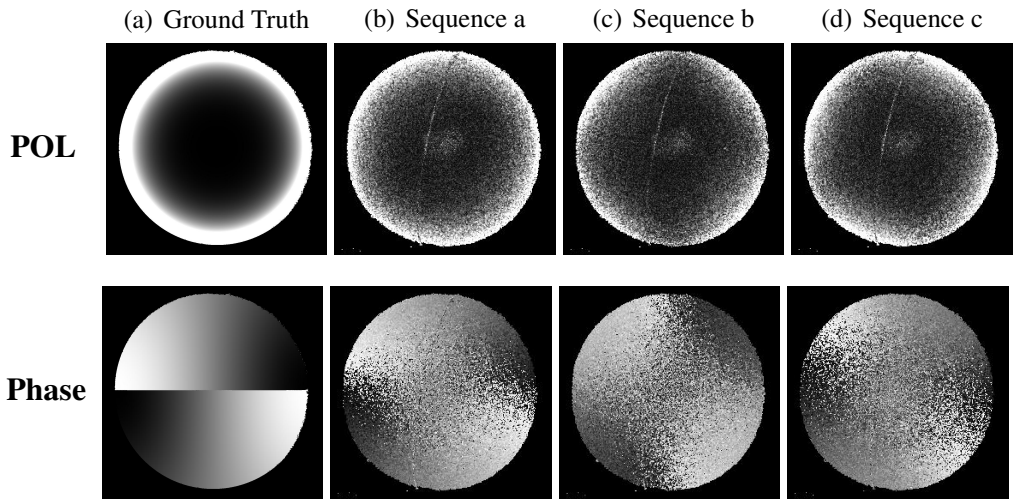

Figure 3.9: The result for the estimation from different sequences, graphs for the first column stand for ground truth data from synthetic data, the rest three columns are for sequence a, sequence b and sequence c respectively.

instead of Wolff's method in this experiment.

Figure 3.11 shows the error distribution of the results in Figure 3.10 compared with the ground truth data. The plots in the figures represent the mean value of the error, while the error bar is the standard deviation value of the distribution. It is demonstrated that our method performs the best as the error of the results is much lower than the other two approaches.

Finally, we explore the application of our method to refractive index estimation. In Table 3.3 we compare the measured refractive index values n_{est} with the tabulated values n_{ref} from five different materials. For the smooth surfaces, the results delivered by our method are all consistent with the tabulated results. However, for rough or indented surfaces such as sponge and plaster the results do not agree well. We attribute this to the effects of surface indentations which cause departures from Lambertian reflectance [3]. Rough surface is considered as microfacets whose orientations are randomly distributed. The external scattering between the facets will reduce the intensity of reflection to the viewer, and the partial polarisation value becomes lower than expected. It is concluded that our method gives relatively accurate results for the refractive index of smooth objects.

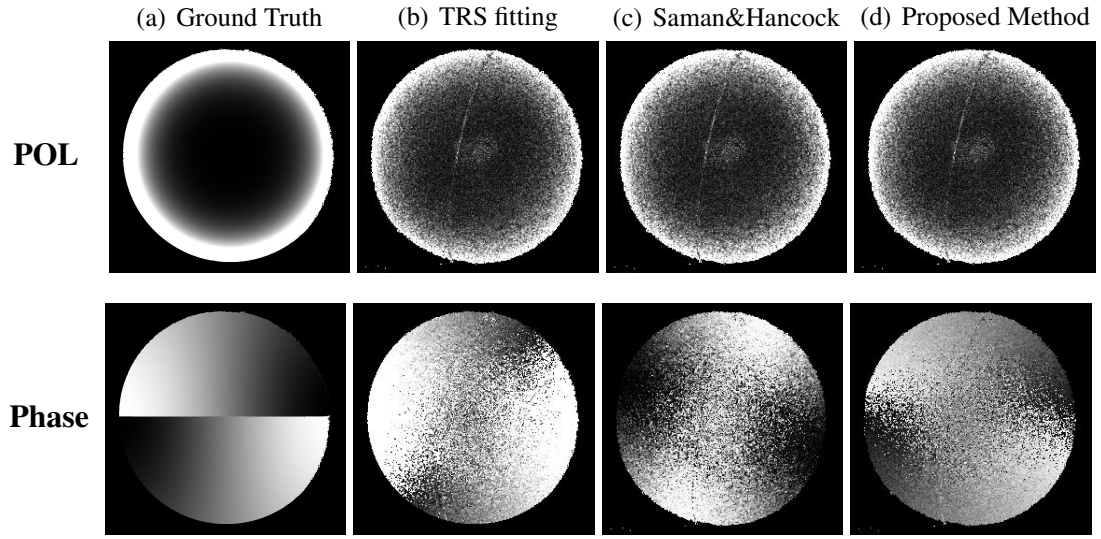

Figure 3.10: The result for the three methods, the brightnesses of all figures have been adjusted.

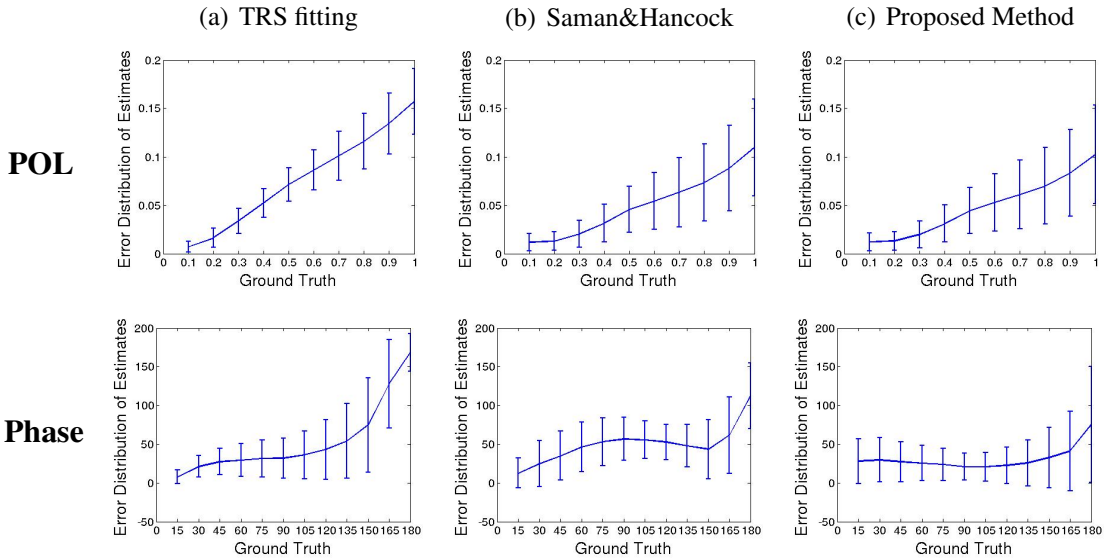

Figure 3.11: The error distribution of the POL and phase angle estimates from three methods with the ground truth data, with the error bar representing the value of standard deviation of the error.

Table 3.3: The list of refractive index estimation results.

Material	n_{ref}	n_{est}
Plastic	1.28	1.23
Apple	1.20	1.17
Plaster	1.46	1.27
Porcelain	1.51	1.56
Sponge	1.48	1.31

3.5 Conclusions

In this chapter we provide a novel method for shape from polarisation and refractive index estimation, which is based on blind source separation. Two constraints are made for the method, firstly the determinant value of matrix $\boldsymbol{W}$ is unity to ensure the stability of the method, and the Equation 3.24 for Newton's method. The proposed method only requires three images without knowing their polariser orientations, which is very convenient when the objects observed are not static, such as human palm and faces. We choose Newton's method instead of exhaustive search in iterative process, for its relatively faster process. In experiment section we demonstrate that the proposed method is both robust and reliable, and performs better than alternative methods. We also show that the method can be used for refractive index estimation, if the surface of the object under study is smooth.

There are several weakness of the works introduced in this chapter which can be improved. Firstly, when developing criterion function we only focus on using the Lambertian model, which is known for its simplicity, but quite weak in predicting reflection and cannot be applied for surfaces that contain strong highlight area. Secondly, we have proved in the experiment section that the method is more robust than the traditional shape from polarisation method, by comparing their performances in phase angle estimation, and using different sequences of three polarised images. However, whether it can retain robustness when the polariser angles are very close to each other is still questionable. Thirdly, in this chapter we only focus on using diffuse Fresnel polarisation model, which has its own weakness as it is vulnerable to noises. It is necessary that we consider other polarisation models for shape recovery.

The solutions of all of these problems are presented in Chapter 4, in which we present a more thorough discussion on some of the issues in polarisation and blind source separation, and novel frameworks are introduced to improve the performances.

Chapter 4

Polarisation Model and Criterion Function

As shown in Chapter 3, we have presented a novel framework that can recover polarisation states using only three images, when their polariser angles are unknown. It has been demonstrated experimentally that the proposed method is capable of calculating robust shape information. In addition, the results are better than with alternative approaches based on the same inputs, especially when the polariser orientations are 0, 60 and 120 degrees.

However, experiments show that the performance of the estimation method in Chapter 3 is reduced when choosing other sequences of three images. Besides, we found experimentally that when the polariser angles of the chosen inputs are very close to each other, such as 0, 30 and 60 degrees, the produced results become unsatisfactory.

Another drawback is that the zenith angle estimates in the previous chapter have residual noise, which occurs for shape from diffuse polarisation, because the values of DOP estimated in this case are low in most pixels, and can be easily influenced by noise from the camera's CCD sensor.

Contribution

The main contribution of this chapter is that we solve the problems addressed above in two different ways: Firstly, we give a detailed overview of Fresnel theory and show how to develop the diffuse and specular polarisation models, which are now widely used. We

discuss their advantages and weaknesses, and propose a novel polarisation probabilistic model that considers diffuse and specular reflections. The probability coefficients in the model are estimated using an iterated conditional modes algorithm, which is an extension of the work of Ragheb and Hancock in [79].

Secondly, we present an improved strategy for developing a criterion function, which is different from the method proposed in Chapter 3 [124]. We show in the previous chapter that the method is not robust enough in estimating phase angle on different sequences of three images, so the criterion function introduced here concentrate on stabilising the variation of phase angle estimation. It has been developed with the aid of SFS; the methodology is presented in Section 4.3.

Chapter Outline

The remainder of this chapter is organised as follows: We start by introducing the Fresnel theory, with the descriptions of Fresnel coefficients and the diffuse and specular polarisation models in Section 4.1. In Section 4.2 we show how to use the proposed probabilistic model and ICM to combine the two polarisation models, and apply the model to shape from polarisation method. In Section 4.3 we present a novel criterion function which improves the estimation of the method described in Chapter 3, with the aid of techniques in SFS. In Section 4.4 we present some experimental results that demonstrate the methods proposed in this chapter.

4.1 Fresnel Theory

In this section we concentrate on investigating Fresnel theory and show how it can be utilised in shape estimation. The Fresnel theory has been mentioned and summarised in Chapter 2 and Chapter 3. Here we focus instead on describing how to develop Fresnel reflection models using Fresnel coefficients and diffuse and specular reflectance properties. The relevant equations are presented and the two Fresnel models are constructed following the works in [3, 6, 116, 117]. Furthermore, we compare the two models and discuss their advantages and drawbacks.

4.1.1 Fresnel Coefficients

The Fresnel equations have been discussed in the following literature [6, 12, 43]. Here we describe the parts of the Fresnel theory that are relevant to this thesis, as the rest is beyond the scope of our research.

Consider the incident light which is resolved into two components whose oscillation directions are parallel to and perpendicular to the plane of incidence as $\Upsilon_{i\perp}$ and $\Upsilon_{i\parallel}$, and the corresponding two reflected wave components as $\Upsilon_{r\perp}$ and $\Upsilon_{r\parallel}$. The amplitude coefficient for the light polarised perpendicular to the plane of incidence $r_\perp$ is defined as the ratio of its reflected wave amplitude $\Upsilon_{r\perp}$ to the incident wave amplitude $\Upsilon_{i\perp}$, which is written as follows:

$$r_\perp(n, \psi_i, \psi_t) = \frac{\Upsilon_{r\perp}}{\Upsilon_{i\perp}} = (\cos\psi_i - n\cos\psi_t)/(\cos\psi_i + n\cos\psi_t) \; . \tag{4.1}$$

where the angles ψ_i and ψ_t are the zenith angle for incident and reflected light directions, and n is the refractive index for the surface. Similarly the other amplitude coefficient for the light polarised parallel to the plane of incidence $r_\parallel$ is defined as

$$r_\parallel(n, \psi_i, \psi_t) = \frac{\Upsilon_{r\parallel}}{\Upsilon_{i\parallel}} = (n\cos\psi_i - \cos\psi_t)/(n\cos\psi_i + \cos\psi_t) \; . \tag{4.2}$$

It is noted that ψ_t can be replaced by ψ_i using Snell's law addressed in Chapter 2, which is

$$\sin\psi_i = n\sin\psi_t \; . \tag{4.3}$$

Therefore the two Fresnel intensity coefficients are obtained by $R_\perp = r_\perp^2$ and $R_\parallel = r_\parallel^2$. Figure 4.1 shows the Fresnel intensity coefficients for a typical dielectric as a function of the incident angle ψ_i. Both the reflection and transmission coefficients are shown, where the latter refers to the ratios of transmitted to incident powers and are defined as follows

$$T_\perp = 1 - R_\perp \; , \tag{4.4}$$

$$T_\parallel = 1 - R_\parallel \; . \tag{4.5}$$

Figure 4.1 shows the reflection and transmission coefficients. It is noted that the point where $R_\parallel = 0$ corresponds to the Brewster angle.

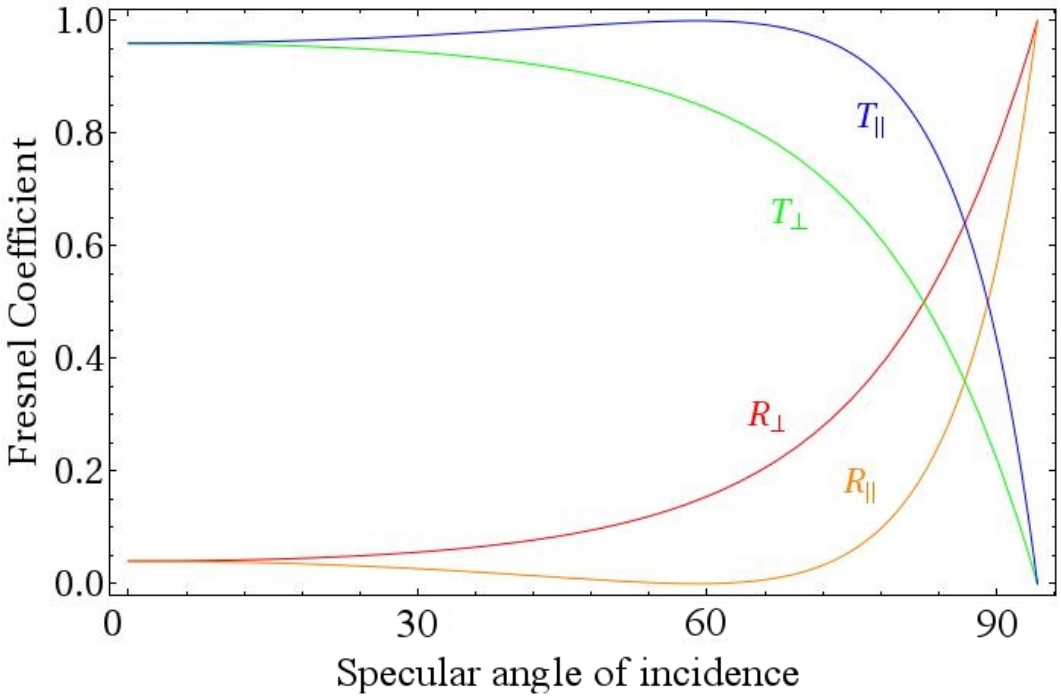

Figure 4.1: Reflection and transmission coefficients for a typical dielectric($n = 1.5$).

4.1.2 The Fresnel Polarisation Models

As stated in the previous chapter, the Fresnel theory can be applied to both diffuse and specular reflections, and thus there are two polarisation models based on the two reflection types. According to [117] we have the four magnitudes of the perpendicular and parallel components for specular and diffuse reflections respectively, denoted as $M_{s\perp}(n,\psi)$, $M_{s\|}(n,\psi)$, $M_{d\|}(n,\psi)$ and $M_{d\perp}(n,\psi)$. The equations are given as follows:

$$M_{s\perp}(n,\psi) = \frac{R_{\perp}(n,\psi)}{R_{\|}(n,\psi)+R_{\perp}(n,\psi)}L_s\,, \tag{4.6}$$

$$M_{s\|}(n,\psi) = \frac{R_{\|}(n,\psi)}{R_{\|}+R_{\perp}(n,\psi)}L_s\,, \tag{4.7}$$

$$M_{d\|}(n,\psi) = \frac{1-R_{\|}(1/n,\psi)}{2-R_{\|}(1/n,\psi)-R_{\perp}(1/n,\psi)}L_d\,, \tag{4.8}$$

$$M_{d\perp}(n,\psi) = \frac{1-R_{\perp}(1/n,\psi)}{2-R_{\|}(1/n,\psi)-R_{\perp}(1/n,\psi)}L_d\,. \tag{4.9}$$

where L_s and L_d are the radiances for specular and diffuse components, whose values are influenced by the object albedo and direction of source light, and are not constant across the surface. It is noted that when the incident light is unpolarised, we denote $I_{smax} =$

$M_{s\perp}(n,\psi)$ and $I_{smin} = M_{s\parallel}(n,\psi)$ as the maximum and minimum intensity values in the transmitted radiance sinusoid (TRS) equation for the specular reflection. Similarly for the diffuse reflection we have $I_{dmin} = 1 - M_{d\perp}(n,\psi)$ and $I_{dmax} = 1 - M_{d\parallel}(n,\psi)$.

Substituting the above equations into the Equation 3.4, we have two models for shape recovery based on diffuse and specular reflection types. The equations for the two Fresnel polarisation models are given as follows:

$$\begin{aligned}
\rho_s(n,\psi_s) &= \frac{I_{smax} - I_{smin}}{I_{smax} + I_{smin}}\,, \\
&= \frac{2\sin^2\psi_s \cos\psi_s \sqrt{n^2 - \sin^2\psi_s}}{n^2 - \sin^2\psi_s - n^2\sin^2\psi_s + 2\sin^4\psi_s}\,, \qquad (4.10) \\
\rho_d(n,\psi_d) &= \frac{I_{dmax} - I_{dmin}}{I_{dmax} + I_{dmin}}\,, \\
&= \frac{(n - 1/n)^2 \sin^2\psi_d}{2 + 2n^2 - (n + 1/n)^2\sin^2\psi_d + 4\cos\psi_d\sqrt{n^2 - \sin^2\psi_d}}\,. \qquad (4.11)
\end{aligned}$$

4.1.3 Discussion

In polarisation vision the diffuse polarisation model is much more widely used than the specular model. There are several reasons for that. Firstly, as shown in Figure 4.1(a), the specular polarisation model has two real solutions for ψ. The ambiguity must be solved beforehand, which is very difficult to do. The second reason, as addressed in Chapter 2, is that special devices are required for determining shape from specular polarisation method. As specular highlight cannot occur over the entire object surface from a single light source, Miyazaki *et al.* [68] used a global light diffuser to solve this problem.

On the other hand, there are also several drawbacks when using the diffuse polarisation model. Firstly, as observed from Figure 4.1(b) most of the DOP values are quite small except when ψ becomes large, especially when n is also low. The estimate accuracy is influenced by noise caused by image quality. Secondly, the diffuse model is much more sensitive to the estimate of refractive index than the specular model. Therefore both polarisation models are unsatisfactory for shape recovery using polarisation measurement. It is also noted that both diffuse and specular reflections are affected by roughness. A rougher surface will reduce the values of DOP, and therefore the zenith angle estimates are underestimated.

(a) Specular Fresnel Model

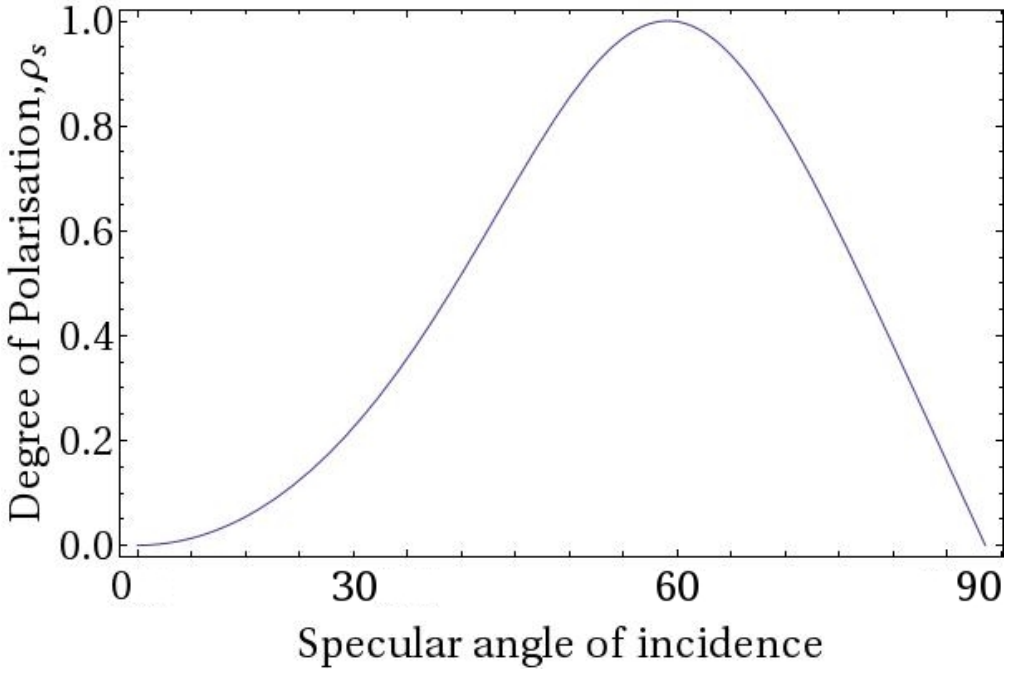

(b) Diffuse Fresnel Model

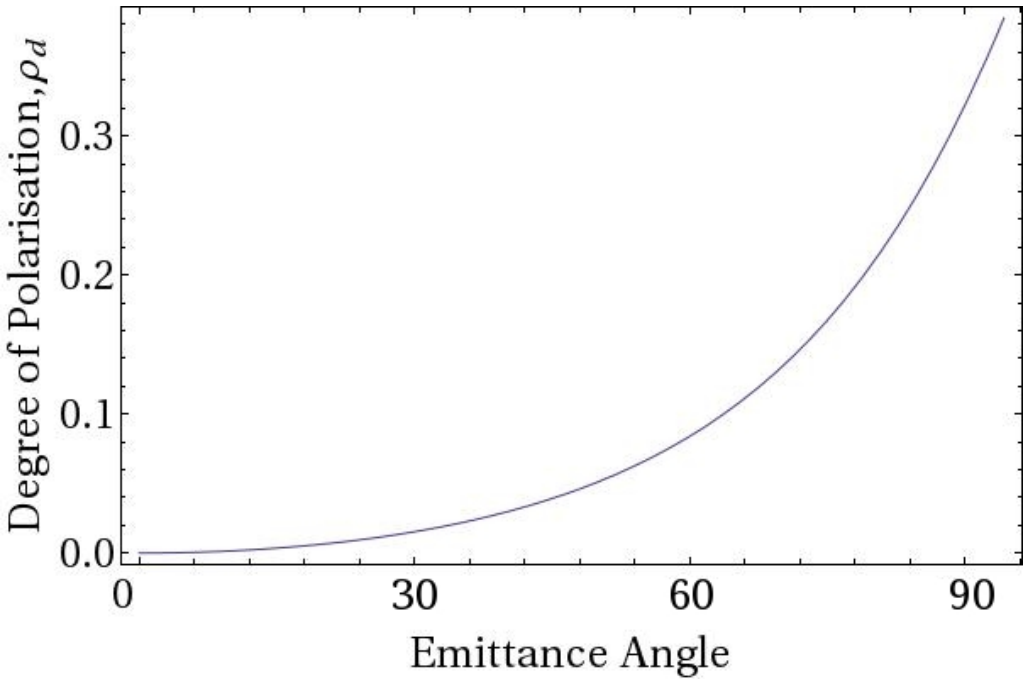

Figure 4.2: Polarisation model for (up) specular and (down) diffuse reflections, $n = 1.5$.

4.2 Probabilistic Model for Shape Recovery

As previously mentioned, both the diffuse and specular Fresnel polarisation models are not ideal for shape recovery. In this section we explore solutions to this problem by developing a probabilistic polarisation model that considers the diffuse and specular reflections simultaneously. The proposed framework is constructed based on the work of Ragheb and Hancock in [79], who introduced a maximum *a posteriori* probability framework for SFS and reflectance component separation. There are many constraints on object surface appearance in the framework. As a result it can only be applied to smooth surfaces with little or no surface texture. Here we utilise the methodology introduced in [79], and show how it can be applied to shape from polarisation method.

4.2.1 Probabilistic Model

According to the two Fresnel polarisation models described in Equation 4.11 and Equation 4.11, the two polarisation parameters ρ_s and ρ_d are related to their corresponding reflectance components, whose values are different. In our probabilistic model we define the measured DOP value by considering both diffuse and specular reflections. As a result the measured value of ρ is related to both the values of ρ_s and ρ_d by a probabilistic model, which is written as follows:

$$\rho = P(\omega_s|\psi_s, \psi_d, \rho_s)\rho_s + P(\omega_d|\psi_s, \psi_d, \rho_d)\rho_d \; . \tag{4.12}$$

where ω_s and ω_d are the class identities meaning that the result estimation ρ is equal to ρ_s or ρ_d, respectively. The $P(\omega_s|\psi_s, \psi_d, \rho_s)$ and $P(\omega_d|\psi_s, \psi_d, \rho_d)$ are the *a posteriori* probabilities that ρ belongs to the class of ω_s or ω_d respectively. The two *a posteriori* probabilities satisfy the following constraints

$$\begin{cases} P(\omega_s|\psi_s, \psi_d, \rho_s) + P(\omega_d|\psi_s, \psi_d, \rho_d) = 1 \; , \\ 0 \leq P(\omega_d|\psi_s, \psi_d, \rho_s) \leq 1 \; , \\ 0 \leq P(\omega_s|\psi_s, \psi_d, \rho_s) \leq 1 \; . \end{cases} \tag{4.13}$$

We also impose a constraint, that for every location in the image the value of ρ is intermediate between ρ_s and ρ_d, given as

$$\min(\rho_s, \rho_d) \leq \rho \leq \max(\rho_s, \rho_d) \ . \tag{4.14}$$

Substituting Equation 4.11 and Equation 4.11 into Equation 4.12, we have the probabilistic model which relates the measured DOP value ρ to the zenith angle estimates, which is the mixture equation as follows:

$$\begin{aligned} \rho \ &= P(\omega_s|\psi_s, \psi_d, \rho_s) \ \frac{2\sin^2\psi_s \cos\psi_s \sqrt{n^2 - \sin^2\psi_s}}{n^2 - \sin^2\psi_s - n^2\sin^2\psi_s + 2\sin^4\psi_s} \\ &+ P(\omega_d|\psi_s, \psi_d, \rho_d) \ \frac{(n - 1/n)^2 \sin^2\psi_d}{2 + 2n^2 - (n + 1/n)^2\sin^2\psi_d + 4\cos\psi_d\sqrt{n^2 - \sin^2\psi_d}} \end{aligned} \tag{4.15}$$

where the zenith angle ψ_d and ψ_s are theoretically identical, because they describes the surface normal information which is measured from the same object.

4.2.2 Iterated Conditional Modes

Our goal in this section is to compute the two *a posteriori* probabilities $P(\omega_s|\psi_s, \psi_d, \rho_s)$ and $P(\omega_d|\psi_s, \psi_d, \rho_d)$ in Equation 4.15, which is to obtain the mixing proportions for diffuse and specular DOP estimates. Here, we apply the ICM algorithm for the estimation. The ICM method was developed for solving the MAP problem. It is an iterative process, which avoids the exhaust search of the MAP estimation that is time-consuming for computation. The method was introduced in computer vision by Besag [13] for restoring the pixel values and eliminating noise. It was also applied to the SFS framework in [79], as it is simple to implement and can produce relatively decent results.

The ICM algorithm interleaves two computational steps in each iteration. Firstly, we estimate the MAP based on the current zenith angle measurement, and then updates the surface normal information based on the current *a posteriori* probabilities estimates. We develop the ICM method based on the following strategy: in each iterative step we firstly compute $\rho_s^{(t)}$, $\rho_d^{(t)}$, $\psi_s^{(t)}$ and $\psi_d^{(t)}$, then compute the zenith angle estimate $\psi'^{(t)}$ according to the Equation 4.24. Next, we use $\psi'^{(t)}$ to compute $\rho_s'^{(t)}$ and $\rho_d'^{(t)}$ and compare them with the corresponding $\rho_s^{(t)}$ and $\rho_d^{(t)}$, using the least square fitting method given by

$$\varepsilon_s^{(t)} = [\rho_s'^{(t)} - \rho_s^{(t)}]^2 , \tag{4.16}$$

$$\varepsilon_d^{(t)} = [\rho_d'^{(t)} - \rho_d^{(t)}]^2 . \tag{4.17}$$

When we found the correct *a posteriori* probabilities of $P(\omega_s|\psi_s, \psi_d, \rho_s)^{(t)}$ and $P(\omega_d|\psi_s, \psi_d, \rho_d)^{(t)}$, the measured ψ' is the correct zenith angle result, thus ρ_s' is equal to ρ_s while ρ_d' is equal to ρ_d. Defining ϵ as the constant number to determine when convergence is reached, we have the criterion function of the ICM method written as follows

$$[\varepsilon^{(t)} - \varepsilon^{(t-1)}]^2 < \epsilon . \tag{4.18}$$

The two probability distributions are defined as $p(\omega_s|\psi_s, \psi_d, \rho_s)^{(t)}$ and $p(\omega_d|\psi_s, \psi_d, \rho_d)^{(t)}$. In this section, they are computed using the error function $\varepsilon_s^{(t)}$ and $\varepsilon_d^{(t)}$, as given by

$$\varepsilon_s^{(t)} = p(\omega_s|\psi_s, \psi_d, \rho_s)^{(t)} , \tag{4.19}$$

$$\varepsilon_d^{(t)} = p(\omega_d|\psi_s, \psi_d, \rho_d)^{(t)} . \tag{4.20}$$

With the probability distributions $p(\omega_s|\psi_s, \psi_d, \rho_s)^{(t)}$ and $p(\omega_d|\psi_s, \psi_d, \rho_d)^{(t)}$ to hand, we develop their *a posteriori* probabilities according to the ICM method, namely $P(\omega_s|\psi_s, \psi_d, \rho_s)^{(t)}$ and $P(\omega_d|\psi_s, \psi_d, \rho_d)^{(t)}$ respectively. Denoting the set $\Omega = (d, s)$ which consists of the diffuse and specular labels, the two *a posteriori* probabilities are updated using the Bayes formula given as

$$P(\omega_s|\psi_s, \psi_d, \rho_s)^{(t+1)} = \frac{p(\omega_s|\psi_s, \psi_d, \rho_s)^{(t)} P(\omega_s|\psi_s, \psi_d, \rho_s)^{(t)}}{\sum_{\Lambda\in\Omega} p(\omega_\Lambda|\psi_s, \psi_d, \rho_\Lambda)^{(t)} P(\omega_\Lambda|\psi_s, \psi_d, \rho_\Lambda)^{(t)}} , \tag{4.21}$$

$$P(\omega_d|\psi_s, \psi_d, \rho_d)^{(t+1)} = \frac{p(\omega_d|\psi_s, \psi_d, \rho_d)^{(t)} P(\omega_d|\psi_s, \psi_d, \rho_d)^{(t)}}{\sum_{\Lambda\in\Omega} p(\omega_\Lambda|\psi_s, \psi_d, \rho_\Lambda)^{(t)} P(\omega_\Lambda|\psi_s, \psi_d, \rho_\Lambda)^{(t)}} . \tag{4.22}$$

4.2.3 Iterative Process

At initialisation of ICM method, we apply the shape from diffuse polarisation method in Equation 4.11 to obtain the shape estimate, which we assume is equal to the specular zenith angle $\psi_s^{(0)}$. Therefore the corresponding specular DOP value $\rho_s^{(0)}$ can be computed

using Equation 4.11. We impose the constraint in the initialisation step that the values of $P(\omega_s|\psi_s,\psi_d,\rho_s)^{(0)}\rho_s^{(0)}$ and $P(\omega_d|\psi_s,\psi_d,\rho_d)^{(0)}\rho_d^{(0)}$ are identical and equal to half of the DOP ρ, which is given as follows

$$P(\omega_s|\psi_s,\psi_d,\rho_s)^{(0)}\rho_s^{(0)} = P(\omega_d|\psi_s,\psi_d,\rho_d)^{(0)}\rho_d^{(0)} = \rho/2\ . \tag{4.23}$$

Using the constraint we can compute $P(\omega_s|\psi_s,\psi_d,\rho_s)^{(0)}$ by $P(\omega_s|\psi_s,\psi_d,\rho_s)^{(0)} = \rho/[2\rho_s^{(0)}]$, then $P(\omega_d|\psi_s,\psi_d,\rho_d)^{(0)}$ by the constraint in Equation 4.13, next $\rho_d^{(0)}$ by $\rho_d^{(0)} = \rho/[2P_d^{(0)}]$, and $P(\omega_d|\psi_s,\psi_d,\rho_d)^{(0)}$ by using the inverse function of the diffuse polarisation model in Equation 4.11. It is noted that we decided not to estimate $\psi_d^{(0)}$ first, but instead choose $\psi_s^{(0)}$, as in that case $\psi_s^{(0)}$ has to be computed by the inverse function of the specular polarisation model in Equation 4.11, which has an ambiguity problem to be solved. The third constraint we make in this framework is that the zenith angle ψ is estimated by the mean values of estimates from two reflections ψ_d and ψ_s, given by

$$\psi'^{(0)} = [\psi_d^{(0)} + \psi_s^{(0)}]/2\ . \tag{4.24}$$

The method of iterated conditional modes is summarised in Algorithm 4.1. It is noted that the proposed algorithm is not used for computing DOP, but demonstrates how to use the proposed polarisation model for shape recovery, when the estimate of DOP and refractive index is known. Here we impose the constraint that the refractive index n is constant for all pixels in the image. We also assume that $n = 1.4$, which is typical of most commonly occurring surfaces [3]. Future work will focus on shape recovery using the proposed polarisation model without the information of refractive index.

4.3 Improved Criterion Function

In this section we develop an improved criterion function in the Newton's method proposed in Chapter 3 by following a different strategy. In the last chapter, the criterion function is constructed to measure the similarity between the estimates from shape from polarisation and the Lambertian model. This guarantees the correctness of the refractive index and zenith angle estimate, but the phase angle information is neglected. Therefore in the experimental section of previous chapter the phase angle results are not satisfactory.

Algorithm 4.1: The ICM method for shape recovery using probabilistic model and unpolarised source light, considering both diffuse and specular reflections.

Input: The degree of polarisation value ρ.

Output: zenith angle result ψ.

begin

  Set iteration $t = 0$;

  Initialise $n = 1.4$,$P(\omega_s|\psi_s, \psi_d, \rho_s)^{(0)}\rho_s^{(0)} = P(\omega_d|\psi_s, \psi_d, \rho_d)^{(0)}\rho_d^{(0)} = \rho/2$;

  Initialise $\psi_s^{(0)}$ using Equation 4.11 and the given ρ, then compute ρ_s using Equation 4.11;

  Compute $P(\omega_s|\psi_s, \psi_d, \rho_s)^{(0)}$ by $P(\omega_s|\psi_s, \psi_d, \rho_s)^{(0)} = \rho/[2\rho_s^{(0)}]$;

  Compute $P(\omega_d|\psi_s, \psi_d, \rho_d)^{(0)}$ by the constraint (Equation 4.13);

  Compute $\rho_d^{(0)}$ by $\rho_d^{(0)} = \rho/[2P(\omega_d|\psi_s, \psi_d, \rho_d)^{(0)}]$;

  Compute $\psi_d^{(0)}$ by Equation 4.11;

  Initialise $\psi'^{(0)} = [\psi_d^{(0)} + \psi_s^{(0)}]/2$;

  repeat

    Compute diffuse and specular DOP values $\rho_s'^{(t)}$ and $\rho_d'^{(t)}$ from the specular and diffuse polarisation models, using the refractive index value $n = 1.4$ and the zenith angle estimation $\psi'^{(t)}$;

    Compute error functions using least square fitting: $\varepsilon_s^{(t)} = [\rho_s'^{(t)} - \rho_s^{(t)}]^2$ and $\varepsilon_d^{(t)} = [\rho_d'^{(t)} - \rho_d^{(t)}]^2$;

    Update the *a posteriori* class probabilities $P(\omega_s|\psi_s, \psi_d, \rho_s)^{(t+1)} = \frac{\exp[-\varepsilon_s^{(t)}]}{\exp[-\varepsilon_s^{(t)}]+\exp[-\varepsilon_d^{(t)}]}$ and $P(\omega_d|\psi_s, \psi_d, \rho_d)^{(t+1)} = \frac{\exp[-\varepsilon_d^{(t)}]}{\exp[-\varepsilon_s^{(t)}]+\exp[-\varepsilon_d^{(t)}]}$;

    Update $\psi_s^{(t+1)} = \psi'^{(t)}$, and update $\psi_d^{(t+1)}$ using the measured $P(\omega_s|\psi_s, \psi_d, \rho_s)^{(t+1)}$, $P(\omega_d|\psi_s, \psi_d, \rho_d)^{(t+1)}$ and the Equation 4.15;

    Compute error function $\varepsilon^{(t)} = \sum_{x,y}[\varepsilon_s^{(t)}(x, y) + \varepsilon_d^{(t)}(x, y)]$;

    Set iteration $t = t + 1$;

  until $[\varepsilon^{(t)} - \varepsilon^{(t-1)}]^2 < \epsilon$;

end

Here our criterion function measures the squared difference between the estimated phase angle $\phi^{(0)}$ with the target phase angle distribution ϕ'. The BSS adopting this criterion function also has some changes. Here we commence by determining the polariser angles based on polarisation theory. Then we use the estimated polariser angles to estimate the degree of polarisation, from which we compute the refractive index using the Fresnel equation.

4.3.1 Phase Angle Estimation

We compute ϕ' by applying a SFS algorithm to the mean brightness computed from the three input polarised images, which is $\bar{I} = (I_{\max} + I_{\min})/2$ mentioned in Section 3.3.1. For the measured surface normals we compute the azimuth angle. SFS recovers surface shape by analysing intensity variations over a single input image. It has been extensively studied for several decades [119, 126]. There are several methods available, and in this paper we choose the geometric SFS algorithm introduced in [119], for its simplicity and robustness.

The azimuth angle information we obtain from SFS method is denoted as γ'. Next we calculate its corresponding phase angle ϕ' based on its definition described in [7]. The least square fitting method is used to compare ϕ' with the estimated phase angle ϕ, the error function for the Newton's method is given by

$$\varepsilon = \sum_{i=1}^{N_x} \sum_{j=1}^{N_y} [\phi(i,j) - \phi'(i,j)]^2 \,. \tag{4.25}$$

The equation for updating the parameter values in Newton's method is similar with the Equation 3.32 in the last chapter. The only difference is that the refractive index value n is not included in the parameter set Θ. Its estimation method is presented in the next section. The process of the phase angle estimation in this section is given in Algorithm 4.2.

4.3.2 Refractive Index Measurement

After the computation of Newton's method described above, the phase angle estimates are obtained, with the polariser orientations of three input images θ_1, θ_2 and θ_3. Using

Algorithm 4.2: The BSS method using the improved criterion function for estimating polariser angles.

Input: The input matrix $\boldsymbol{X}$ containing intensities of three random polarisation images, using unpolarised light

Output: The polariser angles θ_1, θ_2 and θ_3

begin
- Set the iteration $t = 0$;
- Compute $\boldsymbol{V}$ using SVD method;
- Initialise $\boldsymbol{A}^{(0)}$ using the constraint in Equation 3.23;
- Compute $\theta_1^{(0)}$, $\theta_2^{(0)}$ and $\theta_3^{(0)}$ using Equation 3.10;
- **repeat**
  - Compute $\boldsymbol{C}^{(t)}$ using Equation 3.11;
  - Compute $\phi^{(t)}$ using Equation 3.6;
  - Compute error function $\varepsilon^{(t)} = \sum_{i=1}^{N_x} \sum_{j=1}^{N_y} [\phi^{(t)}(i,j) - \phi'(i,j)]^2$;
  - Update $\theta_1^{(t+1)}$ and $\theta_2^{(t+1)}$ using equation of Newton's method: $\Theta^{(t+1)} = \Theta^{(t)} - \eta \boldsymbol{Q} [\varepsilon^{(t)}]^{-1} \nabla \varepsilon^{(t)}$, where $\Theta^{(t)} = (\theta_1^{(t)}, \theta_2^{(t)})^T$;
  - Update $\theta_3^{(t+1)}$ using the constraint in Equation 3.20;
  - Set iteration $t = t + 1$;
- **until** $[\varepsilon^{(t)} - \varepsilon^{(t-1)}]^2 < \epsilon$;

end

the equations introduced in the previous chapter the corresponding DOP value can be computed. Here we show how to measure the refractive index values when the improved criterion function is adopted in the BSS.

Different from the refractive index estimation method in the last chapter, the approach introduced here is greatly simplified as the DOP value is already known, denoted as ρ. The mutual information criterion still measures the similarity of the average intensity $\bar{I}^{(0)} = [I^{(0)}_{\min} + I^{(0)}_{\max}]/2$ and the diffuse reflectance component. This applies over most of the surface, except in the proximity of highlights.

The process of mutual information estimation is similar to the method described in the last chapter; therefore its description is not repeated here. The only part which is different is the equation of Newton's method for updating the parameters presented in Equation 3.32. The parameter set $\Theta^{(t)}$ is replaced with a refractive index value $n^{(t)}$. The process of refractive index measurement is presented in Algorithm 4.3

4.4 Experiments

In this section, we present an experimental evaluation of the two methods proposed in this chapter, and compare them with alternative methods. Input images are the same as what are used in Chapter 3. We start by investigating the performance of the novel Fresnel polarisation model, and compare its performance with the traditional shape from diffuse polarisation method. Next we show the estimation results using BSS adopting the improved criterion function, and demonstrate its robustness by testing its performance on three randomly chosen polarised images.

4.4.1 Probabilistic Model Result

Firstly we use the proposed probabilistic model for shape recovery from the degree of polarisation estimate following Algorithm 4.1, Figure 4.3 shows the results. The objects under study are a plastic duck, a porcelain bottle, two terracotta canteens, a red apple, a plaster owl, a yellow pear and a sponge ball. For each object we take three polarised images, their polariser angles are all $0°$, $60°$ and $120°$. The first row from left to right shows the input images whose polariser orientations are 0 degree. The second row contains the

Algorithm 4.3: The BSS method using the improved criterion function for estimating refractive index.

Input: The input matrix $\boldsymbol{X}$ containing intensities of three random polarisation images using unpolarised light, the measured polariser angles θ_1, θ_2 and θ_3.

Output: The refractive index n.

begin

  Set the iteration $t = 0$;

  Compute A using Equation 3.10;

  Compute C using Equation 3.11;

  Compute J_{max} and J_{min} using Equation 3.6, and convert into $I_{\max}$ and $I_{\min}$, respectively;

  Compute ρ using Equation 3.21;

  Initialise $n^{(0)} = 1.4$;

  repeat

    Compute $\psi^{(t)}$ using Equation 3.22;

    Compute $Z^{(t)} = \cos\psi^{(t)}$, and $\bar{I}^{(t)} = [I_{\min}^{(t)} + I_{\max}^{(t)}]/2$;

    Compute mutual information estimation between $Z^{(t)}$ and $\bar{I}^{(t)}$, the result is $B(Z^{(t)}; \bar{I}^{(t)})$;

    Update $n^{(t+1)}$ using equation of Newton's method: $\Theta^{(t+1)} = \Theta^{(t)} - \eta \boldsymbol{Q}[B^{(t)}]^{-1}\nabla B^{(t)}$, where $\Theta^{(t)} = n^{(t)}$;

    Set iteration $t = t + 1$;

  until $[B^{(t)} - B^{(t-1)}]^2 < \epsilon$;

end

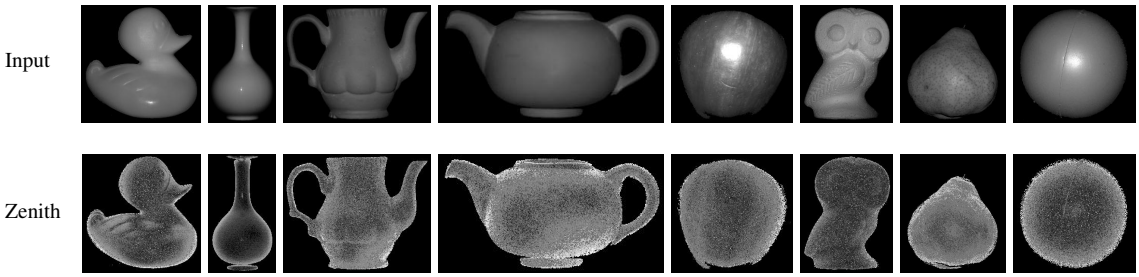

Figure 4.3: The result for shape from polarisation using the probabilistic model, the first row is for the input polarised image, and the second is for the results of zenith angle. The eight columns are for different experimental objects. The brightness of all figures has been adjusted to be displayed clearly.

zenith angle estimates. The results produced are all decent, which prove the validity of the proposed probabilistic model, that it can be applied in the process of shape recovery.

Next we compare the performance with the alternative approach, in which we choose shape from diffuse polarisation. We use plaster owl object for the experiment, and the comparison results are shown in Figure 4.4. The zenith angle estimate on the left is computed from diffuse model, whereas the other one is from the proposed model. Observed from the figures, the performance of the novel probabilistic model performs similar with the alternative polarisation model. We compute their difference and show the error distribution in Figure 4.5, the plots in the figure represent the mean value of difference between the two zenith estimates, with the error bar for the value of variance. The figure also shows that the two results are nearly equal to each other in the range from 9 to 58.6 degrees. It is sensible as research shows that shape estimate using diffuse polarisation model has already been relatively accurate [6].

However, the zenith angle result from the probabilistic model still has residual noise, which can also be seen in Figure 4.3. We attribute this to the fact that the diffuse reflection covers the whole surface, while the specular occurs only in a small area. Therefore diffuse components in the probabilistic model plays a more important role in shape estimation than the specular component. The residual noise in the diffuse DOP value therefore still influence the zenith angle estimate. This suggests that we need to find another way in shape from polarisation for solving this problem.

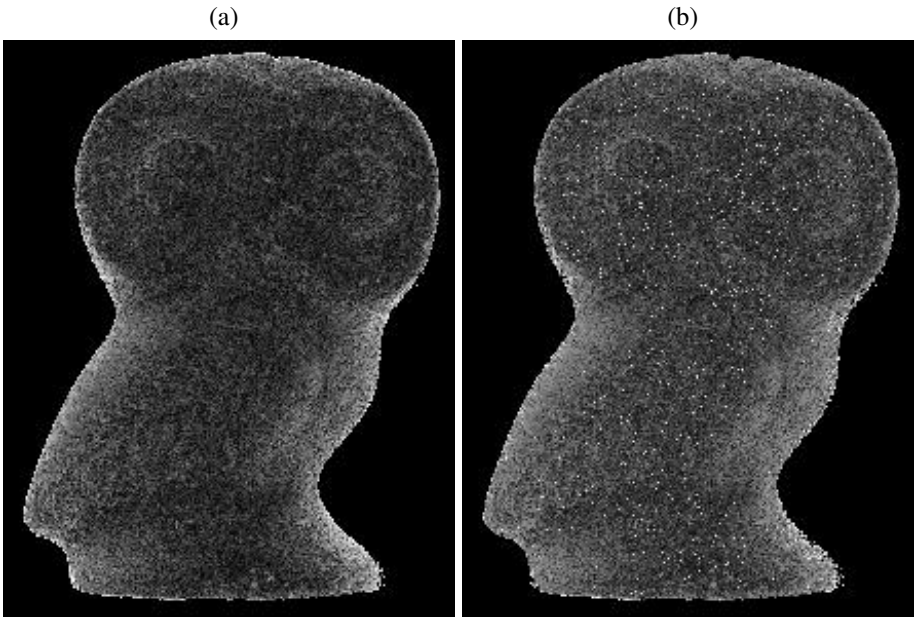

Figure 4.4: The comparison of estimation results between shape from diffuse polarisation (left) and the proposed method (right).

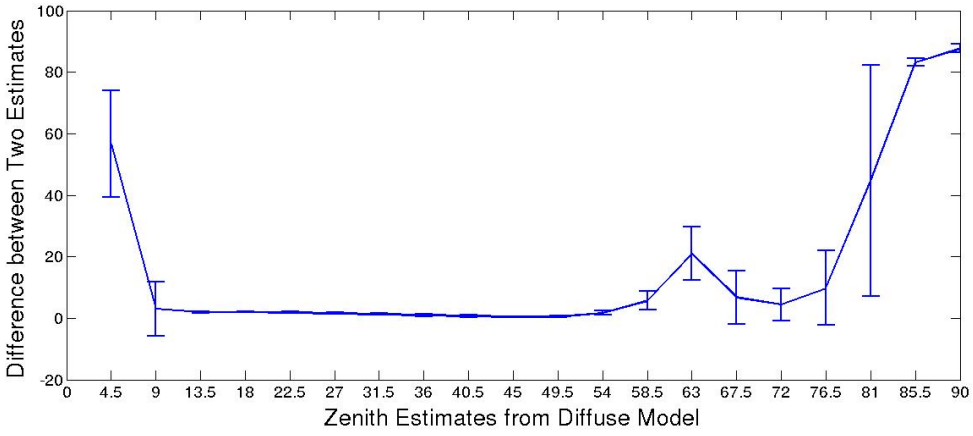

Figure 4.5: The difference distribution of two estimates shown in Figure 4.4. The X axis is the zenith angle from the diffuse polarisation model ranges from 0 to 90 degrees, the Y axis represents the mean value of computed difference between the two results, with the error bar for the variance.

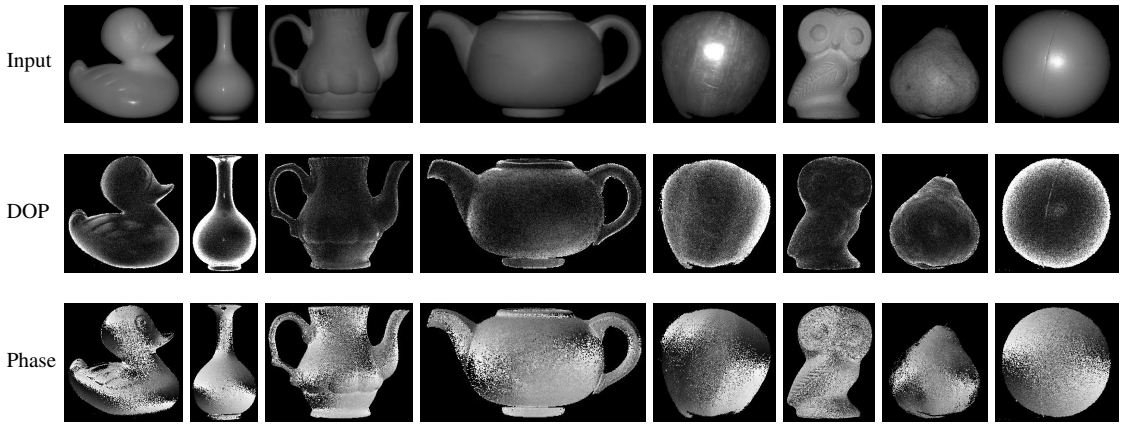

Figure 4.6: Results for shape from polarisation using improved criterion function from eight experimental objects. The first row is for the input polarised image, the second for DOP, and the third is for the result of phase angle for the surface normal. The brightness for all figures has been adjusted to be displayed clearly.

4.4.2 Improved Criterion Function Result

Here we concentrate on demonstrate the validity of the BSS method using the improved criterion function. The first experiment conducted is to estimate the shape of the viewed object together with the polariser angles using the proposed method described in Algorithm 4.2 and Algorithm 4.3. Figure 4.6 shows the results. There are 8 objects in all, which are a plastic duck, a porcelain bottle, two terracotta canteens, a red apple, a plaster owl, a yellow pear and a sponge ball. The three columns show the input polarised image, the estimated DOP and the phase angle. This demonstrates that the estimation process works well without information concerning the polariser angles.

We compare our method with some alternatives. We consider two methods, namely the TRS fitting [71] and the method of Saman and Hancock mentioned in Section 3.1. In order to compare their produced results in a clear way we test the methods using the sponge ball and assume that its shape is completely round. Therefore we create the ground truth zenith angle data for the round object and its phase angle estimate following the theory of polarisation.

Figure 4.7 shows the results for the three methods for the object with ground truth data for reference. The first row is the degree of polarisation and the second the phase angle. There are no significant differences between the three methods for the estimation

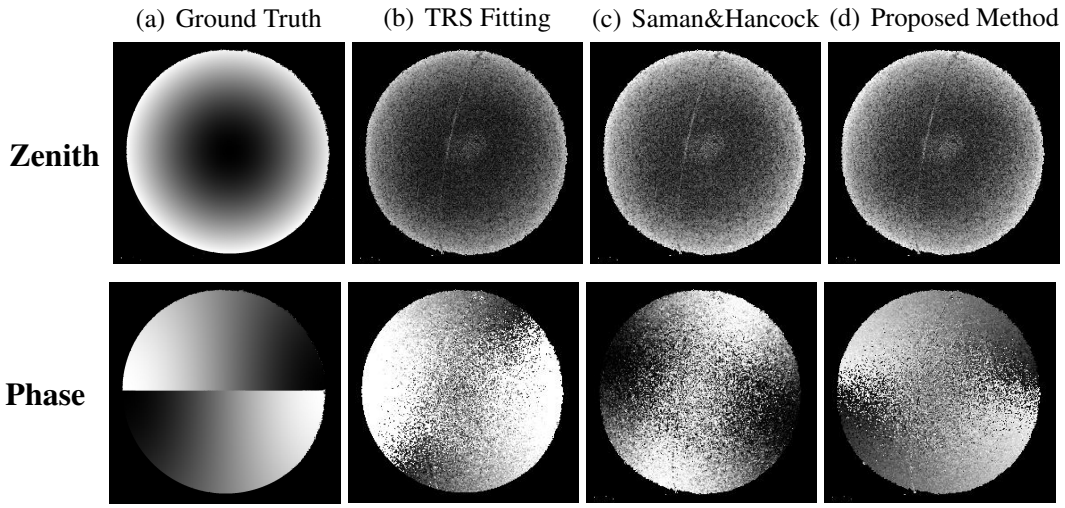

Figure 4.7: The result for the three methods, the brightness have been adjusted.

of the degree of polarisation. However, our proposed method performs better for the phase angle.

Figure 4.8 shows the measured versus ground truth values of zenith and phase angles for the three methods as scatter plots. Ideally the points in the figures should fall on a line of unit slope and zero intercept, commencing at $(0, 0)$ and ending at $(180, 180)$. The main differences between the three methods are in the phase angle. The line in the first graph starts at $(0, 30)$ and ends at $(180, 150)$, while as the estimate for the second is completely wrong. Of the alternatives, our method gives the best regression line.

We also compare the results of three methods in Figure 4.7 with the ground truth data, and Figure 4.9 shows the error distribution with the error bar representing the standard deviation of the comparison. The figure also demonstrates that the results of proposed method are closest to the ground truth data.

We also compare the use of alternative linear transformation algorithms namely PCA and ICA in the BSS. To implement ICA we use the FastICA method introduced in [50], which uses a fixed-point iteration scheme that has a rapid rate of convergence. Figure 4.10 shows the comparison for phase angle estimate, from which the differences between the performances of the three methods can be seen. The results produced by the proposed method are better aligned with the ground truth than those produced by PCA and ICA.

Next we explore the robustness of the method to choice of polariser angle setting. We do this by randomly selecting three images with different polariser angles from a longer

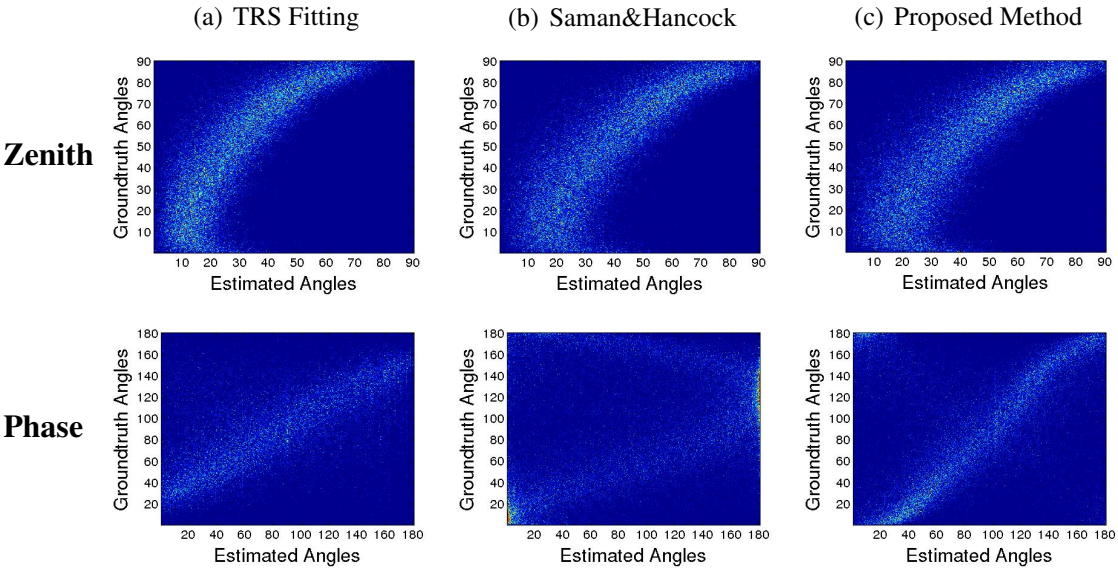

Figure 4.8: The figures of scatter plots which represent the differences between the ground-truth and the results of three methods. The first row shows the zenith angle estimates and the second row is for the phase angle measurements.

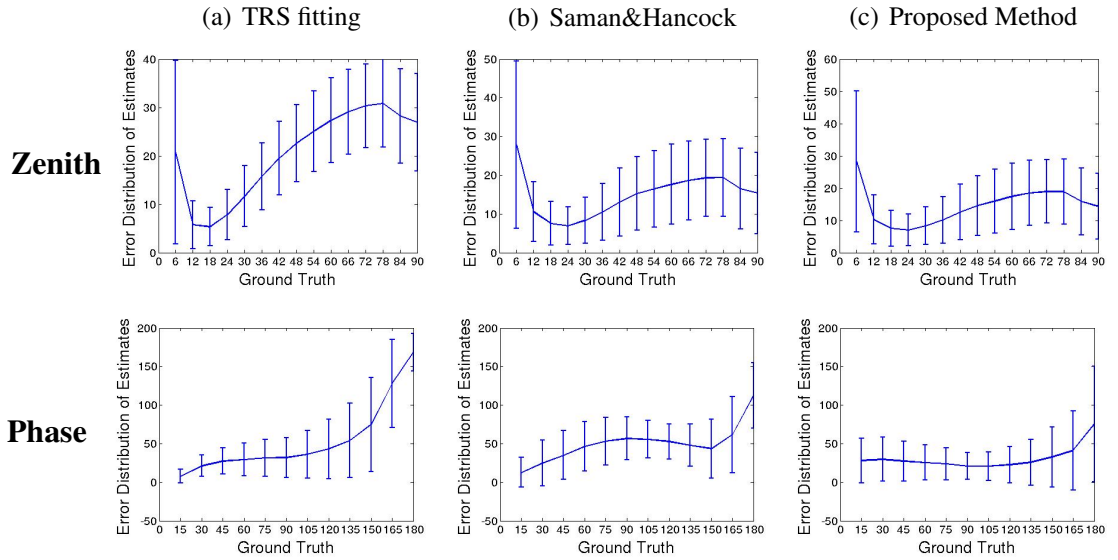

Figure 4.9: The error distribution of the zenith and phase angle estimates from three methods with the ground truth data, with the error bar representing the value of standard deviation of the error.

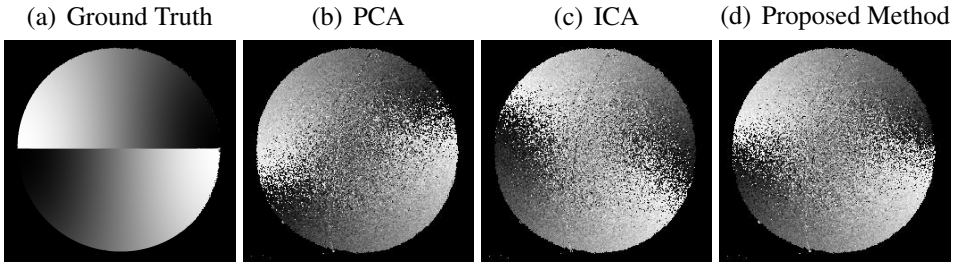

Figure 4.10: The comparison for the phase angle estimates with the synthesised ground-truth, the brightnesses have been adjusted to be displayed clearly.

sequence and check if the results are valid. There are six polarised images in all for the selected object (a ball), whose polariser angles are $0°, 30°, 60°, 90°, 120°$ and $150°$.

We have tested all combinations of polariser angles, and the results are presented in Figure 4.11. The DOP results are not shown, as the differences between them are imperceptible. The estimated phase angles for all 20 combinations appear sensible since they are all consistent with the ground truth image shown in Figure 4.10. This demonstrates that the new criterion function introduced in this chapter can improve the robustness of the BSS method.

The differences between the results are mainly caused by noise in the input images. We have also tested the extreme cases, where the differences of three polariser angles are less than 30 degrees. As the intensity differences between the input images are small, the results produced do not remain stable.

We have also shown the application of our method in refractive index estimation. Similar with what is shown in Chapter 3 we compare the measured refractive index values n_{est} with the tabulated values n_{ref} from five different materials. The estimation results are shown in Table 4.1. The proposed method gives decent results for smooth objects, while it fails to estimate refractive index for rough surfaces, such as sponge and plaster. The reason is the same as given in the last chapter, the roughness of the surface makes the diffuse polarisation model underestimate the correct refractive index values.

4.4.3 Height Map Recovery

In this section the experiment conducted is to use the zenith angle estimates shown in Figure 4.6 for 3D meshes and height map estimation. As we lack the azimuth angle in-

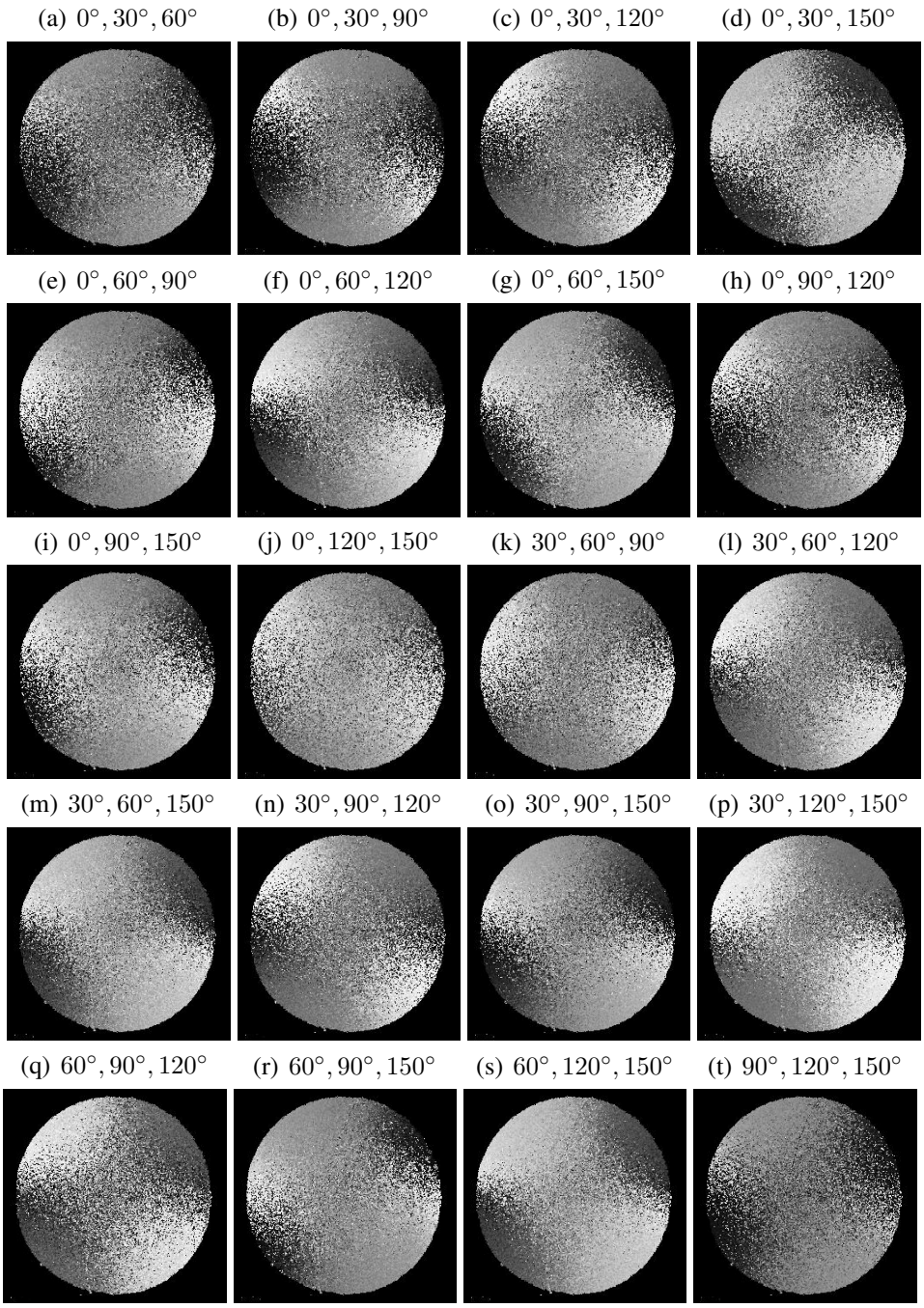

Figure 4.11: The phase angle result for the estimation from different sequences.

Table 4.1: The list of refractive index estimation results using the improved criterion function.

Material	n_{ref}	n_{est}
Plastic	1.28	1.20
Apple	1.20	1.19
Plaster	1.48	1.28
Porcelain	1.51	1.57
Sponge	1.48	1.28

formation for the objects, we use the shapelets method instead [58], which can produce results without the need for the azimuth angle. Figure 4.12 shows the 3D meshes from the zenith angle results presented in Figure 4.6. We have also rendered them in Figure 4.13 using Matlab and a 1.2GHz CPU computer. The results of 3D modelling are sensible, especially for the complex shape objects. However, there are two problems existed in those estimates. Firstly, the residual noise from the zenith angle estimates has also influenced the process of height map recovery. For example, in Figure 4.13(g) the sponge ball has a smooth surface, but the recovered height map shows a rough surface instead. Secondly, as the azimuth angle information lacks, the shapelets method cannot decide whether the surface is convex or concave. As shown in Figure 4.13(e), the nose of the owl is replaced with a hole on its face.

4.5 Conclusions

In this chapter we concentrate on providing solutions to the two problems encountered in the previous chapter. Firstly, we further explore the Fresnel theory and propose a probability polarisation model that considers both diffuse and specular reflection types. To compute the probability coefficients we utilise the iterated conditional modes in the work of Ragheb and Hancock [79].

However, the experimental results show that the performance of the proposed probabilistic model has little or no improvements over the traditional shape from diffuse polarisation method. There is still residual noise in the zenith angle estimate and we therefore

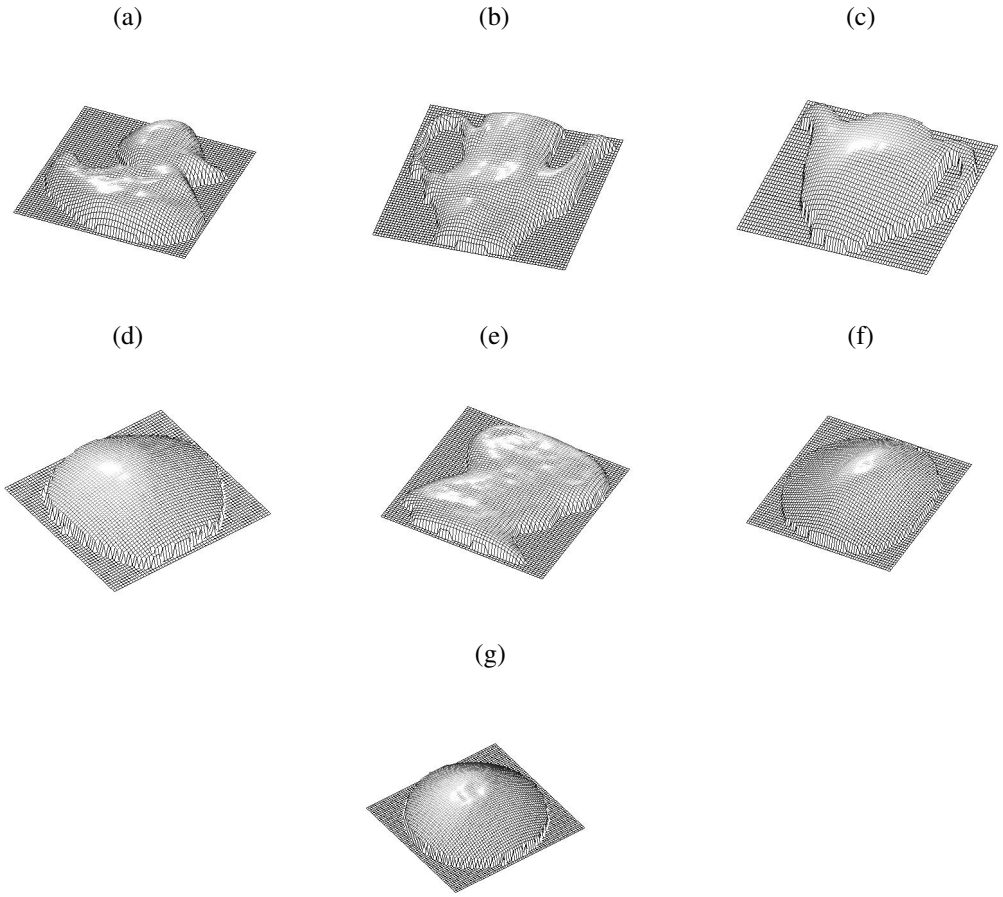

Figure 4.12: The mesh 3D model recovered from the estimated surface normal.

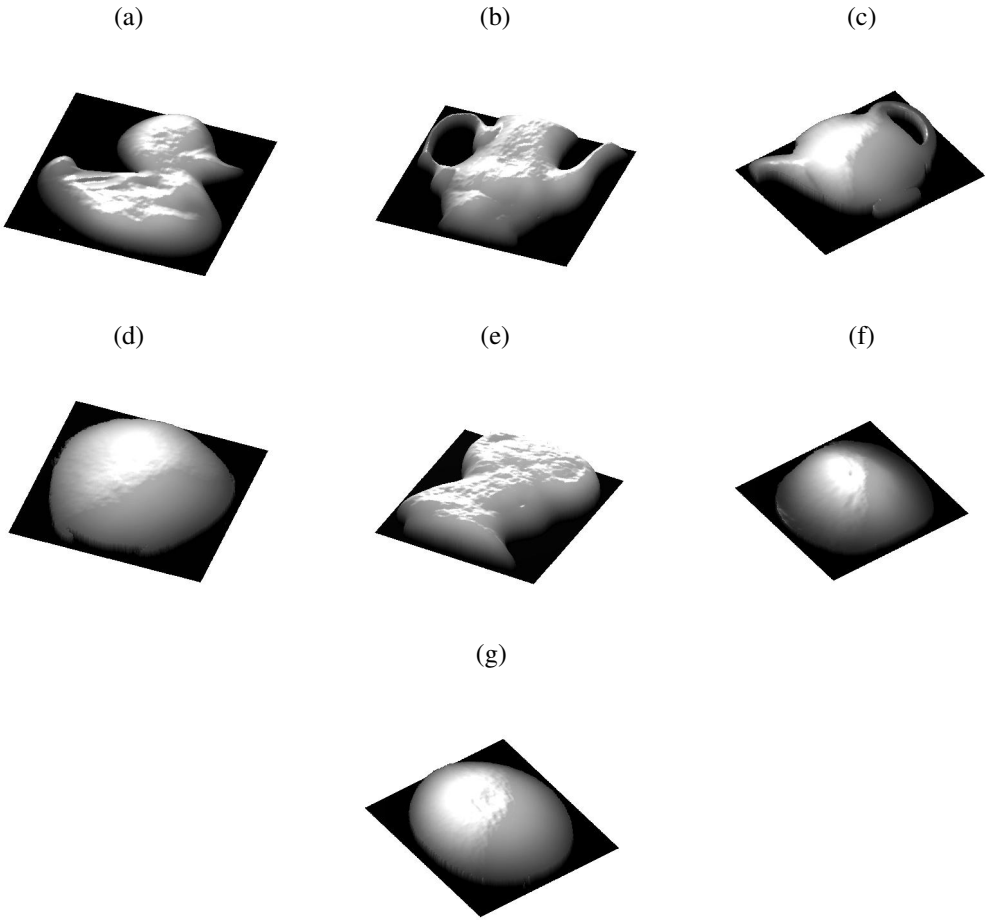

Figure 4.13: The height maps recovered from the estimated surface normal.

need to look for another method for shape recovery using the polarisation method. In the next chapter we present another probability polarisation model, which solves this problem.

We also propose a new criterion function, which improves the robustness of the BSS method given in the previous chapter. It is developed based on a different strategy; we focus on how to produce correct phase angle estimates in this chapter. In the experimental section we demonstrate its performance, and prove that the phase angle results are much better than those shown in Chapter 3.

It is also noted that the refractive index value is assumed to be 1.4 for all the general objects when using the probabilistic model, therefore the algorithm can be simplified. When estimating polarisation using the improved criterion function, the method can also measure the refractive index values, and the results are shown in Table 4.1.

Chapter 5

Shape Recovery using Polarised Light

In this chapter we investigate the techniques using polarised light, and show how the Fresnel polarisation model can be applied here for shape recovery. When the incident light is unpolarised, its reflected ray is partially polarised, meaning that it is difficult to eliminate the specular highlight from the surface. Placing a polarising filter in front of the source light, the objects under study are taken under polarised light. While the diffuse reflectance component remains depolarised, the specular component becomes fully polarised. When the polariser angle is rotated to be perpendicular to the polarising filter orientation, the image taken has no specularities as the specular component is blocked by the polariser. Besides, the Fresnel polarisation models, which are proposed in the previous chapter, can only be applied to the case where the incident light is unpolarised.

We present a novel polarisation model based on Fresnel theory shape recovery that is different from the probabilistic model in the last chapter. Our goal is that the proposed new model for shape recovery can be applied for the images taken under polarised light, and the zenith angle estimate can have its residual noise eliminated. In this chapter we show how to apply the novel model for shape recovery, which is a two stage process. Firstly diffuse and specular components are separated from the input images which are required for the estimation, secondly the proposed polarisation model is used for shape recovery, with the aid of an optimised ICM method, Torrance-Sparrow reflectance model and two reflectance component intensities.

Contribution

We introduce a comprehensive polarisation model, which can recover shape from the DOP using polarised light. The traditional shape from polarisation method has the drawback that the diffuse component remains unpolarised except near occluding contours, where the zenith angle ψ is large. Therefore the DOP values are small for the most part of the image, and the estimation process is strongly influenced by noise, which in turn results in inaccurate surface normal estimations. The proposed model improves the results, as the DOP values are greatly larger in polarised light. However, there are two solutions of zenith angle corresponding to most DOP values. In this chapter we solve this zenith angle ambiguity problem, by using the zenith angle estimates from the chosen parametric reflectance models as a reference.

There are two steps for obtaining this estimate. The process of detailed estimation based on reflectance models can be simplified if the specular and diffuse components are separated beforehand. In the first step we acquire the images in the experiment of polarisation, and separate the components of reflection by applying the method of BSS. We extend the work in Umeyama *et al.* [110] and propose the BSS method whose criterion function is developed specifically for this case. We show in Section 5.3 that the proposed method is capable of separating reflectance components and obtaining phase angle estimates simultaneously.

Secondly we explore the framework, which measures the reflectance properties using parametric reflectance models. With the two reflectance components intensities in hand, we impose the constraint that if the chosen models can accurately describe the reflectance in the surface and the parameters are correct, the surface normals recovered from the two components should have the largest similarity. We choose the Lambertian model for diffuse reflections, and a simplified version of the Torrance and Sparrow model for specular reflection.

When the ambiguity problem is solved, we use a probabilistic framework to recover the zenith angle using the proposed polarisation model, which can be implemented without knowing their parameters. The framework introduced here is also developed based on the work of Ragheb and Hancock in [79]. However, it is optimised for the process of shape from polarisation in this chapter, which is different from the probabilistic model approach introduced in the last chapter. We describe the details of the methodology in

Section 5.2.

Chapter Outline

The organisation of this chapter is as follows. Section 5.1 presents a comprehensive model based on the Fresnel theory introduced in Chapter 4 for shape recovery. Next we introduce the methodologies to recover shape using the proposed model in Section 5.2. Finally, Section 5.3 presents the details of experimental results.

5.1 Polarisation Vision

In Chapter 4 we have summarised the polarisation models available for shape recovery by using the values of refractive index and DOP. In this section we show how the Fresnel theory can be applied when the images are taken under polarised light. Here Malus's law is adopted which describes the properties when polarised light is reflected from the surface of objects. According to the Malus's law, part of the fully polarised light intensity I_0 transmitting through the polariser is blocked. Denote the light intensity that passes through as I, the equation of the Malus's law is given by

$$I = I_0 \cos^2(\theta) \; . \tag{5.1}$$

where θ is the polariser angle. In order to develop the polarisation model, here we also adopt the four magnitudes of the perpendicular and parallel components for specular and diffuse reflections presented in the last chapter, which are given as follows

$$M_{s\perp}(n,\psi) = \frac{R_\perp(n,\psi)}{R_\parallel(n,\psi)+R_\perp(n,\psi)} L_s \; , \tag{5.2}$$

$$M_{s\parallel}(n,\psi) = \frac{R_\parallel(n,\psi)}{R_\parallel+R_\perp(n,\psi)} L_s \; , \tag{5.3}$$

$$M_{d\parallel}(n,\psi) = \frac{1-R_\parallel(1/n,\psi)}{2-R_\parallel(1/n,\psi)-R_\perp(1/n,\psi)} L_d \; , \tag{5.4}$$

$$M_{d\perp}(n,\psi) = \frac{1-R_\perp(1/n,\psi)}{2-R_\parallel(1/n,\psi)-R_\perp(1/n,\psi)} L_d \; . \tag{5.5}$$

Following the work of Wolff and Boult in [117], we have the general expressions for the magnitude of diffuse and specular reflections as

$$M_d(n,\psi) = M_{d\parallel}(n,\psi)\cos^2\theta + M_{d\perp}(n,\psi)\sin^2\theta\ , \tag{5.6}$$

$$M_s(n,\psi) = M_{s\perp}(n,\psi)\sin^2\theta + M_{s\parallel}(n,\psi)\cos^2\theta\ . \tag{5.7}$$

Here we impose the constraint that $M_d(n,\psi)$ and $M_s(n,\psi)$ are regarded as the intensities of diffuse and specular components, which is also stated in [117]. Suppose that the texture of the objects under study is simple, according to the dichromatic model [93] the image intensity $I(n,\psi)$ is decided by the diffuse and specular components using the following equation

$$I(n,\psi) = M_d(n,\psi) + M_s(n,\psi)\ . \tag{5.8}$$

When polarised light is reflected from a surface, the specular component maintains the polarisation state whilst the diffuse component becomes depolarised. As a result the specularity is eliminated in the image when we have the polariser placed in front of the source light, and angles of the two polarisers are perpendicular to each other [25]. Observed from the Malus's law in Equation 5.1, any electric wave whose direction is perpendicular to the incidence plane are blocked, therefore in this case $I_{s\perp}$ is zero. The magnitude for the specular reflectance component becomes

$$M'_s(n,\psi) = M_{s\parallel}(n,\psi)\cos^2\theta\ . \tag{5.9}$$

as a result, the intensity of image is related to the zenith angle and refractive index values using the following equation

$$I(n,\psi) = M_{d\parallel}(n,\psi)\cos^2\theta + M_{d\perp}(n,\psi)\sin^2\theta + M_{s\parallel}(n,\psi)\cos^2\theta\ . \tag{5.10}$$

In [71] the intensity values in the polarised images are related to the polariser angle θ and the phase angle ϕ by the TRS, the equation is introduced in Equation 3.4 of Chapter 3. We replace the maximum and minimum intensity values $I_{\max}$ and $I_{\min}$ in TRS equation, with the Fresnel coefficients in Equation 5.10 to relate ρ to the zenith angle ψ using the following polarisation model

$$\rho = \frac{\frac{R_{\parallel}(n,\psi)}{R_{\parallel}(n,\psi)+R_{\perp}(n,\psi)}L_s + \frac{R_{\parallel}(1/n,\psi)-R_{\perp}(1/n,\psi)}{R_{\perp}(1/n,\psi)+R_{\parallel}(1/n,\psi)-2}L_d}{L_d + \frac{R_{\parallel}(n,\psi)}{R_{\parallel}(n,\psi)+R_{\perp}(n,\psi)}L_s} . \tag{5.11}$$

The novel polarisation model is shown in Figure 5.1. It is noted that in the extreme cases, if the radiance L_s becomes zero, the specular magnitudes in the polarisation model are eliminated. Therefore Equation 5.11 is equal to the diffuse polarisation model introduced in [3], as there is only the diffuse component available which is partially polarised. The polarisation model in that case is shown in (b). On the other hand, when L_d is 0, the DOP ρ becomes 1 for all the values in the matrix as the image is fully polarised, as is shown in (c).

5.2 Methodology

We now consider how the polarisation model can be used for estimating shape from the captured images. As shown in Figure 5.1 there are two ψ values for most values of ρ. This ambiguity problem has to be solved before shape estimation is attempted. In this section we firstly obtain the diffuse and specular reflectance components, then we use numerical inversion of the chosen reflectance models to estimate the zenith angles ψ_d and ψ_s, which are combined as $\psi' = (\psi_d + \psi_s)/2$. Let the two zenith angle results from the estimated as ψ_1 and ψ_2, the ambiguity is resolved by taking the one that is closer to ψ'.

In this section our first goal is reflectance component separation, for which we propose a novel BSS algorithm using three polarised images without polariser orientation information. The advantage of using BSS method over cross-polarisation setting is that the phase angle can also be obtained, which can be used for computing azimuth angle of the surface normal. The BSS method is developed following a different strategy from what is introduced in Chapter 3. The second goal in this section is for shape recovery using the proposed polarisation model. The probabilistic model approach presented in the last chapter is adopted here. We consider L_d and L_s as the two probability coefficients for the probabilistic model, which is the proposed polarisation model. Therefore the iterated conditional modes algorithm can be applied in this section for estimating values of L_d and L_s.

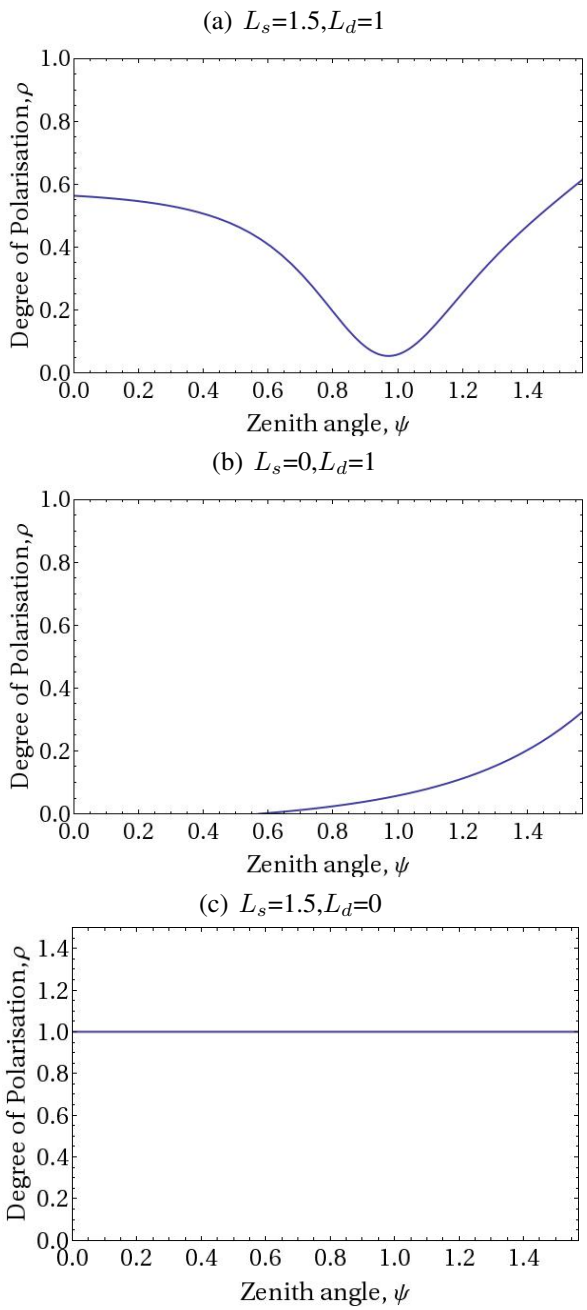

Figure 5.1: The proposed polarisation model, the refractive index n is set to be $n = 1.4$. Figure (a) is the function when the two coefficient values are set as L_s=1.5,L_d=1. Figure (b) and Figure (c) are two extreme cases, the first shows when the specular component is not available, while as the second shows when the diffuse component is none in the reflectance.

5.2.1 Reflectance Component Separation

When scattered light is measured through a linear polarising filter, the intensity changes as the polariser angle θ is rotated [38]. The measured intensity follows the TRS equation introduced in Chapter 3. There are four parameters in the equations, $I_{\max}$ is the maximum brightness, $I_{\min}$ is the minimum, and ϕ is the phase angle, that corresponds to the angle of maximum transmission.

According to the TRS equation in Equation 3.4 the maximum pixel brightness is observed when the polariser is aligned with the angle of polarisation, i.e. $I(\theta = \phi) = I_{\max}$, and the minimum is observed when the polariser is rotated by a further 90 degree in either direction, i.e. $I(\theta = \psi \pm 90^{\circ}) = I_{\min}$. In [71] when using polarised incident light, part of the specular component, denoted as I_{sv}, is changed with the polarisation angles, while as the rest remains constant I_{sc}.

Following the definition in [71] where the diffuse component is $I_d = I_{\min}$, and assuming the specular component $I_s = I_{\max} - I_{\min} = 2I_{sc} = 2I_{sv}$, the TRS equation can be rewritten as

$$I(\theta) = I_d + \frac{I_s}{2} + \frac{I_s}{2}\cos 2\theta \cos 2\phi + \frac{I_s}{2}\sin 2\theta \sin 2\phi \; . \tag{5.12}$$

Our method requires three $N_x \times N_y$ images captured under polariser orientations as θ_1,θ_2 and θ_3. Each image is converted into a long-vector of length $N_x N_y$, and the observation matrix $\boldsymbol{X}$ is denoted as (x_1, x_2, x_3), where x_i is the long-vector by stacking the columns of the i-th polarisation image. We capture the two-components reflectance process using the matrix

$$\boldsymbol{C} = [(J_d + \frac{1}{2}J_s), (\frac{1}{2}J_s \cos 2\phi), (\frac{1}{2}J_s \sin 2\phi)] = [c_a, c_b, c_c] \; . \tag{5.13}$$

In the above, J_d and J_s are long-vectors of length $N_x N_y$ that contain the diffuse and specular reflectance components I_d and I_s as elements. In this section we adopt the BSS method which is introduced in Chapter 3 to compute J_d and J_s. There are two difference between the two BSS approaches presented here and in Chapter 3. Firstly, the method introduced before is applied in the case using unpolarised light, while in this chapter we use polarised light instead. As previously stated, differences between the images taken in

these two illumination environments cannot be neglected. Secondly, the BSS algorithm we apply in Chapter 3 is for polarisation state estimation, while in this section we are aiming at reflectance component separation, the purpose is also different from each other. Therefore, we develop a new novel BSS method, which meets the requirements in this section.

We still apply the Newton's method for measuring the parameter values, while the criterion function is developed following the requirements addressed above. Here we use a smoothness criterion based on the local variance of the diffuse component of intensity. Firstly, we select a set of pixels within the region $G^{(0)}$, where the intensities in the specular component $J_s^{(0)}$ are higher than its mean value. That is

$$i \in G^{(0)}, \text{ if } J_s^{(0)}(i) \geq \bar{J}_s^{(0)}, \quad i = 1, ..., N_x N_y \, . \tag{5.14}$$

where $\bar{J}_s^{(0)} = \frac{1}{N_x N_y} \sum_{i=1}^{N_x N_y} J_s^{(0)}(i)$. Our error criterion is based on the variance of the intensities of the diffuse component over the image region $G^{(0)}$. For iteration t, we therefore have

$$\varepsilon^{(t)} = \sum_{i \in G^{(t)}} [J_d^{(t)}(i) - \bar{J}_d{}^{(t)}]^2 \, . \tag{5.15}$$

where $\bar{J}_d{}^{(t)}$ is the arithmetic mean of $J_d^{(t)}(i)$ for all $i \in G^{(t)}$. When we have correct separation, the intensities of the diffuse component in that region should become approximately uniform. This means that there is neither specularity nor shading information present in $G^{(t)}$, and ε reaches a minimum. The process of reflectance component separation is presented in Algorithm 5.1.

5.2.2 Shape Estimation

In this section we show how to use the proposed polarisation model for shape recovery. Firstly we use numerical inversion of the Lambert and simplified Torrance-Sparrow models [69] to estimate the zenith angles ψ_d and ψ_s, the equations are mentioned in Chapter 2. The parameter value e_s in the Torrance-Sparrow model is computed using the mutual information estimation method presented in the next chapter. We impose the constraint

Algorithm 5.1: The BSS method for reflectance component separation.

Input: The input matrix $\boldsymbol{X}$ containing intensities of three random polarisation images, using polarised light

Output: The separated reflectance components I_d and I_s.

begin
- Set the iteration $t = 0$;
- Compute V using SVD method;
- Initialise $\boldsymbol{A}^{(0)}$ using the constraint in Equation 3.23;
- Compute $\theta_1^{(0)}$, $\theta_2^{(0)}$ and $\theta_3^{(0)}$ using Equation 3.10;
- **repeat**
  - Compute $\boldsymbol{C}^{(t)}$ using Equation 3.11;
  - Compute $J_d^{(t)}$ and $J_s^{(t)}$ using Equation 5.13, and convert into $I_d^{(t)}$ and $I_s^{(t)}$, respectively;
  - Compute mean value of intensities in $J_s^{(t)}$, denoted as $\bar{J}_s^{(t)}$;
  - Set image region $G^{(t)}$ in which $J_s^{(t)} > \bar{J}_s^{(t)}$;
  - Compute error function $\varepsilon^{(t)} = \sum_{i \in G^{(t)}} [J_d^{(t)}(i) - \bar{J}_d{}^{(t)}]^2$;
  - Update θ_1 and θ_2 using equation of Newton's method: $\Theta^{(t+1)} = \Theta^{(t)} - \eta \boldsymbol{Q} [\varepsilon^{(t)}]^{-1} \nabla \varepsilon^{(t)}$, where $\Theta^{(t)} = (\theta_1^{(t)}, \theta_2^{(t)})^T$;
  - Update $\theta_3^{(t+1)}$ using the constraint in Equation 3.20;
  - Set iteration $t = t + 1$;
- **until** $[\varepsilon^{(t)} - \varepsilon^{(t-1)}]^2 < \epsilon$;
- Compute $\boldsymbol{A}$ using Equation 3.10;
- Compute $\boldsymbol{C}$ using Equation 3.11;
- Compute J_d and J_s using Equation 5.13, and convert into I_d and I_s, respectively;

end

that the zenith angle estimate ψ' is obtained by the mean values of ψ_d and ψ_s, which is given by

$$\psi' = (\psi_d + \psi_s)/2 \, . \tag{5.16}$$

Let the two estimates of zenith angle candidates as ψ_1 and ψ_2, the ambiguity is resolved by choosing the one that is closer to ψ'. Consider the correct zenith angle as $\psi^{(0)}$, it is computed using the following equations

$$\psi^{(0)} = \begin{cases} \psi_1, & |\psi_1 - \psi'| \leq |\psi_2 - \psi'| \, , \\ \psi_2, & |\psi_1 - \psi'| > |\psi_2 - \psi'| \, . \end{cases} \tag{5.17}$$

Value of DOP ρ is needed for shape recovery, we use the two reflectance component intensities I_d and I_s, and compute the maximum and minimum intensities using the constraints made in Section 5.2.1, which are $I_d = I_{\min}$ and $I_s = I_{\max} - I_{\min}$. Then we compute ρ following Equation 3.21. There are three parameters to be considered when using the proposed model for shape recovery, which are the refractive index n of the surface and the two radiances L_s and L_d. To compute the two radiances we use a method similar to ICM to estimate the posterior mean zenith angle. We commence by developing a probabilistic model, which is written as:

$$\psi = P(\omega_s|L_s, L_d, \psi_s)\psi_s + P(\omega_d|L_s, L_d, \psi_d)\psi_d \, . \tag{5.18}$$

where $P(\omega_s|L_s, L_d, \psi_s)$ and $P(\omega_s|L_s, L_d, \psi_d)$ are the *a posteriori* probabilities of the specular and diffuse components, satisfying

$$P(\omega_s|L_s, L_d, \psi_s) + P(\omega_d|L_s, L_d, \psi_d) = 1 \, , \tag{5.19}$$

$$0 \leq P(\omega_s|L_s, L_d, \psi_s) \leq 1 \, , \tag{5.20}$$

$$0 \leq P(\omega_d|L_s, L_d, \psi_d) \leq 1 \, . \tag{5.21}$$

where ω_s and ω_d are the class identities for the specular and diffuse radiance class. For every location in the image the value of ψ is intermediate between ψ_s and ψ_d, which is

$$\min(\psi_s, \psi_d) \leq \psi \leq \max(\psi_s, \psi_d) \, . \tag{5.22}$$

The iterative process used for estimation is similar with the ICM method introduced in the last chapter. There are several changes in the ICM method which is implemented here, firstly the polarisation model proposed in this chapter is different from the probabilistic model in Chapter 4. Secondly, the input data here is the zenith angle estimates from diffuse and specular components, which are used here as the reference for computing the zenith angle by the proposed polarisation model. Therefore we develop the ICM method based on a strategy which is different from the approach proposed in Chapter 4. The iterative process is given in Algorithm 5.2.

Algorithm 5.2: The ICM method for probabilistic model using polarised light

Input: DOP value ρ, the diffuse and specular zenith angle estimates ψ_s, ψ_d.

Output: zenith angle result ψ.

begin

  Set iteration $t = 0$;

  Initialise $n = 1.4$, $P(\omega_s|L_s, L_d, \psi_s)^{(0)} = P(\omega_s|L_d, L_d, \psi_s)^{(0)} = 0.5$, and $\psi^{(0)}$ using Equation 5.18;

  repeat

    Compute $I_s^{(t)}$ and $I_d^{(t)}$ using $\psi^{(t)}$ and the Lambertian and Torrance-Sparrow model using the parameter e_s;

    Let $\varepsilon_s^{(t)} = [I_s - I_s^{(t)}]^2$ and $\varepsilon_d^{(t)} = [I_d - I_d^{(t)}]^2$, then the updated *a posteriori* class probabilities are $P^{(t+1)}(\omega_s|L_s, L_d, \psi_s) = \frac{\exp[-\varepsilon_s^{(t)}]}{\exp[-\varepsilon_s^{(t)}]+\exp[-\varepsilon_d^{(t)}]}$ and $P^{(t+1)}(\omega_d|L_s, L_d, \psi_d) = \frac{\exp[-\varepsilon_d^{(t)}]}{\exp[-\varepsilon_s^{(t)}]+\exp[-\varepsilon_d^{(t)}]}$;

    Update $\psi^{(t+1)}$ using Equation 5.18;

    Update $L_s^{(i+1)}$ and $L_d^{(i+1)}$ using the proposed polarisation model in Equation 5.11;

    Compute error function $\varepsilon^{(t)} = \sum_{x,y}[\varepsilon_s^{(t)}(x, y) + \varepsilon_d^{(t)}(x, y)]$;

    Set iteration $t = t + 1$;

  until $[\varepsilon^{(t)} - \varepsilon^{(t-1)}]^2 < \epsilon$;

end

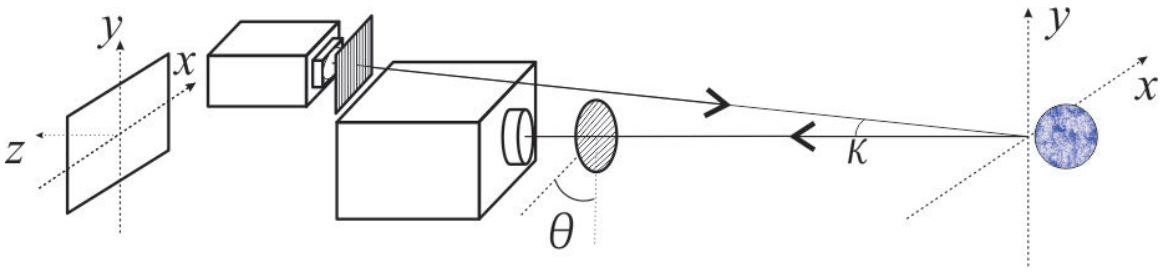

Figure 5.2: The experimental setup for image acquisition using polarised lights. Notice that a polarising filter is attached in front of the source light.

5.3 Experiments

In this section we present the experiments with our new method for estimating shape. We commence by demonstrating the performance of proposed method for reflectance component separation, the estimates are vital for the shape recovery in this chapter. Next we use the novel polarisation method and ICM method introduced in the last section for shape recovery, and compare the zenith angle estimate with the result computed using traditional shape from diffuse polarisation. In the end we provide the 3D meshes and height map from the surface normal estimates.

During the acquisition we placed a vertical polarisation filter in front of a collimated light source, so that the objects are illuminated by polarised light in the direction of the camera (frontal illumination). There was also a polariser in front of the camera, which can be rotated and change the intensities of input images following the equation of transmitted radiance sinusoid (TRS) introduced in Section 3.1.1. Figure 5.2 shows the devices used for image acquisition.

5.3.1 Separation Result

The first experiment conducted is reflectance component separation from input images taken using a polarised light source, following Algorithm 5.1. There are three experimental objects under study, which are a green apple, a yellow pear, and an orange. Figure 5.3 shows the three input images of the green apple under the polariser angles of 0, 60 and 120 degrees, and we plot the intensity distribution of the row across the centre of the three images. Differences between the three input images are much larger than the three input

images taken using the unpolarised light, which are shown in Figure 3.7. The results of this experiment are presented in Figure 5.4. The first column shows the image obtained with the incident light polariser at an angle of 0 degrees (vertical), the specular and diffuse separations are shown in the second, third and fourth columns, and the phase angles in the fifth column. The standard method uses the Equation 5.12 of TRS to perform the separation, which requires the polariser angle information of the input images.

Comparing the results of our method with that of the standard one, it can be seen that some specularity remained on the surface of the apple using the TRS fitting. Using our method by contrast, the shininess has been fully eliminated. The results clearly demonstrate therefore, that using our method the knowledge of polariser angle is not required, while the result of separation remains quite satisfactory. We also compare our result with another traditional approach, which is cross-polarisation setting introduced in Chapter 1. Figure 5.5 shows the differences between the two methods, the first figure is the diffuse component from the proposed method, while the second figure is taken following the cross-polarisation setting. It is shown that the two results are hard to be distinguished, which is also demonstrated in Figure 5.6, in which the mean value of difference between the two estimates is less than 0.008, which can be considered as trivial.

Next we explore the application of our method to colour images. Here we have investigated samples of human skin. The colour images are decomposed into red, green and blue channels, and the separation process is applied to each channel in turn. The specular and diffuse components in the different channels are then recombined to give composite separations [34]. Figure 5.7 shows the results obtained, with the usual column ordering. The specular separation is good, and removes the shininess from the surface of the skin.

5.3.2 Shape Recovery Result

In this section we use the novel polarisation model and the ICM method proposed in this chapter to recover shape, following Algorithm 5.2. We have used 12 objects for experiments, which are green and red apples, a sponge ball, two human faces, two terracotta models, one human palm and a plaster owl. The experimental results are shown in Figure 5.8. The figures demonstrate that the estimation process works well using the new polarisation model.

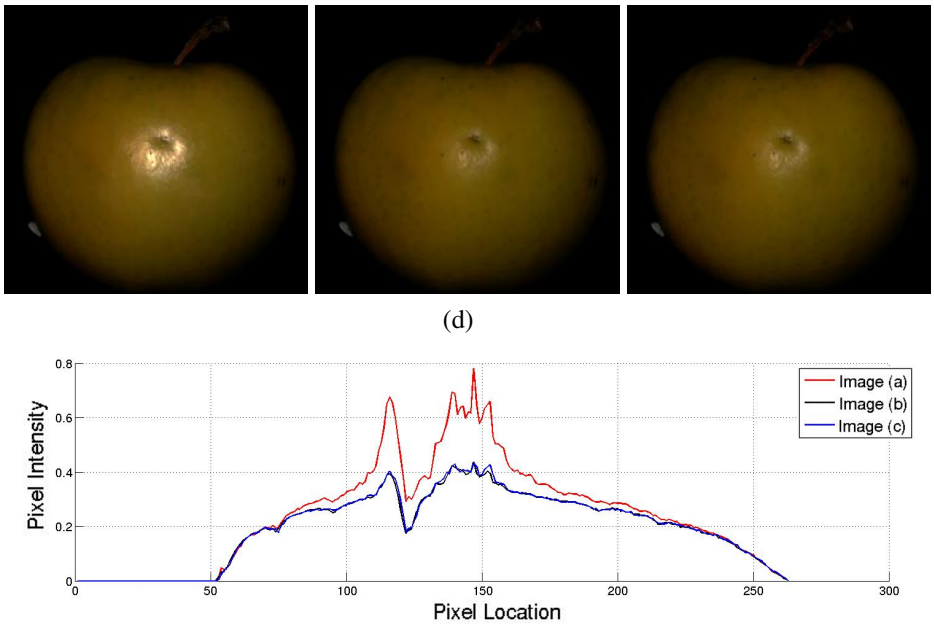

Figure 5.3: The input images taken under the polarisation orientations of 0, 60 and 120 degrees using polarised light (a,b,c). Figure (d) shows the intensity distribution of the row across the centre of the three images.

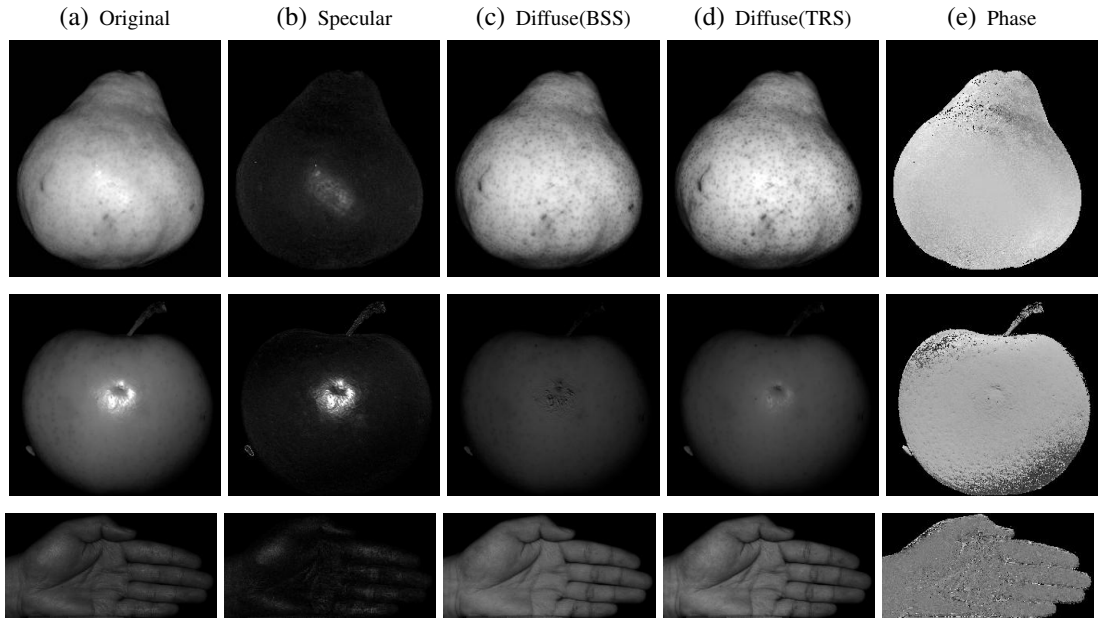

Figure 5.4: Results for selected objects under polarised incident light. Columns from left-to-right, example input image (0 degree polariser), diffuse, specular and phase-angle. Images in the third and fourth columns are the comparison of diffuse component between our method and the standard method. The image contrast has been adjusted to improve clarity.

(a) Proposed method

(b) Cross-polarisation

Figure 5.5: Comparison between the proposed method(a) and cross-polarisation setting(b).

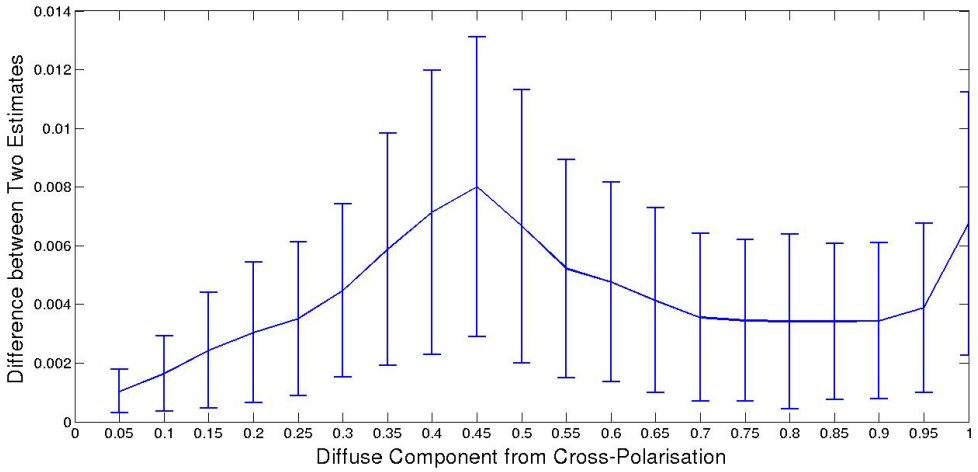

Figure 5.6: The difference distribution of two estimates shown in Figure 4.4. The X axis is the intensity of diffuse component from cross-polarisation method ranges from 0 to 1, the Y axis represents the mean value of computed difference between the two results, with the error bar for the variance.

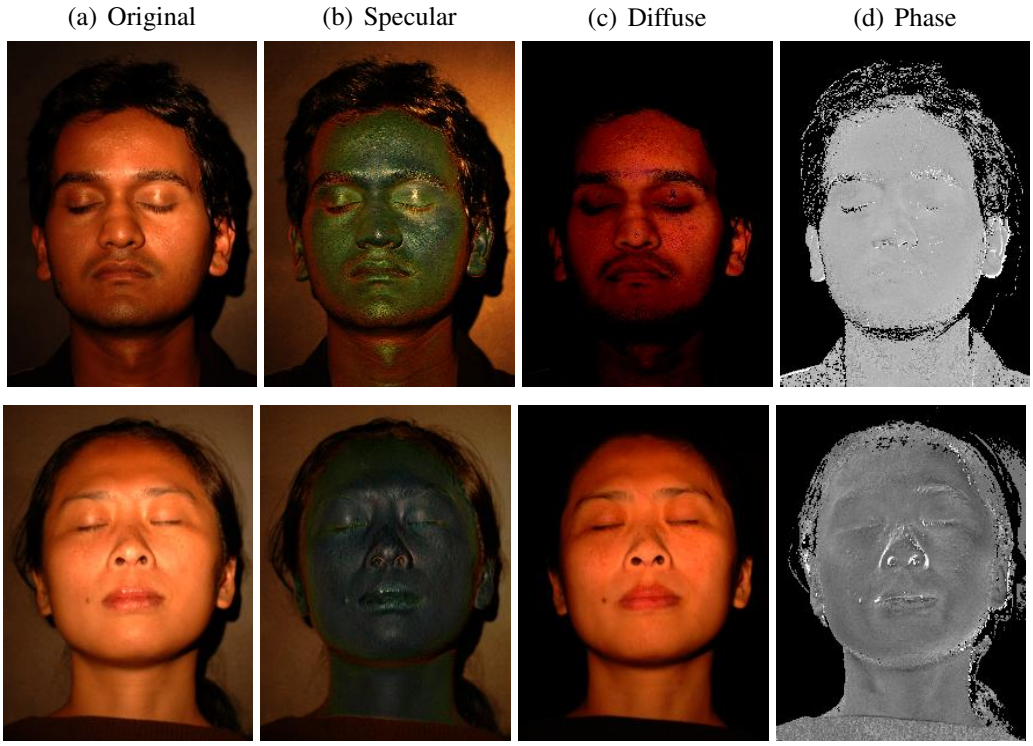

Figure 5.7: Example results for colour images.

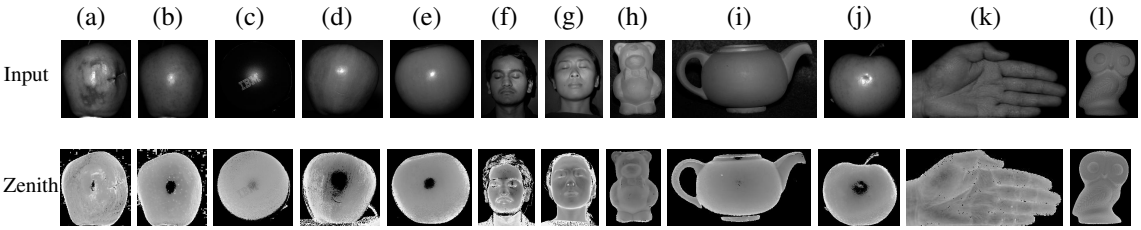

Figure 5.8: The shape results for 12 objects. The first row shows the input images and the figures in the second row show the surface normal estimations.

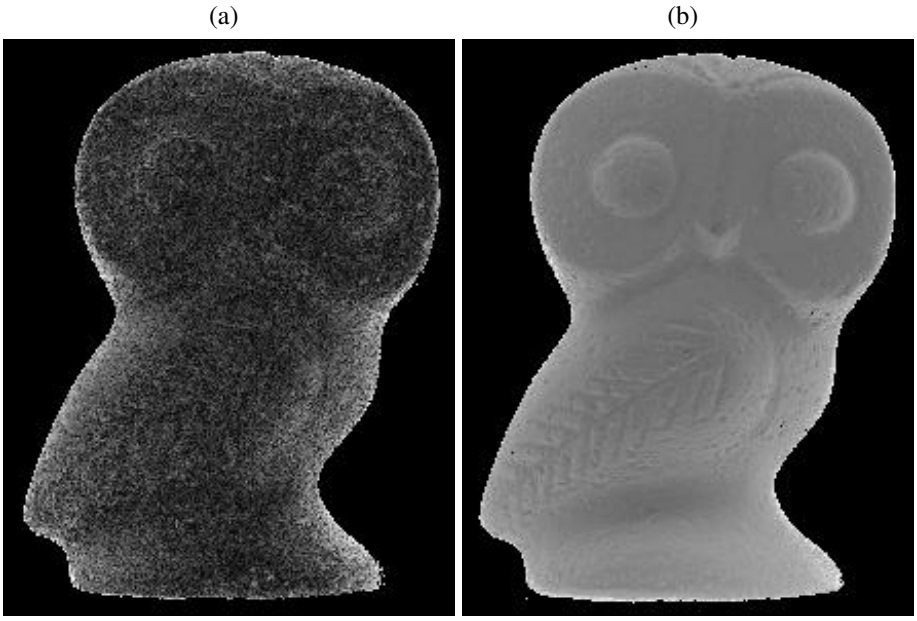

Figure 5.9: The comparison of estimation results between shape from diffuse polarisation (a) and the proposed method (b).

Next we compare our method with the alternatives. In Figure 5.9 the left figure is the zenith angle estimated using the shape from diffuse polarisation using linear polariser described in [3], whilst the right hand figure is the result of using the method reported in this chapter. There is a significant amount of noise in the left hand figure, while the surface in the right hand figure is much smoother. It should also be noted that although such noise can be eliminated using simple smoothing process in [3], the details of the surface are eroded by this process. Difference between the two estimates is shown in Figure 5.10.

Finally, we provide experiment to recover the height map and 3D meshes for the objects using the surface normal estimates. There is two information required for surface normal of the surface, one is zenith angle which is shown in Figure 5.8, the other is the azimuth angle which theoretically can be computed from the phase angle estimates. Because of the problem of azimuth angle ambiguity described in Chapter 3, it is very difficult to obtain the azimuth angle in the polarisation vision. We also use the shapelets method introduced in [58], which does not require the need of azimuth angle when computing height map.

Figure 5.11 shows some of the results in the form of meshes, and we have rendered

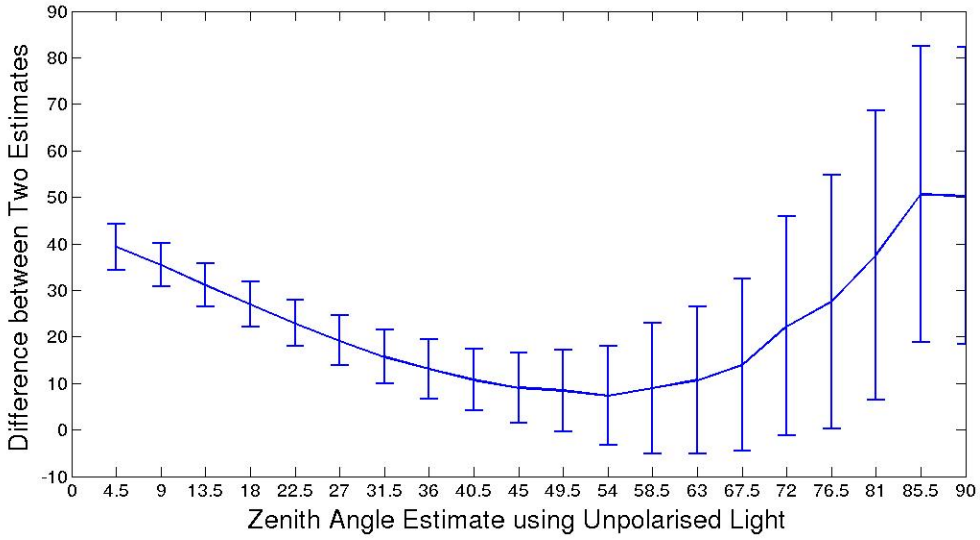

Figure 5.10: The difference distribution of two estimates shown in Figure 5.9. The X axis is the zenith angle estimate from diffuse polarisation model that ranges from 0 to 1, the Y axis represents the mean value of computed difference between the two results, with the error bar for the variance.

them in Figure 5.12 using Matlab program and a 1.2GHz CPU computer. Compared with the results shown in the last chapter, the surfaces of objects become much smoother, though it is not much improved. The simple objects, such as apples and balls, were not performed well, as shown in Figure 5.11(a) and Figure 5.11(f), where the surfaces are slightly distorted. It is also noted that without the azimuth angle information, the shapelets method cannot accurately determine whether the given surface is convex or concave. For example, in Figure 5.11(h) and Figure 5.11(c), the nose shapes of the human face and plaster owl are concave instead of convex. With the azimuth angle information to hand, such problems can be easily solved.

5.4 Conclusions

In this chapter, we show how to use the Fresnel theory in shape recovery, using the images taken under polarised light. We have investigated Malus's law, and constructed a new novel model, which is completely different from the alternatives in polarisation vision. We demonstrate experimentally that the proposed method can be applied for shape recovery

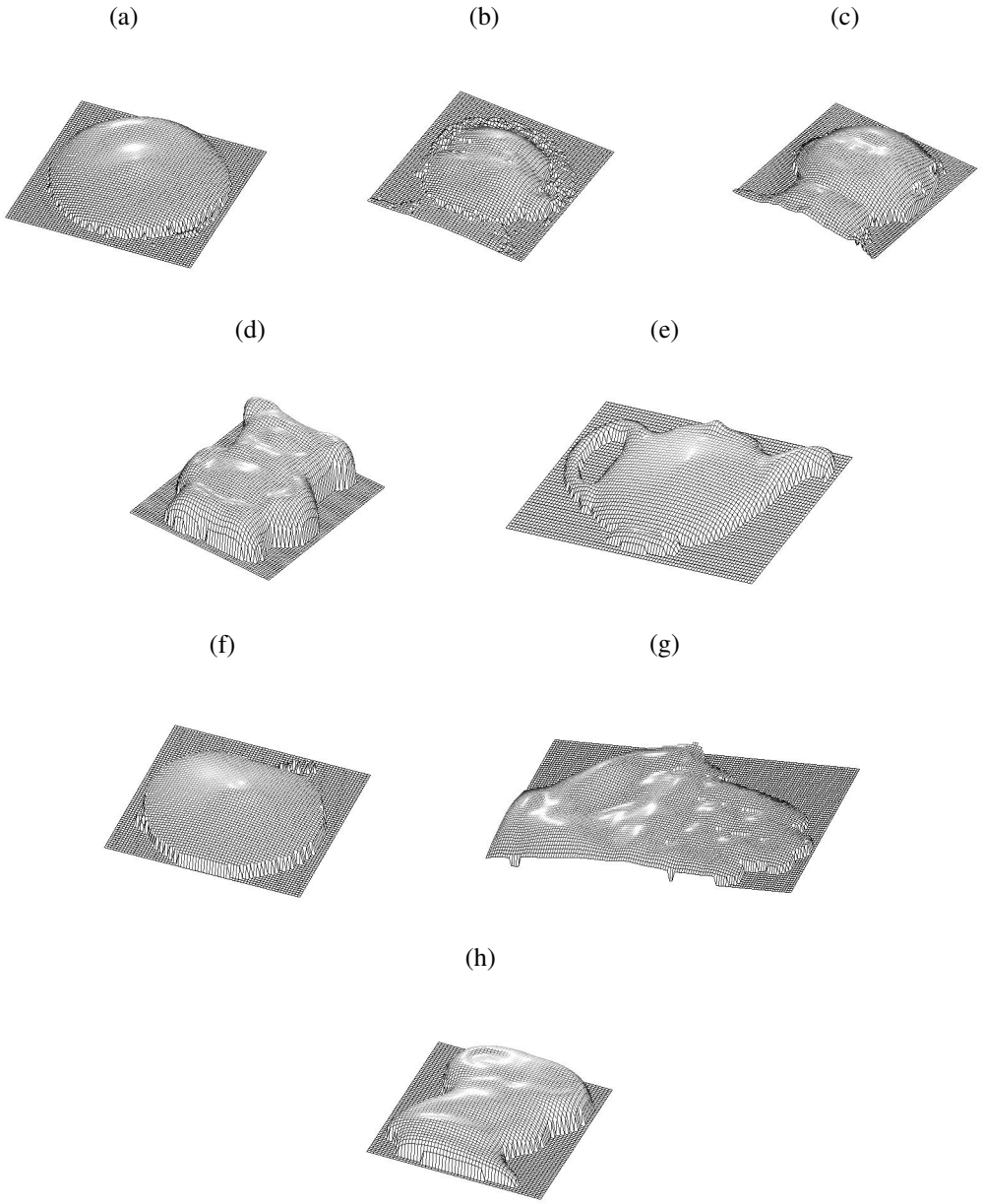

Figure 5.11: The mesh 3D model recovered from the estimated surface normal.

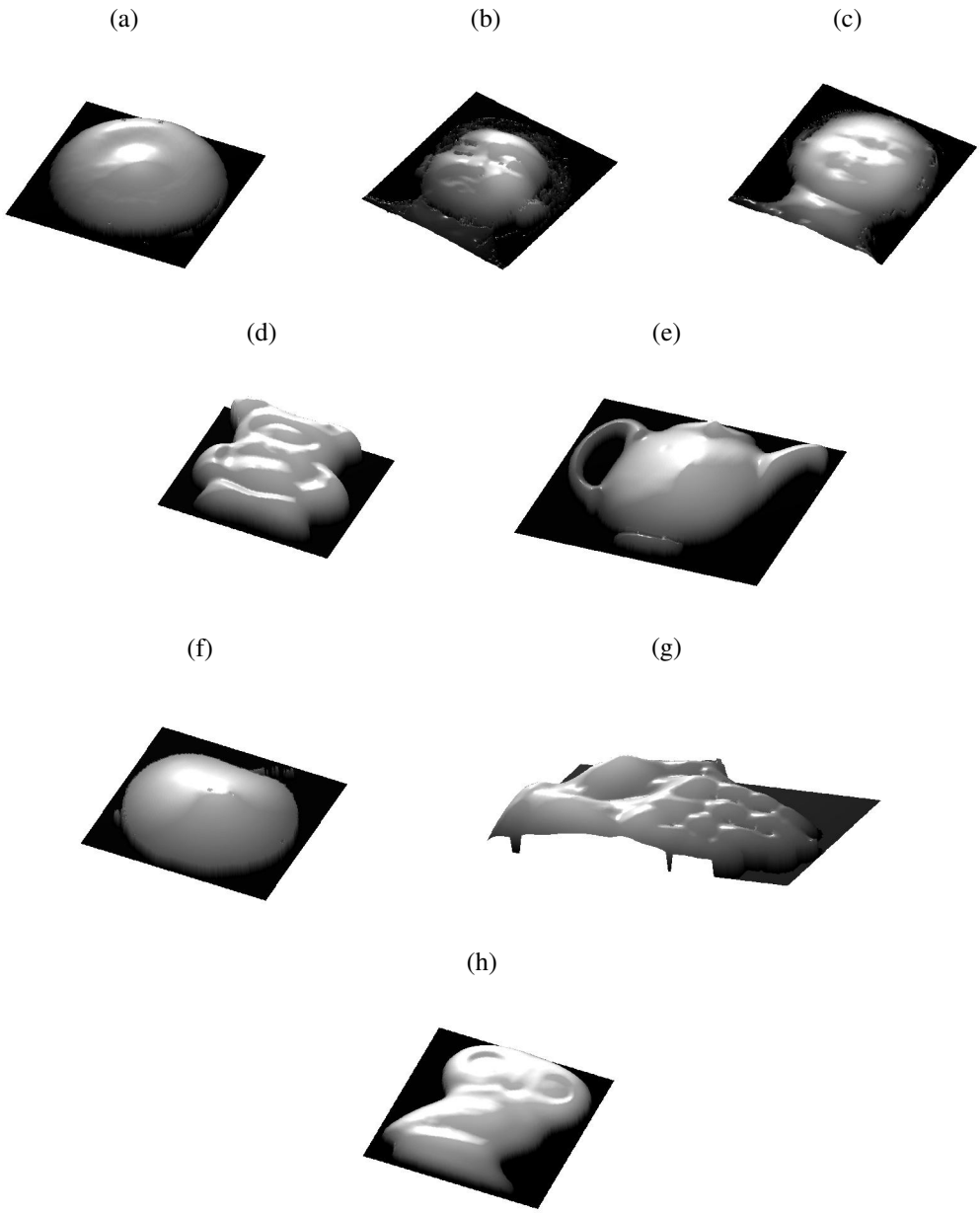

Figure 5.12: The height map recovered from the estimated surface normal.

using polarised light, and it produces results which are better than the traditional shape from diffuse polarisation method.

We also present a novel BSS method for reflectance component separation. Only three polarised images are required for computation and the phase angle estimates can also be obtained, which is impossible for the cross-polarisation approach. The separated components can also be used for reflectance estimation and shape recovery; the methodology is presented in the next chapter. Furthermore, the height map recovered is unsatisfactory because the azimuth angle information is lacking during computation. We present an algorithm in Chapter 6, where we also concentrate on solving this problem.

Chapter 6

Shape and Reflectance Recovery

In this chapter we introduce the parametric reflectance models used in our method and show how to estimate their parameter values. With the separated reflectance components estimates in Chapter 5 to hand, the zenith angle of the surface normal can be inferred from the relevant reflectance model together with its estimated parameter values. We develop a novel two-step method for reflectance parameter estimation and shape-recovery. In the first step, we determine the parameter values for the diffuse and specular reflectance models. In the second step we use a probabilistic framework to recover the shape from the estimated reflectance components. We present experiments to demonstrate the validity of the proposed method for a variety of materials, and we show that the proposed method is capable of accurately estimating both shape and reflectance information.

Contribution

Our goal in this chapter is to propose a novel framework for reflectance and shape estimation in polarisation vision. Theoretically, the zenith angle estimate can be computed directly from the reflectance component using the inverse function of the reflectance model. However, due to the limited capacity of the chosen models, the estimates obtained are usually unsatisfactory. The proposed framework recovers shape from two reflectance components. Firstly the zenith angle estimates from diffuse and specular components are compared and the parameter values of the reflectance models are adjusted to make the two estimates as close to each other as possible. We also apply the iterated conditional models algorithm introduced in Chapter 4 and Chapter 5 for recovering the correct shape

information from the two estimates. The details are presented in Section 6.2.

There are two other contributions in this chapter. Firstly, we introduce a novel approach for solving azimuth angle estimation, which is one of the main issues in the shape from polarisation field. Existing methods measure the azimuth angle using the stereo method, which requires extra devices and more images are taken during image acquisition [7] [68]. The proposed method used the SFS algorithm, which is simple and low-cost to use. We show its performance in Section 6.2.2.

Secondly, we show how to use the proposed method in other computer vision fields. There are two applications in Section 6.3.4 and Section 6.3.5, we start by relaxes assumption about constant reflectance. Next we show how to extract features from reflectance estimates, in which we have 35 fruits for seven categories under study.

Chapter Outline

The remainder of this chapter is organised as follows: Section 6.1 shows the mutual information estimation used here for reflectance measurement. In Section 6.3 we demonstrate the validity of the proposed method, and present two applications in the computer vision field.

6.1 Reflectance Estimation

In this chapter we apply those six reflectance models for reflectance measurement, in which the models of Lambertian, O-N and B-K are more suitable for estimating diffuse component in the images, whilst the Phong, T-S and C-T models are generally used for specular component estimation. We invert the reflectance function to recover shape, i.e. surface normal zenith angle, information. It is noted that the original reflectance models of Phong, T-S and C-T contain diffuse component which is actually the Lambertian model. Here we only use their specular component for the estimation. Our aim is to show if those three models can use O-N or B-K model as the diffuse part, and if such combination can improve the estimation results.

The reflectance models are also simplified according to the following two constraints. Firstly, the incident and viewing directions follow the retro-reflection constraint, in which

the two orientations are identical. Secondly, the images are acquired in the front view, therefore the azimuth angle of the incident and viewing directions are equal to zero. We show in the experiment section that the image acquisition setting follows these two constraints.

Let the specular and diffuse reflectance models as $f_s(\psi_s, \boldsymbol{E}_s)$ and $f_d(\psi_d, \boldsymbol{E}_d)$, respectively, and let $\boldsymbol{E}_s$ and $\boldsymbol{E}_d$ be their parameter value sets. The estimated surface normal zenith angles for the two models are ψ_s and ψ_d. Associated with each model is a scaling coefficient, denoted by k_s and k_d. The separate reflectance components are I_s and I_d. Hence we can write

$$I_s = k_s f_s(\psi_s, \boldsymbol{E}_s) \,, \tag{6.1}$$

$$I_d = k_d f_d(\psi_d, \boldsymbol{E}_d) \,. \tag{6.2}$$

Upon inversion the two zenith angles are

$$\psi_s = f_s^{-1}(I_s/k_s, \boldsymbol{E}_s) = f_s^{-1}(I'_s, \boldsymbol{E}_s) \,, \tag{6.3}$$

$$\psi_d = f_d^{-1}(I_d/k_d, \boldsymbol{E}_d) = f_d^{-1}(I'_d, \boldsymbol{E}_d) \,. \tag{6.4}$$

We compute k_s and k_d so that the two components $I'_s = I_s/k_s$ and $I'_d = I_d/k_d$ are normalised. Since they correspond to the same image location, the two zenith angles should correspond, i.e. ψ_s and ψ_d should be identical. As I_s and I_d are known, the parameter values can be found when the distributions of ψ_s and ψ_d are closest to each other. Because of its rapid (quadratic) convergence we use Newton's method to estimate the parameters $\boldsymbol{E}_s$ and $\boldsymbol{E}_d$. The criterion function used as input to Newton's method is defined by a mutual information criterion B for the distributions of ψ_d and ψ_s. The values of $\boldsymbol{E}_s^{(0)}$ and $\boldsymbol{E}_d^{(0)}$ are initialised according to the properties of the corresponding reflectance models. The process of mutual information estimation is given in Algorithm 6.1.

6.2 Shape Recovery

In this section we introduce the method for estimating surface normal information, which consists of zenith and azimuth angles. We commence by showing how to estimate the

Algorithm 6.1: Newton's method for recovering parameters of reflectance models, using the mutual information estimation between two zenith angle results from diffuse and specular components.

Input: The diffuse and specular components I_d and I_s, albedo coefficients k_s and k_d.

Output: The parameter values of reflectance models $\boldsymbol{E}_s$ and $\boldsymbol{E}_d$.

begin
  Set the iteration $t = 0$;
  Initialise $\boldsymbol{E}_s^{(0)}$ and $\boldsymbol{E}_d^{(0)}$;
  repeat
    Compute $\psi_s^{(t)}$ and $\psi_d^{(t)}$ using Equation 6.3 and Equation 6.4;
    Compute mutual information between $\psi_s^{(t)}$ and $\psi_d^{(t)}$, the result is $B(\psi_s^{(t)}; \psi_d^{(t)})$;
    Update $\boldsymbol{E}_s^{(t+1)}$ and $\boldsymbol{E}_d^{(t+1)}$ using the equation of Newton's method: $\Theta^{(t+1)} = \Theta^{(t)} - \eta \boldsymbol{Q}[B^{(t)}]^{-1} \nabla B^{(t)}$, where $\Theta^{(t)} = (\boldsymbol{E}_s^{(t)}, \boldsymbol{E}_d^{(t)})^T$;
    Set iteration $t = t + 1$;
  until $[B^{(t)} - B^{(t-1)}]^2 < \epsilon$;
end

zenith angle, when the parameter values of the chosen reflectance models have been obtained. As previously stated, the two estimates ψ_s and ψ_d should have identical distributions since they originate from the same surface, but via estimation methods based on different reflectance models. However, there are inevitably some differences between the two estimates due to the limited capacities of the selected reflectance models to accurately reproduce the behaviour of real-world surfaces. Concrete problems include the influence of texture and shadows. Here we use the iterated conditional method which estimates the zenith angle information from the two estimates ψ_s and ψ_d using the probabilistic model.

The azimuth angle can be computed from the phase angle estimate, which can be obtained using the proposed frameworks in the previous chapters, as we have demonstrated. However, there is an azimuth angle ambiguity problem, which needs to be solved beforehand. Some of the existing methods recover azimuth angle by making constraints on surface shape [69] [3], whilst the others use stereo methods instead [68] [5]. Both have weaknesses that render them impractical for shape recovery. In this section we solve this problem by firstly using the SFS method to obtain an azimuth angle estimate, and then comparing it with the phase angle.

6.2.1 Zenith Angle Estimation

We commence by developing an information theoretic framework for recovering the underlying surface shape as captured by the zenith angle ψ. We assume that the observed zenith angle is drawn from a probabilistic model over the diffuse and specular components. Each probabilistic component has an associated zenith angle estimate ψ_d and ψ_s. We take the posterior mean of the two estimates, that is

$$\psi = P(\omega_s|I_s, I_d, \psi_s)\psi_s + P(\omega_d|I_s, I_d, \psi_d)\psi_d \; . \tag{6.5}$$

where $P(\omega_s|I_s, I_d, \psi_s)$ and $P(\omega_s|I_s, I_d, \psi_d)$ are the *a posteriori* probabilities of the specular and diffuse components, satisfying $P(\omega_s|I_s, I_d, \psi_s) + P(\omega_d|I_s, I_d, \psi_d) = 1$, $0 \leq P(\omega_s|I_s, I_d, \psi_s) \leq 1$ and $0 \leq P(\omega_d|I_s, I_d, \psi_d) \leq 1$. ω_s and ω_d are the class identities meaning that the result estimation ψ is equal to ψ_s or ψ_d, respectively.

For every location in the image the value of ψ is intermediate between ψ_s and ψ_d, i.e. $\min(\psi_s, \psi_d) \leq \psi \leq \max(\psi_s, \psi_d)$. Applications of probabilistic models generally

are in the fields of clustering, generative component models and density estimation [62]. Here our aim is to find the mixing proportions for the two surface normal estimates and calculate their posterior mean ψ.

The idea underpinning the approach is to iteratively interleave the two processes of calculating the reflectance components recovered from the current shape estimate ψ, and update ψ based on the error between the input components with the current estimated reflectance. The main difference between the iterated conditional modes (ICM) method applied in this section and the approach introduced in Chapter 5, is that in this chapter there is no polarisation model included in the probabilistic model. Therefore the algorithm can be simplified. The iterative process of ICM is listed in Algorithm 6.2.

6.2.2 Azimuth Angle Estimation

When the reflected light is polarised, the part that becomes fully polarised has its wave oscillation directed to a single orientation. The direction is equal to the azimuth angle on the surface. Therefore when it is transmitted through a linear polariser, maximum light transmission is allowed if the polariser angle is parallel to the oscillation orientation. Denote ϕ as phase angle, in Equation 3.4 of TRS the intensity becomes maximum when the polariser angle ψ follows $\psi = \phi$ or $\psi = \phi + 180^o$. Define γ as surface azimuth, which is the angle between the direction of surface normal projected onto the image plane and the y-axis. Therefore we have two ambiguity angle candidates γ_1 and γ_2 from phase angle, which is written as follows

$$\gamma_1 = \phi \qquad \gamma_2 = \phi + 180^o \, . \tag{6.6}$$

Our goal is to recover the azimuth angle from the two candidates. We commence by estimate azimuth angle using the SFS method, which is denoted as γ' here. As described in Chapter 2, SFS methods are not robust for recovering shape from dielectric materials, but are simple and require only one input image. We utilised Worthington and Hancock [119] algorithm here for its simplicity and relatively efficient performance in shape recovery. When the estimate γ' is obtained, we measure the correct azimuth angle γ by selecting the candidate whose value is closer to γ', which is given by

Algorithm 6.2: The ICM method using diffuse and specular components for zenith angle estimation.

Input: The diffuse and specular separated reflectance components I_d and I_s, and the E_d and $_s$ computed using Algorithm 6.1, and k_s and k_d.

Output: zenith angle result ψ.

begin

  Set iteration $t = 0$;

  Initialise $P(\omega_s|I_s, I_d, \psi_s)^{(0)} = P(\omega_s|I_d, I_d, \psi_s)^{(0)} = 0.5$;

  Compute ψ_d and ψ_s using the two reflectance models, with their parameter sets E_s and E_d, and their scaling coefficients k_s and k_d;

  Compute $\psi^{(0)}$ using Equation 6.5;

  repeat

    Compute $I_s^{(t)}$ and $I_d^{(t)}$ using the chosen two reflectance model;

    Compute error functions $\varepsilon_s^{(t)} = [I_s - I_s^{(t)}]^2$ and $\varepsilon_d^{(t)} = [I_d - I_d^{(t)}]^2$ using least square fitting;

    Update the *a posteriori* class probabilities $P^{(t+1)}(\omega_s|I_s, I_d, \psi_s) = \frac{\exp[-\varepsilon_s^{(t)}]}{\exp[-\varepsilon_s^{(t)}]+\exp[-\varepsilon_d^{(t)}]}$ and $P^{(t+1)}(\omega_d|I_s, I_d, \psi_d) = \frac{\exp[-\varepsilon_d^{(t)}]}{\exp[-\varepsilon_s^{(t)}]+\exp[-\varepsilon_d^{(t)}]}$;

    Update $\psi^{(t+1)}$ using Equation 6.5;

    Compute error function $\varepsilon^{(t)} = \sum_{x,y}[\varepsilon_s^{(t)}(x, y) + \varepsilon_d^{(t)}(x, y)]$;

    Set iteration $t = t + 1$;

  until $[\varepsilon^{(t)} - \varepsilon^{(t-1)}]^2 < \epsilon$;

end

$$\gamma = \begin{cases} \gamma_1 & |\gamma_1 - \gamma'| \leq |\gamma_2 - \gamma'| \,, \\ \gamma_2 & |\gamma_1 - \gamma'| > |\gamma_2 - \gamma'| \,. \end{cases} \tag{6.7}$$

6.3 Experiments

In this section we demonstrate the validity of the proposed method for estimating reflectance and shape. All the image acquisition settings are as described in Chapter 5. We commence by testing the performances of six chosen reflectance models by using them in the estimation framework. The two best-performed reflectance models are chosen and we show their zenith angle results. The azimuth angle estimation method is also demonstrated experimentally. We also give two applications of proposed methods in computer vision: firstly we intend to construct a reflectance parameter map for the surface. Next we show how to extract features from reflectance estimates, which can further applied in object classification.

6.3.1 Zenith Angle Estimation from Six Chosen Models

Here the experiment conducted is to show the zenith angle estimates from the diffuse and specular components respectively, and the results using ICM method following Algorithm 6.2. There are 12 objects in various materials used for the experiments, including human face, palm, apple, plaster, etc. For each object we used six reflectance models for testing, which are Lambertian (L), Oren-Nayar (O-N) and Beckmann-Kirchhoff (B-K) models for diffuse component estimation, and Phong (P), Torrance-Sparrow (T-S) and Cook-Torrance (C-T) models for the specular component. We show our surface normal estimations for a human palm in Figure 6.1 and Figure 6.2 obtained from the diffuse component and from the specular component, respectively. The zenith angle results using the probabilistic model is shown in Figure 6.3.

6.3.2 Reflectance Models Comparison

There are two experiments conducted for the comparison of six reflectance models. Firstly we presents reflectance functions of diffuse and specular components based on the re-

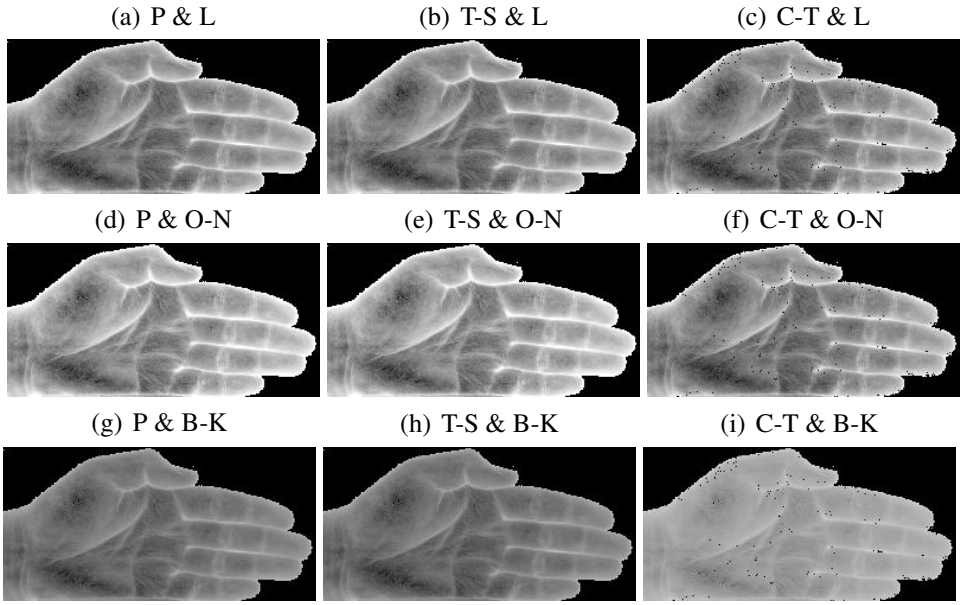

Figure 6.1: The estimated zenith angle result from the diffuse component of the palm images.

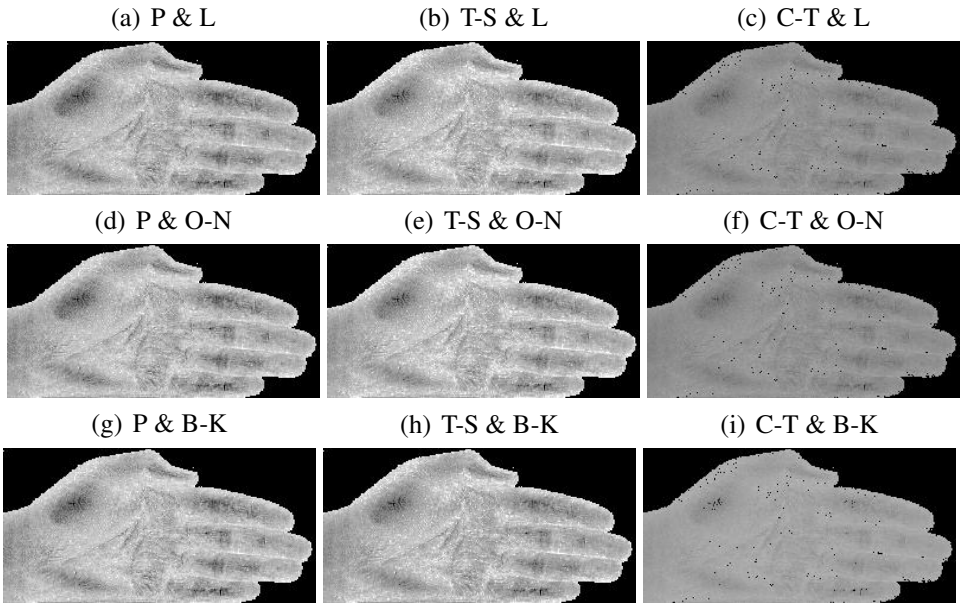

Figure 6.2: The estimated zenith angle result for the specular component of the palm images.

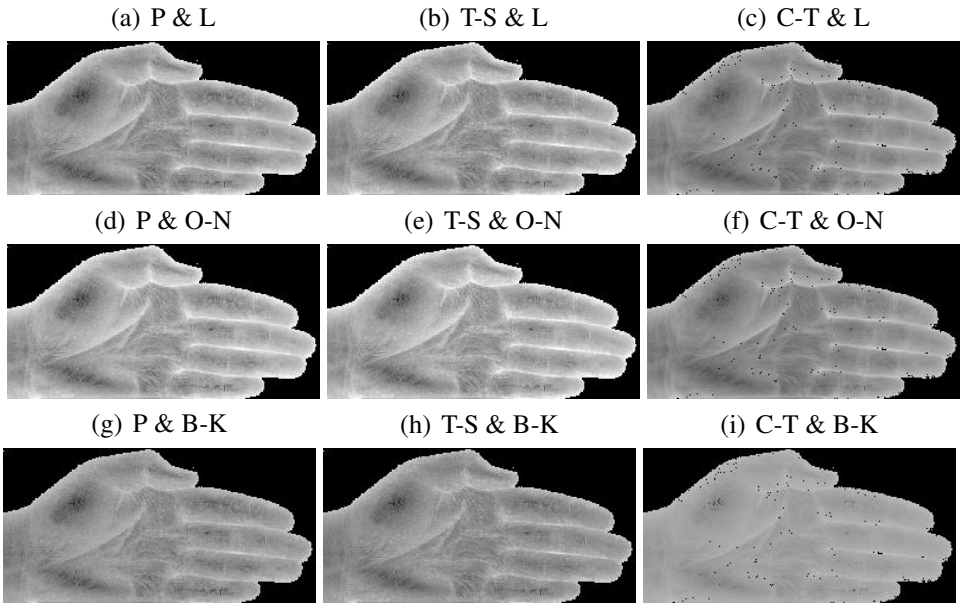

Figure 6.3: The zenith angle estimation results of the palm using ICM method.

flectance model parameters and zenith angle estimates in Figure 6.3, and compare them with the other reflectance functions based on two input components I_d and I_s and the zenith angle results.

Figure 6.4 shows the comparisons for diffuse components, and Figure 6.5 for specular components. The red curves in the figures represent the estimated component intensities with the zenith angle, while the blue curves show the input component intensities. The two chosen reflectance models perform the best when the two curves are closest to each other. We found that for the palm object, using P and O-N model will give the best zenith angle estimation.

In the second experiment we compute the average degree differences between each ψ_d and ψ_s for every combination of the chosen models from 12 objects under study. Table 6.1 shows the comparison results, with the three lowest values in each row marked. In the last row, the number of values which are marked for every column are counted and displayed; this is where we found the two reflectance models C-T & B-K which exhibited the most robust performance for all the test objects. We show all the estimation results using these two reflectance models in Figure 6.6.

The third experiment in this section is to compare the zenith angle results from Chapter 3 to Chapter 6 with the ground truth data. Their profiles are shown in Figure 6.8, the red line represents the zenith angle of the ground truth in Figure 6.7, the black line is for the

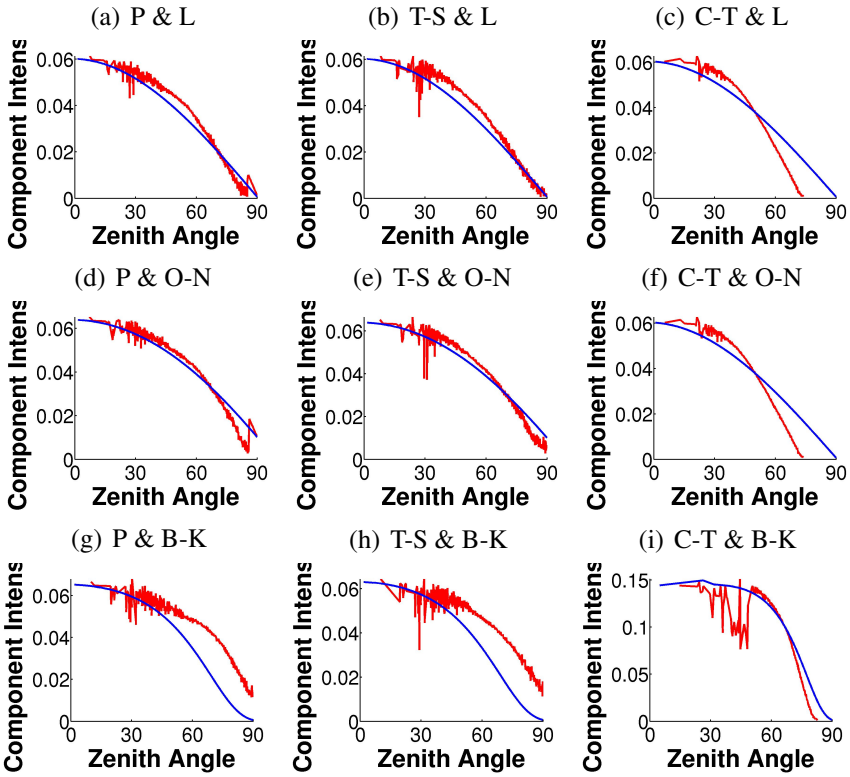

Figure 6.4: The reflectance functions showing estimated (red) and input (blue) diffuse intensities vs. incidence angle (degrees) for the 9 combinations of 6 models.

Object	P & L	T-S & L	C-T & L	P & O-N	T-S & O-N	C-T & O-N	P & B-K	T-S & B-K	C-T & B-K
(a)	10.0933	11.6628	**8.3871**	14.7469	11.9407	**8.3784**	12.7077	11.0268	**2.7073**
(b)	**5.5659**	8.1981	8.1834	6.1119	10.1287	8.1781	16.0189	**6.0387**	**2.7969**
(c)	11.7387	11.7114	**8.6117**	16.1290	14.2806	8.7929	9.0234	**4.7555**	**3.1386**
(d)	11.2333	10.4713	12.8066	11.7740	12.0234	10.4854	**3.9226**	**5.0487**	**4.2480**
(e)	11.5318	13.8986	**11.3075**	11.6007	12.5497	**11.3162**	14.7635	20.7186	**3.4637**
(f)	11.8937	14.1800	13.8163	12.5334	18.1971	13.8165	**10.8185**	**9.7094**	**5.2193**
(g)	14.2579	14.3202	15.8556	14.0307	**13.9955**	16.1079	17.7225	**11.0234**	**6.9204**
(h)	16.4035	15.4444	15.0133	**13.0860**	15.8120	**12.8245**	15.6969	19.8582	**5.7076**
(i)	7.3221	**6.5468**	11.0542	6.9148	6.6644	11.0160	10.9366	**4.9092**	**4.3284**
(j)	15.7758	9.7315	10.0429	**5.5467**	**9.4252**	10.1020	12.1209	17.3663	**3.2221**
(k)	13.4805	14.6278	**9.8023**	11.2663	11.4619	**9.8050**	21.8432	21.5365	**3.9133**
(l)	10.2859	10.3647	10.6280	5.5744	5.6535	11.5517	**4.7663**	**4.3278**	**3.9820**
Count of Best	1	1	4	2	2	4	3	7	12

Table 6.1: The average degree differences between surface normal estimations from diffuse and specular components, each row represents the corresponding object shown in Fig.6.6. The three lowest values for each row are marked, and the last row shows the number of values in every column that are marked.

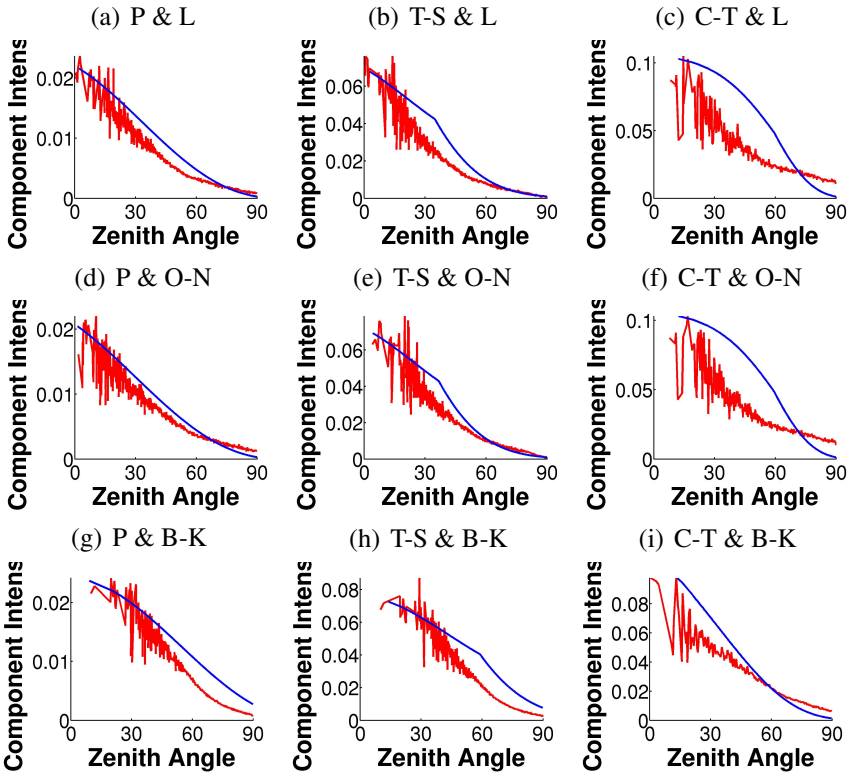

Figure 6.5: The reflectance functions showing estimated (red) and input (blue) specular intensities vs. incidence angle (degrees) for the 9 combinations of 6 models.

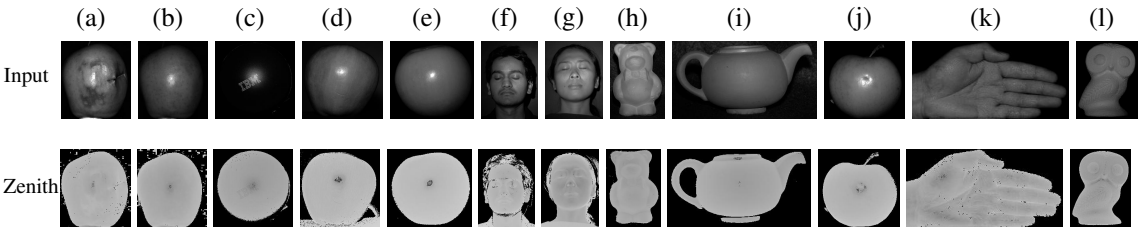

Figure 6.6: The shape results for 12 objects. The first row contains the unpolarised images and the figures in the second row show the surface normal estimations.

Figure 6.7: The zenith angle information of the ground truth data of porcelain bottle.

method using BSS, the pink line is the result using the polarisation probabilistic model in Chapter 4, the blue line is the estimate using BSS and improved criterion function which is close with the black line, the cyan line is for the method of novel polarisation model in Chapter 5, and the green line is for the method of reflectance model. The first two are computed using unpolarised light, while as the rest two use polarised light. It is shown that the lines of estimates are generally following the ground truth, although the accuracy is less pronounced than what are expected for general objects. The work of Atkinson [6] is focused on optimising the polarisation estimates, combining the techniques with the proposed frameworks will greatly improve the results of estimation, which will be one of our research goals. It is also noted that noises of estimates in Figure 6.8 can be eliminated using smoothing approaches.

6.3.3 Surface Azimuth Recovery

In this section we present experiment for azimuth angle estimation following Section 6.2.2. We have provided three objects for the estimation: a china vase and two apples. Figure 6.9 shows the results: the first row presents the images for the experimental objects, the second row shows their phase angle estimates and the third row contains the azimuth angle results. The methods perform well for the simple objects, while for the china vase

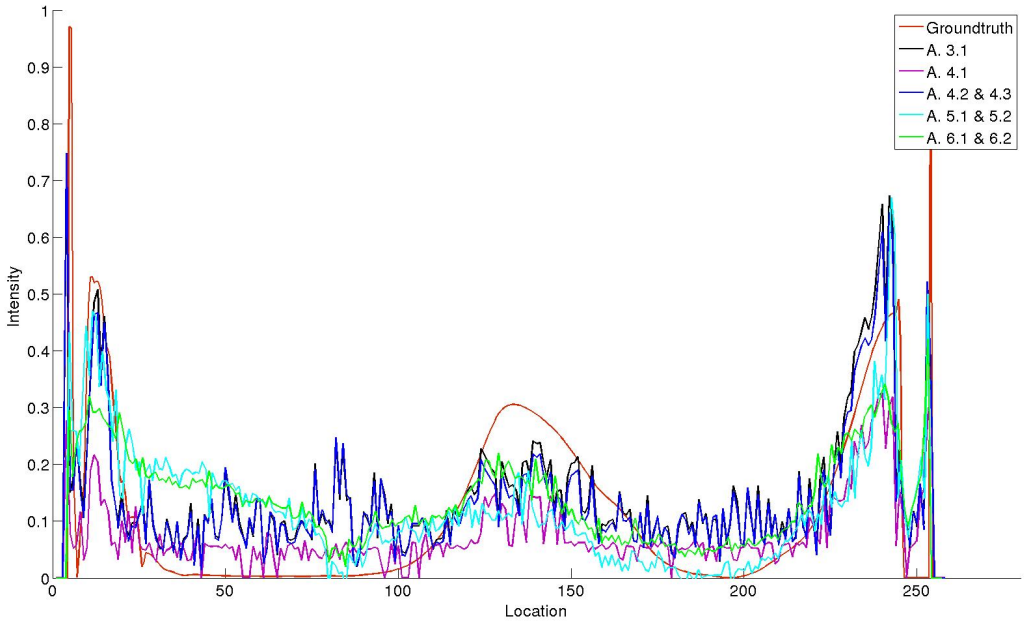

Figure 6.8: The zenith angle profiles of the porcelain bottle, the red line represents the ground truth data, and the rest are estimates using methods proposed in this thesis. Black line is the result using Algorithm 3.1, pink line is Algorithm 4.1, blue line is Algorithm 4.2 and Algorithm 4.3, cyan line is Algorithm 5.1 and Algorithm 5.2, green line is Algorithm 6.1 and Algorithm 6.2.

the estimate for the neck part is incorrect. The proposed method is not robust enough to be applied to general objects of dielectric materials, especially when the surface shape is complicated. Figure 6.10 shows the images for which the azimuth angle is not correctly recovered. The reason for this is that the SFS method proposed by Worthington and Hancock, produces fairly poor azimuth angle results which influences the final estimation, as shown in (c). Therefore a better SFS method should be found or developed in future research.

6.3.4 Reflectance Parameter Map

Experiment in this section is to make constraint that the surface of the objects under study does not have the uniform reflectance properties, and demonstrate the approach to recover parameter value map based on the zenith angle estimates, which can be used for material analysis and many other applications in computer vision. With the zenith angle estimate ψ to hand, and assuming that all albedo information on the surface is constant, the parameter values can be computed using the reflectance models. We use the two models described in Section 6.3, which are the O-N and the Phong model, because of their simplicity. We have computed the parameter maps using other models such as T-S model, B-K model and C-K model. However, their results are incorrect as the complexity of the models influence the computations.

Figure 6.11 shows the estimation results. We have used five experimental objects with no complicated textures: a potato, a red apple, an orange, a green apple and a satsuma. The results are sensible and the mean values of reflectance parameter maps are close to the parameter estimates measured by the proposed method in Section 6.1 and Section 6.2. However, the variances of the parameter values in the maps are larger than expected, we attribute this to the limited capacity of chosen reflectance models and influences from texture information. Future research will focus on developing reflectance models to solve these problems.

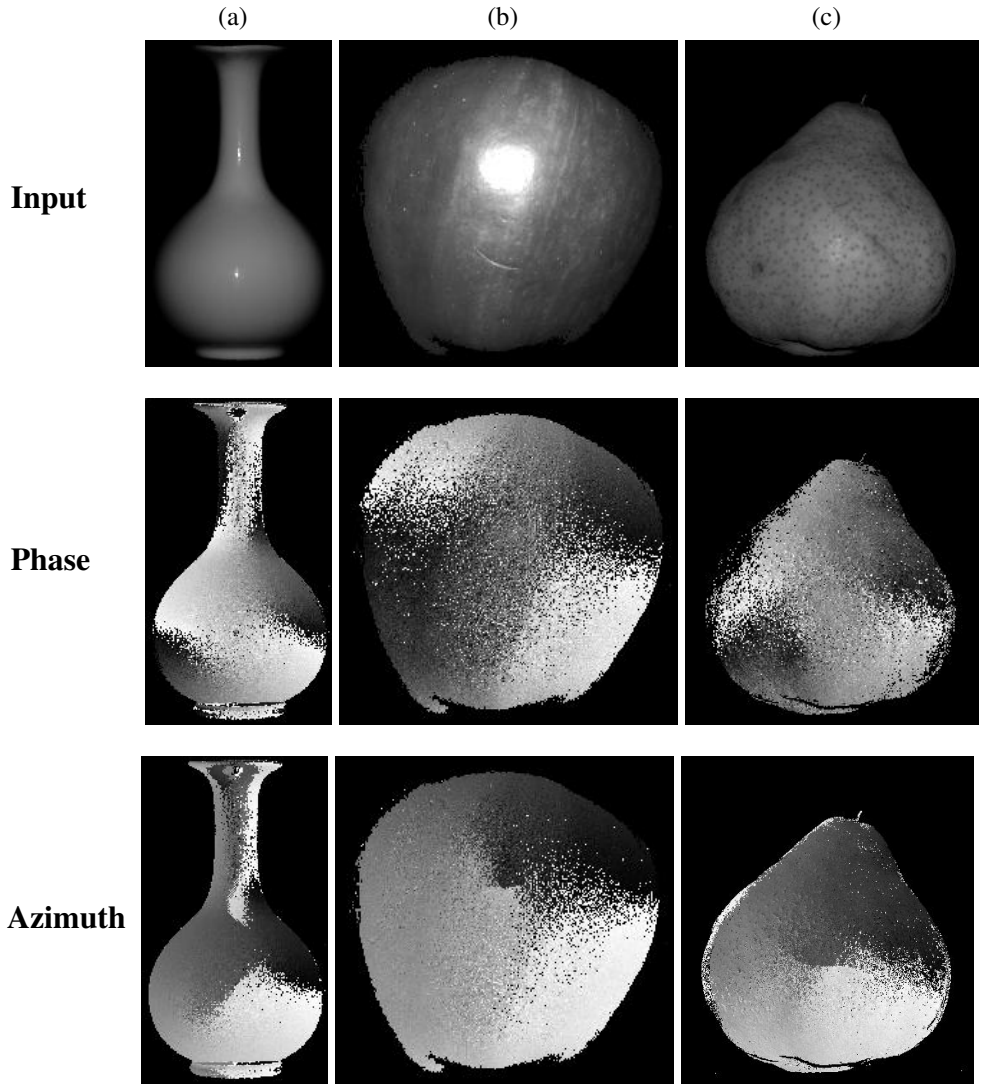

Figure 6.9: The azimuth angle results for three object. The first row are the image inputs, the figures in the second row show the phase angle results, and the third row show the azimuth angle estimates.

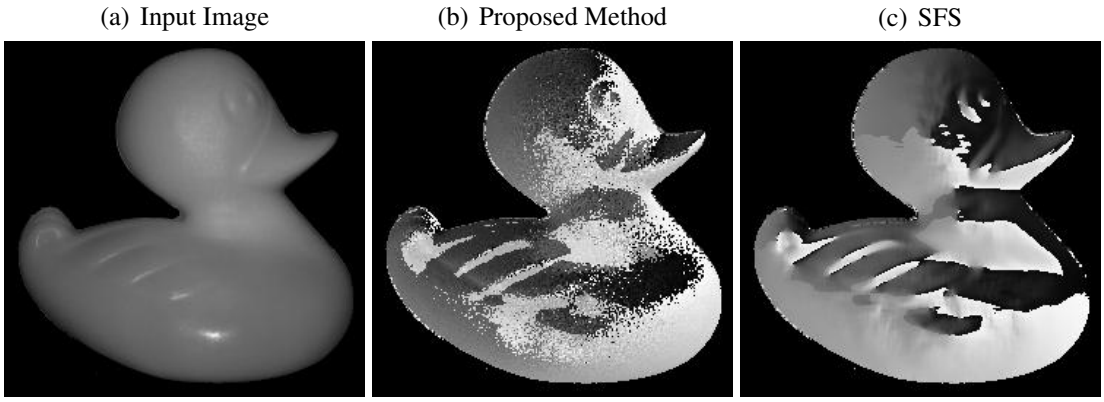

Figure 6.10: The failed azimuth angle result. The body of the duck, which should be convex, is shown as concave in the figure. Notice that estimate from SFS is so poor that it influences the performance of proposed method .

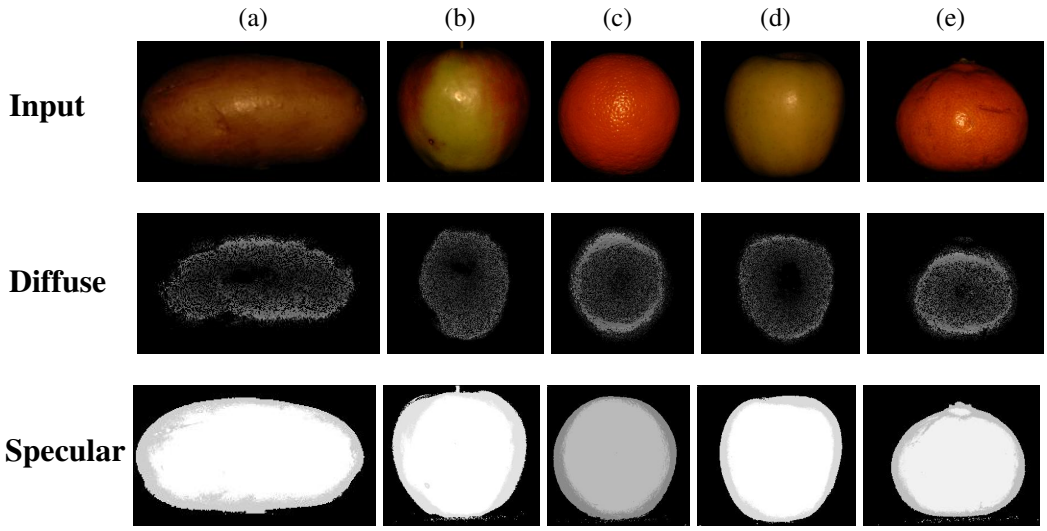

Figure 6.11: The reflectance parameter map results. The first row shows the input images, and the second and the third rows present the diffuse and specular reflectance parameter maps, respectively. The brightnesses of the figures have been adjusted to be shown clearly. Negative values in the paramter maps are considered as 0 in the figures.

6.3.5 Reflectance Feature Extraction

In this section the experiment conducted is to extract features from reflectance functions of objects under study. Feature extraction transforms the input data into a set of features which are applied to other works. It can be applied in a variety of fields in computer vision and pattern recognition domains including object recognition and classification. There are several methods available for feature extraction, such as PCA, ICA, locally linear embedding (LLE) [39] and curvilinear component analysis [20].

In this section we apply three statistical methods to the data for feature extraction. These are the traditional method of PCA, and the improved approaches which includes weight map, that are weighted PCA (WPCA) and supervised weighted PCA (SWPCA). The weight map indicates the importance of different locations in discriminating objects, thus the accuracy of results produced by feature extraction methods can be improved. The methods were developed based on the work of Wu *et al.* [120]. The methodology details can be found in our work of [125].

The reflectance functions for each experimental objects are created by using the method described in [99]. For every pixel in the image, its intensity has the corresponding value of the surface radiance function given by

$$g(\psi(x,y)) = I(x,y)\ . \tag{6.8}$$

By tabulating these two values against each other, we have a dense but noisy sampling of the function g. Then we bin the values of $g(\psi(x,y))$ into bins whose width is τ. Let $\Gamma_i = (x,y)|(i-1)\tau \leq \psi(x,y) < i\tau$ be the set of pixels (x,y) for which $\psi(x,y)$ falls into the ith bin. For ith bin we find the median value of g denoted by $h(i)$, using the equation written as

$$h(i) = \underset{(x,y)\in\Gamma_i}{\text{median}}\ I(x,y)\ . \tag{6.9}$$

The reflectance function is thus stored as a long vector $(h(1),...,h(\eta))$, which is used for feature extraction. There are 35 fruits in seven different categories for the experiments, and there are five objects in each class. The experimental objects include red and green apples, oranges, pears, tomatoes, lemons and apricots, we show the input images of all

objects in Figure 6.12, which are taken when the polarisation orientation is 0 degree. The results of reflectance functions for all inputs are shown in Figure 6.13 and Figure 6.14. The reflectance information of fruits in different classes is hard to distinguish, as it is easily influenced by dirt such as dust and oil.

In Figure 6.15 we show the feature extraction results using the three methods, i.e. PCA, WPCA and SWPCA. Observed from the figures, the feature extraction is not satisfactory, which we attribute to the measured reflectance functions. It is noted that if other information of the objects is to hand, such as colour and shape, the feature extraction results will be much improved. Besides, using techniques such as nearest neighbour or SVM, the feature extraction results considering reflectance, colour and shape can be used for object classification. This is one of the topics for future research.

6.4 Conclusions

In this chapter we proposed a shape and reflectance estimation framework based on the separated reflectance components. Using the parametric reflectance models, the zenith angle estimates can be obtained if the parameter values of the corresponding reflectance models are known. We used Newton's method and mutual information estimation to compute the parameters, which are regarded as the reflectance properties for measurement. We also apply the ICM method to compute the zenith angle information from the two shape estimates from diffuse and specular components, and we demonstrated in experimental section that the results are sensible and the proposed framework is robust for estimation of dielectric materials.

We also presented two applications using the estimates from the proposed framework. Firstly we constructed the reflectance parameter map, which shows the distribution of parameter values of reflectance models for all pixels in the image. Next we presented how to extract features from the reflectance functions, in which we applied the methods of PCA, WPCA and SWPCA. Both applications demonstrate that the proposed estimation framework can be widely applied in computer vision, though some problems still remain in the applications. More details are discussed in Chapter 7.

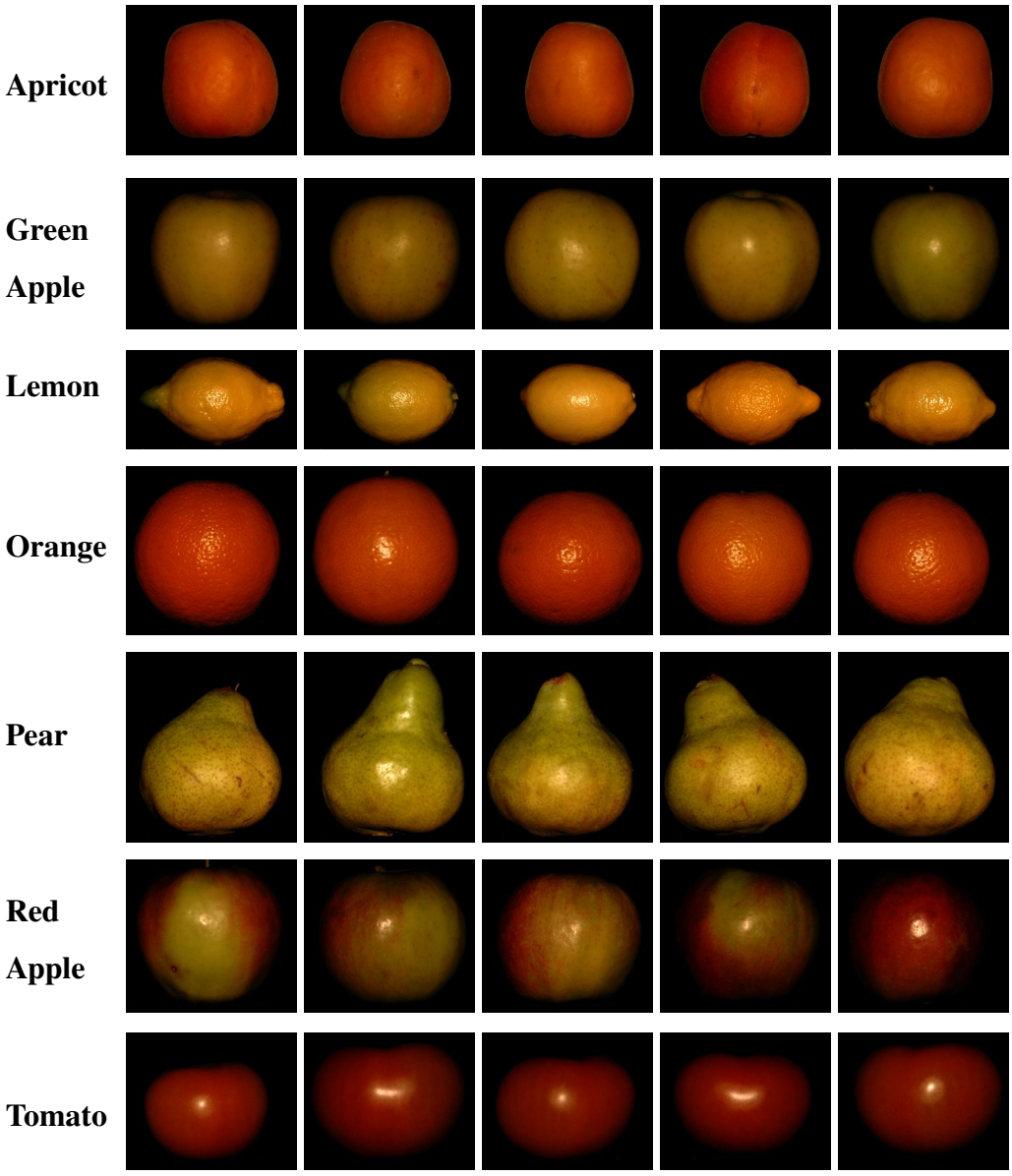

Figure 6.12: The input image of polariser angle 0 degree for 35 fruit objects.

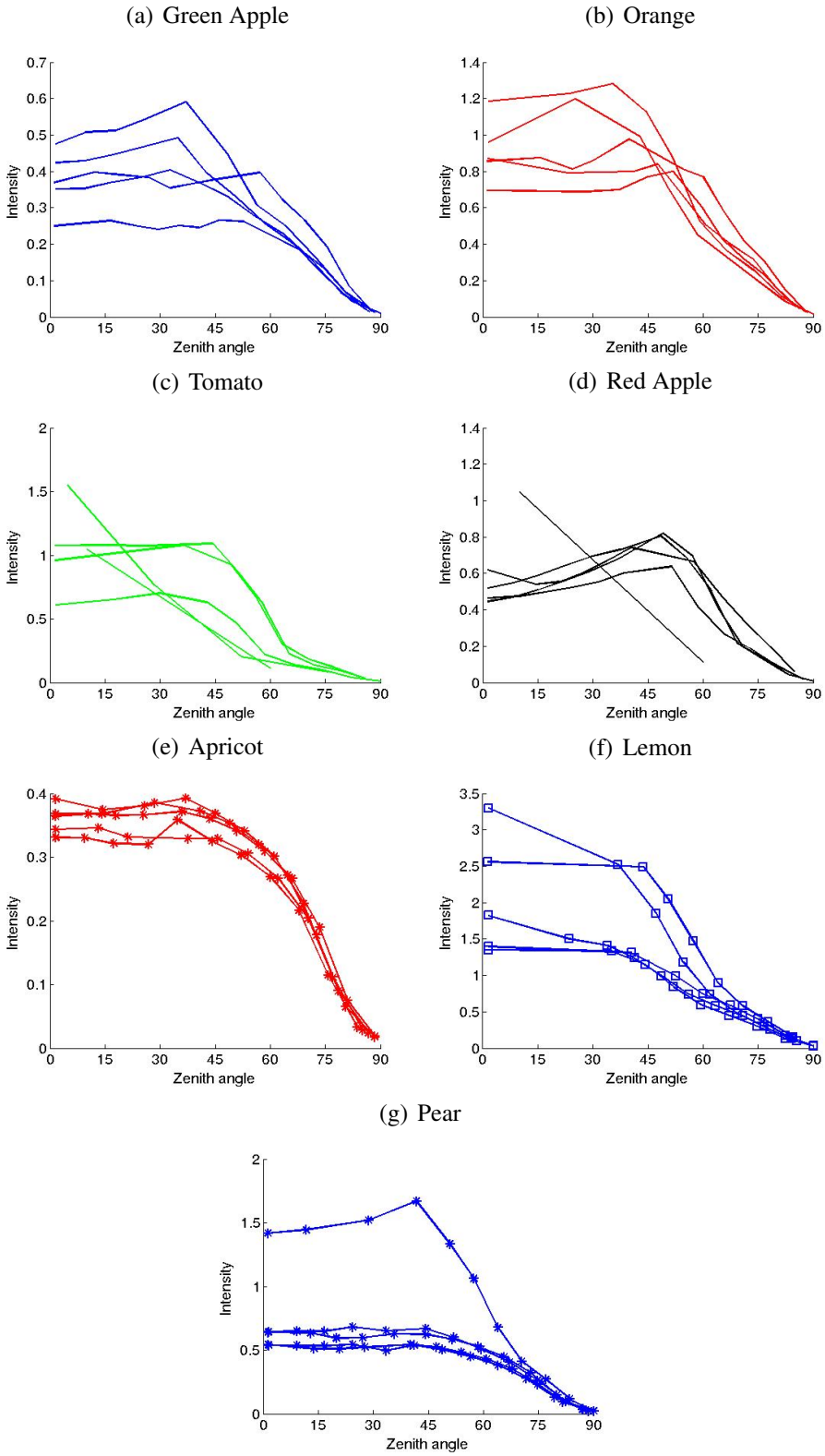

Figure 6.13: The estimated reflectance functions for 35 fruit objects. Figures from (a) to (g) shows the five objects in each class of fruit.

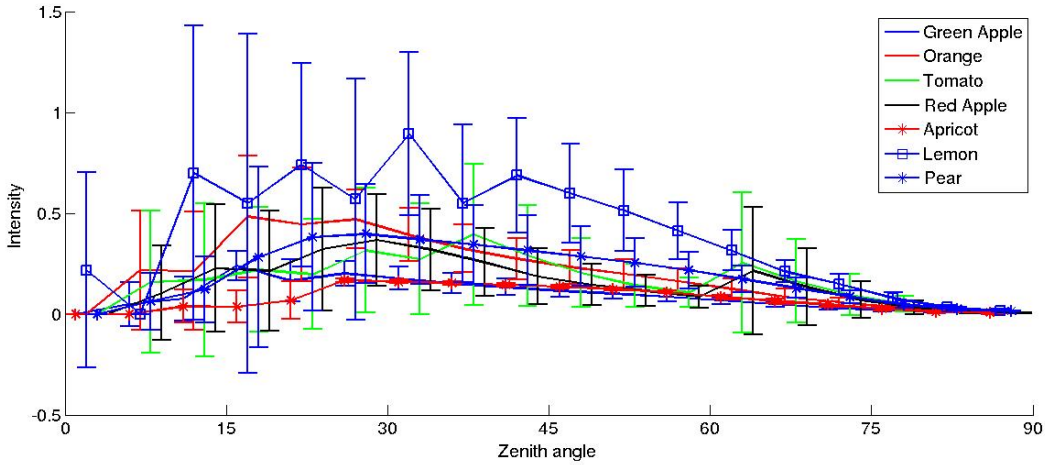

Figure 6.14: The estimated reflectance functions for 35 fruit object, which shows the mean values of seven classes, with the error bar representing the value of standard deviation.

(a) PCA of Ref.

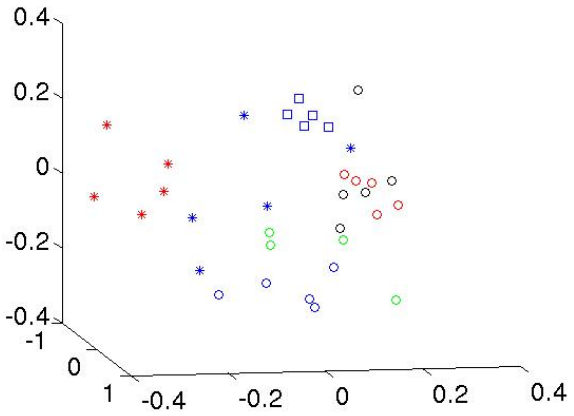

(b) WPCA of Ref.

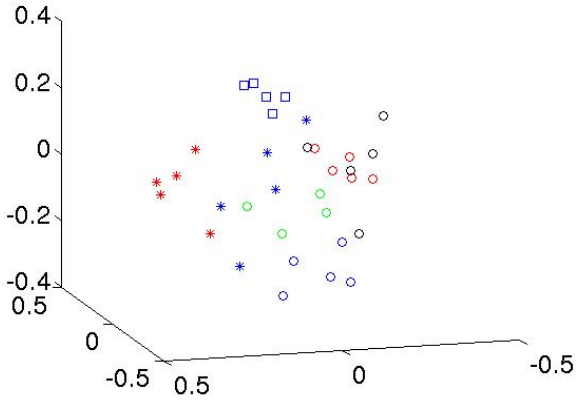

(c) SWPCA of Ref.

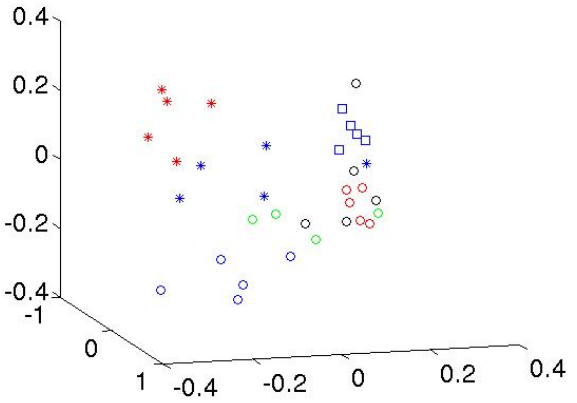

Figure 6.15: The three feature extraction methods used for three characters of fruit surface appearance.

Chapter 7

Conclusion and Outlook

In this chapter we summarised the contributions from Chapter 3 to Chapter 6, and presented the strengths of the proposed methods. The weaknesses and problems described in this thesis are also discussed. Following the analysis we introduce the future work, some focusing on how to solve the problems in the proposed methods, others investigating the applications related to our work.

7.1 Summary of Contributions

This thesis presents research on shape and reflectance estimation using polarisation, and provides advanced techniques and models which are constructed based on the Fresnel theory and statistical methods. Generally there are two different illumination conditions when using polarisation on surface characteristic estimation: Polarised and un-polarised light source. When the incident light is unpolarised, the reflected light captured by the camera is partially polarised, therefore the traditional Fresnel models can be applied for shape recovery. However, when the polarised light is reflected, part of it becomes fully polarised and there is currently no suitable Fresnel models available to be used in this circumstance. In this thesis we consider both cases, in Chapter 3 and Chapter 4 we discuss the methods using unpolarised light, while in Chapter 5 and Chapter 6 the proposed approaches can be applied for images taken under polarised light. The flow diagram in Figure 7.1 shows the thesis' structure.

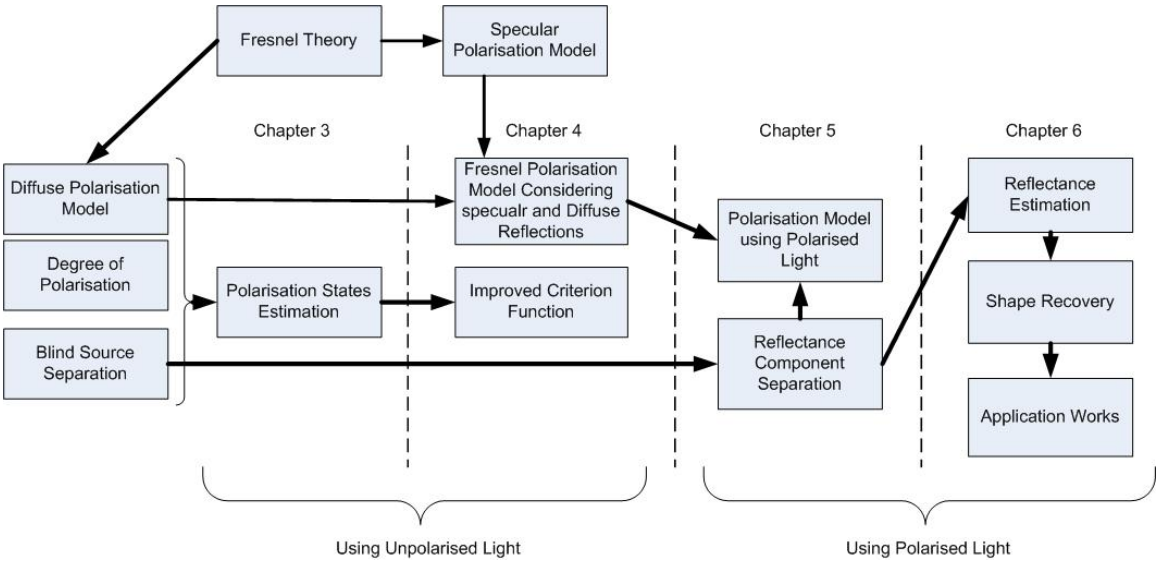

Figure 7.1: Flow diagram summarising the methods presented in the thesis.

Another main contribution of this thesis is that, we employ several statistical methods which greatly improve the performance of estimation methods in a number of ways. According to the TRS equation, there are three parameters for the polarisation states. Therefore, theoretically three input images in different polariser orientations are sufficient for measuring polarisation information. However, more images are required as the noise encountered by image qualities influence the accuracy of estimation. We utilise the BSS method which requires only three images without information on their polariser orientations in Chapter 3 and Chapter 4. In Chapter 5 the BSS method is also applied to reflectance component separation, therefore the phase angle can also be obtained, which the traditional cross-polarisation technique fails to do.

Traditional polarisation methods estimate shape by using polarisation models constructed based on Fresnel theory. There are two weaknesses: firstly both diffuse and specular Fresnel models are not perfect for shape recover, secondly there is no model available for the illumination condition of polarised light. We also develop novel polarisation models for shape recovery based on Fresnel theory. There are two new models presented in the thesis, one is applied using unpolarised light described in Chapter 4, the other is for images taken under polarised light in Chapter 5. We demonstrate their performances in the experimental sections, and show that both models can produce sensible results.

The technique of SFS is adopted in the polarisation methods to improve its performance. The SFS method is not robust enough for shape recovery from dielectric materials, since the results produced lacks accuracy. However, as it only requires one input image and can be implemented in a simple way, we use its estimates as a reference in Chapter 4 and Chapter 6. In Chapter 4 the results from the SFS method are utilised in the criterion function of the Newton's method, in order to stabilise the phase angle estimates from randomly chosen polarised images. In Chapter 6 we apply it to solve the azimuth angle ambiguity problem. Experiments show that incorporating SFS into the polarisation method can improve its performance.

In this thesis we also present a method to estimate shape and reflectance using separated reflectance components. Miyazaki *et al.* [69] also presented a similar work, but it is only applied using unpolarised light, and requires a number of input images. In Chapter 6 we use Newton's method and mutual information estimation to measure reflectance properties from the components using parametric reflectance models. Then we apply ICM method to recover zenith angle information from the diffuse and specular shape estimates. We also present two application works using the proposed estimation frameworks, firstly we investigate the variation of reflectance parameter values for different locations in the image. Next we show how to estimate reflectance functions using the information of zenith angle and image intensity, and provide three statistical methods that can extract features from a set of reflectance functions. It can be further applied in object classification and recognition.

7.2 Weaknesses of the Thesis

There are a number of weaknesses and problems in the proposed methods, that have not yet been solved, which are summarised as follows:

- We expect that by using the BSS method in Chapter 3, not only can the polarisation information be recovered, but the polariser orientations of the input images should also be measured. However, the estimation results are unsatisfactory and unreliable, especially when the polariser angles are close to each other. We attribute this to the noise in the images that affects the computation. The polariser angle estimation

does not improve much in Chapter 4 using the improved criterion function.

- The refractive index estimation in Chapter 3 and Chapter 4 is incorrect when the surface is rough. The reason is that the Fresnel model used for the measurement does not consider the surface property of roughness. Values of DOP become lower than its correct value and so is the estimated refractive index. Besides, texture information on the surface also influences the estimation, therefore it would better be eliminated beforehand.

- All the images are taken following the retro-reflection settings, in which the viewing and source light directions are identical. This restricted acquisition condition limits the methods to be applied in the computer vision field. Actually this requirement is even difficult to meet in the laboratory, as shown in Figure 3.2 and Figure 5.2. We also ignore the inter-reflection and self-shadowing in the images, which are important factors to consider in shape and reflectance recovery.

- The proposed method for estimating azimuth angle in Chapter 6 remains unreliable for estimating dielectric materials, which is the reason we decide to use shapelets method instead to recover depth map in Chapter 4 and Chapter 5. One possible improvement is to use alternative SFS method, which is better performed than the approach of Worthington and Hancock.

- There are some problems in the two applications presented in Chapter 6. Firstly the distribution of the parameter map shown in Figure 6.11 is incorrect in some areas, which is caused by the chosen reflectance models which cannot perfectly describe the reflections. Secondly, it is difficult to distinguish the recovered reflectance functions in Figure 6.13, and the feature extraction results in Figure 6.15 are also not satisfactory. We attribute this to the fact that unlike the properties of shape and texture for the objects, the reflectance information can be easily influenced by oil, dust and water.

7.3 Outlook

In this section we outline our future research, which intends to solve the problems discussed in the previous section. Some applications relevant to the works in shape and reflectance estimation will also be implemented.

A major goal for our future work is to solve the problem of azimuth angle estimation, and recover the depth map using a more reliable approach. An alternative way is to use the photometric stereo method, which can recover accurate azimuth angle information. However, it requires more images for computation, and more devices are needed during image acquisition. Besides, it becomes meaningless if the shape can be recovered by photometric stereo itself. We intend to concentrate on finding a SFS method that is reliable enough to be applied, or develop an algorithm if needed.

In Chapter 6 we make constraint that during image acquisition step the source and view angle are the same, and use it to simplify the equations of reflectance models. However, the two angles cannot be equal or the light from the source will be blocked by the camera. In our future work we focus on solving this problem, therefore the accuracy of estimation results can be improved.

With the shape and reflectance estimates to hand, these can be further exploited in the application of object classification and recognition. We show in Chapter 6 how to extract features from the estimated reflectance information. In our future work we focus on applying classification methods, such as nearest neighbour, SVM and so on. In addition to reflectance estimation , the shape and texture map in object classification is also considered. Our work in [125] shows how to measure the shape and texture information from the objects and extract features from the estimates.

The proposed methods exploit BSS to speed up the time of image acquisition, which can be applied for objects that are not static, such as human faces and palms. We have shown some results using the proposed methods. In our future work we focus on how to measure the subsurface scattering component, following the work proposed by Weyrich *et al.* [114]. Besides, the influences of cosmetics on the reflectance of human faces will also be studied. Also other statistical methods can be considered in shape and reflectance estimation using polarisation in the future, such as Markov chain Monte Carlo (MCMC), particle filtering and etc.

List of Symbols

$\overrightarrow{L}, \overrightarrow{N}_s, \overrightarrow{V}, \overrightarrow{H}$	direction of light source, surface normal, viewer and bisector of angle between $\overrightarrow{L}$ and $\overrightarrow{V}$ in Equation 2.5
$I(x, y)$	the image intensity at the point (x, y)
$I_{\max}, I_{\min}$	maximum and minimum intensity
$\bar{I}, Z$	$\bar{I} = (I_{\max} + I_{\min})/2$ and $Z = \cos\psi$ in Section 3.3.1
$J_{\max}, J_{\min}$	maximum and minimum intensity in long vector form
N_x, N_y	width and height length of the input image
$\boldsymbol{X}$	observation matrix
$\boldsymbol{U}, \boldsymbol{D}, \boldsymbol{V}, \boldsymbol{S'}$	results after SVD process of $\boldsymbol{X}$, $\boldsymbol{S'} = \boldsymbol{U}\boldsymbol{D}$ in Section 3.1.2
$\boldsymbol{C}, \boldsymbol{A}$	results after BSS process of $\boldsymbol{X}$
$\mu, \boldsymbol{S}$	scaling coefficient in method of BSS, $\boldsymbol{S} = \mu\boldsymbol{S'}$
$\boldsymbol{W}$	weighting matrix in method of BSS
ρ	degree of polarisation
θ	polariser angle
ψ	zenith angle
ϕ	phase angle
γ	azimuth angle
n	refractive index
H	Shannon entropy for the probability density function
δ, ζ	two normalised histograms in Section 3.3.2
λ	bin number of histogram
B	mutual information estimation
t	step number of the iteration
$\Theta, \eta, \boldsymbol{Q}$	parameters of update equation in Newton's method of Equation 3.32

p_s	probability coefficient in Shannon entropy of Equation 3.25
Υ_i, Υ_r	incident and reflected wave amplitude in Equation 4.1 and Equation 4.2
r	amplitude coefficient in Fresnel equations
R, T	reflection and transmission Fresnel coefficient
p	probability distribution in ICM method
P	*a posteriori* probability coefficient in ICM method
ω	class identity in ICM method
M	magnitude in the Fresnel equations
L	radiance
I_{sc}, I_{sv}	two components in specular reflectance in Section 5.2.1 following [71]
G	image region in Section 5.2.1
$k(x, y)$	the albedo value at the point (x, y) in Section 6.1
O	facet slope function for T-S and C-T model
e	parameter in the six reflectance models in Section 6.1
$f(\psi, \boldsymbol{E})$	reflectance model using zenith angle ψ and parameter set $\boldsymbol{E}$
ϵ	a constant used to determine when convergence is reached
g, τ, Γ, h	parameters of surface radiance function in Section 6.3.5
κ	bisector of angle between viewing direction and incident light direction in Figure 3.2 and Figure 5.2

Subscripts

i	Incidence
t	Transmittance
r	Reflectance
d	Diffuse
s	Specular
$\perp$	Perpendicular
$\parallel$	Parallel

References

[1] J. Aczél and Z. Daróczy. *On measures of information and their characterizations*, volume 115. Academic Press, 1975.

[2] G.A Atkinson. *Surface Shape and Reflectance Analysis using Polarisation*. PhD thesis, University of York, 2007.

[3] G.A. Atkinson and E.R. Hancock. Recovery of surface orientation from diffuse polarization. *IEEE Transactions on Image Processing*, 15(6):1653–1664, 2006.

[4] G.A. Atkinson and E.R. Hancock. Robust estimation of reflectance functions from polarization. In *Proceedings of IbPRIA*, volume 4478 of *Lecture Notes in Computer Science*, pages 363–371, 2007.

[5] G.A. Atkinson and E.R. Hancock. Shape estimation using polarization and shading from two views. *IEEE Transactions on Pattern Analysis and Machine Intelligence*, 29(11):2001–2017, 2007.

[6] G.A. Atkinson and E.R. Hancock. Surface reconstruction using polarization and photometric stereo. In *Proceedings of International Conference on Computer Analysis of Images and Patterns*, volume 4673 of *Lecture Notes in Computer Science*, pages 466–473. Springer, 2007.

[7] G.A. Atkinson and E.R. Hancock. Two-dimensional BRDF estimation from polarisation. *Computer Vision and Image Understanding*, 111(2):126–141, 2008.

[8] R. Basri, D. Jacobs, and I. Kemelmacher. Photometric stereo with general, unknown lighting. *International Journal of Computer Vision*, 72(3):239–257, 2007.

[9] P. Beckmann and A. Spizzichino. *The scattering of electromagnetic waves from rough surfaces*, volume 4. Pergamon, 1963.

[10] T. Beeler, B. Bickel, P. Beardsley, B. Sumner, and M. Gross. High-quality single-shot capture of facial geometry. *ACM Transactions on Graphics*, 29(4):40–49, 2010.

[11] P.N. Belhumeur, D.J. Kriegman, and A.L. Yuille. The bas-relief ambiguity. *International Journal of Computer Vision*, 35(1):33–44, 1999.

[12] C.A. Bennett. *Principles of Physical Optics*. Wiley, 2008.

[13] J. Besag. On the statistical analysis of dirty pictures. *Journal of the Royal Statistical Society. Series B (Methodological)*, 48(3):259–302, 1986.

[14] J.F. Blinn. Models of light reflection for computer synthesized pictures. *SIGGRAPH Computer Graphics*, 11(2):192–198, 1977.

[15] A.G. Bors, E.R. Hancock, and R.C. Wilson. Terrain analysis using radar shape-from-shading. *IEEE Transactions on Pattern Analysis and Machine Intelligence*, 25(8):974–992, 2003.

[16] A.M. Bronstein, M.M. Bronstein, M. Zibulevsky, and Y.Y. Zeevi. Sparse ICA for blind separation of transmitted and reflected images. *International Journal of Imaging Systems and Technology*, 15(1):84–91, 2005.

[17] M.J. Brooks. Surface-normals from closed paths. In *Proceedings of the 6th International Joint Conference on Artificial Intelligence*, volume 1, pages 98–101. Morgan Kaufmann Publishers Inc., 1979.

[18] M.J. Brooks. Two results concerning ambiguity in shape from shading. In *Proceedings of the National Conference on Artificial Intelligence*, volume 83, pages 36–39, 1983.

[19] M.Z. Brown, D. Burschka, and G.D. Hager. Advances in computational stereo. *IEEE Transactions on Pattern Analysis and Machine Intelligence*, 25(8):993–1008, 2003.

[20] S. Buchala, N. Davey, R.J. Frank, and T.M. Gale. Dimensionality reduction of face images for gender classification. In *Proceedings of the 2nd International IEEE Conference on Intelligent Systems*, volume 1, pages 88–93, 2004.

[21] D. Conte, P. Foggia, C. Sansone, and M. Vento. Thirty years of graph matching in pattern recognition. *International Journal of Pattern Recognition and Artificial Intelligence*, 18(3):265–298, 2004.

[22] R.L. Cook and K.E. Torrance. A reflectance model for computer graphics. *ACM Transactions on Graphics*, 1(1):7–24, 1982.

[23] T.M. Cover and J.A. Thomas. *Elements of Information Theory*. Wiley, 1991.

[24] J. de Rigal, C. Escoffier, B. Querleux, B. Faivre, P. Agache, and J.L. Lévêque. Assessment of aging of the human skin by in vivo ultrasonic imaging. *Journal of Investigative Dermatology*, 93(5):621–625, 1989.

[25] P. Debevec, T. Hawkins, C. Tchou, H.P. Duiker, W. Sarokin, and M. Sagar. Acquiring the reflectance field of a human face. In *Proceedings of the 27th Annual Conference on Computer Graphics and Interactive Techniques*, pages 145–156, July 2000.

[26] P. Deuflhard. *Newton Methods for Nonlinear Problems: Affine Invariance and Adaptive Algorithms*, volume 35. Springer Verlag, 2004.

[27] J. Dorsey, A. Edelman, H.W. Jensen, J. Legakis, and H.K. Pedersen. Modeling and rendering of weathered stone. In *Proceedings of the 26th Annual Conference on Computer Graphics and Interactive Techniques*, pages 225–234. ACM, 1999.

[28] W.T. Doyle. Scattering approach to fresnel's equations and brewster's law. *American Journal of Physics*, 53(5):463–468, 1985.

[29] O. Drbohlav and R. Sara. Using polarization to determine intrinsic surface properties. In *Proceedings of SPIE*, volume 3826, pages 253–263, 1999.

[30] C. Escoffier, J. de Rigal, A. Rochefort, R. Vasselet, J.L. Lévêque, and P.G. Agache. Age-related mechanical properties of human skin: an in vivo study. *Journal of Investigative Dermatology*, 93(3):353–357, 1989.

[31] H. Farid and E.H. Adelson. Separating reflections and lighting using independent components analysis. In *Proceedings of IEEE Conference on Computer Vision and Pattern Recognition*, volume 1, pages 262–267, 1999.

[32] T.J. Farrell, M.S. Patterson, and B. Wilson. A diffusion theory model of spatially resolved, steady-state diffuse reflectance for the noninvasive determination of tissue optical properties in vivo. *Medical Physics*, 19(4):879–888, 1992.

[33] R.W. Fleming, R.O. Dror, and E.H. Adelson. Real-world illumination and the perception of surface reflectance properties. *Journal of Vision*, 3(5):347–368, 2003.

[34] D.A. Forsyth and J. Ponce. *Computer Vision: A Modern Approach*. Prentice Hall, New York, USA, 2003.

[35] R.T. Frankot and R. Chellappa. A method for enforcing integrability in shape from shading algorithms. *IEEE Transactions on Pattern Analysis and Machine Intelligence*, 10(4):439–451, 1988.

[36] P. Gehler and S. Nowozin. On feature combination for multiclass object classification. In *Proceedings of the 12th IEEE International Conference on Computer Vision*, pages 221–228, September 2009.

[37] A.S. Georghiades, P.N. Belhumeur, and D.J. Kriegman. From few to many: Illumination cone models for face Recognition under variable lighting and pose. *IEEE Transactions on Pattern Analysis and Machine Intelligence*, 23(6):643–660, 2002.

[38] G.H. Glover, C.E. Hayes, N.J. Pelc, W.A. Edelstein, O.M. Mueller, H.R.F. Hart, C.J. Hardy, M. O'Donnell, and W.D. Barber. Comparison of linear and circular polarization for magnetic resonance imaging. *Journal of Magnetic Resonance*, 64(2):255–270, 1985.

[39] A. Graf and F. Wichmann. Gender classification of human faces. In *Proceedings of IEEE/CS International Workshops on Biologically Motivated Computer Vision*, volume 17, pages 1489–1496. Springer, 2002.

[40] H. Haneishi, T. Iwanami, T. Honma, N. Tsumura, and Y. Miyake. Goniospectral imaging of three-dimensional objects. *Journal of Imaging Science and Technology*, 45(5):451–456, 2001.

[41] R.V.L. Hartley. *Transmission of Information*, volume 7. Bell System Technical Journal, 1928.

[42] X.D. He, K.E. Torrance, F.X. Sillion, and D.P. Greenberg. A comprehensive physical model for light reflection. *SIGGRAPH Computer Graphics*, 25(4):175–186, 1991.

[43] E. Hecht. *Optics (4th edn.)*. Addison-Wesley, San Francisco, CA, 2002.

[44] D. Hill, D. Hawkes, N. Harrison, and C. Ruff. A strategy for automated multimodality image registration incorporating anatomical knowledge and imager characteristics. In *Proceedings of the 13th International Conference on Information Processing in Medical Imaging*, volume 687 of *Lecture Notes in Computer Science*, pages 182–196, June 1993.

[45] B.K.P. Horn and M.J. Brooks. *Shape from Shading*. MIT press, 1989.

[46] C.P. Huynh, A. Robles-Kelly, and E.R. Hancock. Shape and refractive index recovery from single-view polarisation images. In *Proceedings of IEEE Conference on Computer Vision and Pattern Recognition*, pages 1229–1236, June 2010.

[47] C.P. Huynh, A. Robles-Kelly, and E.R. Hancock. Shape and refractive index from single-view spectro-polarimetric images. *International Journal of Computer Vision*, 101(1):64–94, 2013.

[48] T.L. Hwang, J.J. Clark, and A.L. Yuille. A depth recovery algorithm using defocus information. In *Proceedings of IEEE Conference on Computer Vision and Pattern Recognition*, pages 476–482, June 1989.

[49] A. Hyvärinen. Survey on independent component analysis. *Neural Computing Surveys*, 2(4):94–128, 1999.

[50] A. Hyvärinen, J. Karhunen, and E. Oja. *Independent component analysis*, volume 26. Wiley-interscience, 2001.

[51] J.E. Jackson and J. Wiley. *A User's Guide to Principal Components*, volume 19. Wiley Online Library, 1991.

[52] F.A. Jenkins and H.E. White. *Fundamentals of Optics*. McGraw-Hill, 1957.

[53] H.W. Jensen, S.R. Marschner, M. Levoy, and P. Hanrahan. A practical model for subsurface light transport. In *Proceedings of the 28th Annual Conference on Computer Graphics and Interactive Techniques*, pages 511–518. ACM, 2001.

[54] C. Jutten and J. Herault. Blind separation of sources, part i: An adaptive algorithm based on neuromimetic architecture. *Signal Processing*, 24(1):1–10, 1991.

[55] P. Kisilev, M. Zibulevsky, Y.Y. Zeevi, and B.A. Pearlmutter. Multiresolution framework for blind source separation. Technical Report CCIT Report No. 317, Department of Electrical Engineering, Technion-Israel Institute of Technology, 2000.

[56] G.P. Können. *Polarized Light in Nature*. Cambridge Univ Press, 1985.

[57] K. Koshikawa. A polarimetric approach to shape understanding of glossy objects. In *Proceedings of the 6th International joint Conference on Artificial Intelligence*, volume 1, pages 493–495, 1979.

[58] P. Kovesi. Shapelets correlated with surface normals produce surfaces. In *Proceedings of International Conference on Computer Vision*, volume 2, pages 994–1001. IEEE, 2005.

[59] A. Krishnaswamy and G.V.G. Baranoski. A biophysically-based spectral model of light interaction with human skin. *Computer Graphics Forum*, 23(3):331–340, 2004.

[60] H. Li, S.C. Foo, K.E. Torrance, and S.H. Westin. Automated three-axis gonioreflectometer for computer graphics applications. In *Proceedings of SPIE*, volume 5878, pages 221–231, 2005.

[61] S. Lin and S.W. Lee. Estimation of diffuse and specular appearance. In *Proceedings of the 7th International Conference on Computer Vision*, volume 2, pages 855–861, 1999.

[62] B.G. Lindsay. *Mixture Models: Theory, Geometry, and Applications*, volume 5. Inst of Mathematical Statistic, 1995.

[63] D.G. Lowe. Distinctive image features from scale-invariant keypoints. *International Journal of Computer Vision*, 60(2):91–110, 2004.

[64] W.C. Ma, T. Hawkins, P. Peers, C.F. Chabert, M. Weiss, and P. Debevec. Rapid acquisition of specular and diffuse normal maps from polarized spherical gradient illumination. In *Proceedings of the 18th Eurographics Conference on Rendering Techniques*, pages 183–194, 2007.

[65] F. Maes, A. Collignon, D. Vandermeulen, G. Marchal, and P. Suetens. Multimodality image registration by maximization of mutual information. *IEEE Transactions on Medical Imaging*, 16(2):187–198, 1997.

[66] S. Makeig, A.J. Bell, T.P. Jung, and T.J. Sejnowski. Independent component analysis of electroencephalographic data. In *Advances in Neural Information Processing Systems(NIPS)*, volume 8, pages 145–151. MIT Press, 1996.

[67] S.R. Marschner, S.H. Westin, E.P.F. Lafortune, K.E. Torrance, and D.P. Greenberg. Image-based brdf measurement including human skin. In *Proceedings of the 10th Eurographics Workshop on Rendering Techniques*, pages 131–144. Springer, June 1999.

[68] D. Miyazaki, M. Kagesawa, and K. Ikeuchi. Transparent surface modeling from a pair of polarization images. *IEEE Transactions on Pattern Analysis and Machine Intelligence*, 26(1):73–82, 2004.

[69] D. Miyazaki, R.T. Tan, K. Hara, and K. Ikeuchi. Polarization-based inverse rendering from a single view. In *Proceedings of 9th IEEE International Conference on Computer Vision*, volume 2, pages 982–987, 2003.

[70] V. Müller. Elimination of specular surface-reflectance using polarized and unpolarized light. In *Proceedings of European Conference on Computer Vision*, volume 1065 of *Lecture Notes in Computer Science*, pages 625–635. Springer, 1996.

[71] S.K. Nayar, X.S. Fang, and T. Boult. Separation of reflection components using color and polarization. *International Journal of Computer Vision*, 21(3):163–186, 1997.

[72] A. Ngan, F. Durand, and W. Matusik. Experimental analysis of brdf models. In *Proceedings of the 16th Eurographics Conference on Rendering Techniques*, pages 117–126. Eurographics Association, 2005.

[73] F.E. Nicodemus, J.C. Richmond, J.J. Hsia, I.W. Ginsberg, and T. Limperis. Geometrical considerations and nomenclature for reflectance. In *Nbs Monograph*, volume 160, pages 1–52. National Bureau of Standards Washington, DC, October 1977.

[74] M. Oren and S.K. Nayar. Generalization of lambert's reflectance model. In *Proceedings of the 21st Annual Conference on Computer Graphics and Interactive Techniques*, pages 239–246. ACM, 1994.

[75] F.L. Pedrotti and L.S. Pedrotti. *Introduction to Optics*, volume 28. Prentice Hall, 1993.

[76] B.T. Phong. Illumination for computer generated pictures. *Communications of the ACM*, 18(6):311–317, 1975.

[77] J.P.W. Pluim, J.B.A. Maintz, and M.A. Viergever. Mutual-information-based registration of medical images: a survey. *IEEE Transactions on Medical Imaging*, 22(8):986–1004, 2003.

[78] H. Ragheb and E.R. Hancock. Highlight removal using shape-from-shading. In *Proceedings of European Conference on Computer Vision*, volume 2351 of *Lecture Notes in Computer Science*, pages 626–641. Springer, 2002.

[79] H. Ragheb and E.R. Hancock. A probabilistic framework for specular shape-from-shading. *Pattern Recognition*, 36(2):407–427, 2003.

[80] H. Ragheb and E.R. Hancock. Rough surface estimation using the kirchhoff model. In *Proceedings of the 13th Scandinavian Conference on Image Analysis*, pages 477–484. Springer-Verlag, 2003.

[81] H. Ragheb and E.R. Hancock. Surface radiance correction for shape from shading. *Pattern Recognition*, 38(10):1574–1595, 2005.

[82] H. Ragheb and E.R. Hancock. The modified beckmann-kirchhoff scattering theory for rough surface analysis. *Pattern Recognition*, 40(7):2004–2020, 2007.

[83] S. Rahmann. Reconstruction of quadrics from two polarization views. In *Proceedings of IbPRIA*, volume 2652 of *Lecture Notes in Computer Science*, pages 810–820. Springer, 2003.

[84] S. Rahmann and N. Canterakis. Reconstruction of specular surfaces using polarization imaging. In *Proceedings of IEEE Conference on Computer Vision and Pattern Recognition*, volume 1, pages 149–156, 2001.

[85] A. Rajwade, A. Banerjee, and A. Rangarajan. Probability density estimation using isocontours and isosurfaces: applications to information-theoretic image registration. *IEEE Transactions on Pattern Analysis and Machine Intelligence*, 31(3):475–491, 2009.

[86] T. Rindfleisch. Photometric method for lunar topography. *Photogrammetric Engineering*, 32(2):262–277, March 1966.

[87] D. Russakoff, C. Tomasi, T. Rohlfing, and C. Maurer. Image similarity using mutual information of regions. In *Proceedings of European Conference on Computer Vision*, volume 3023 of *Lecture Notes in Computer Science*, pages 596–607. Springer, 2004.

[88] M. Saito, Y. Sato, K. Ikeuchi, and H. Kashiwagi. Measurement of surface orientations of transparent objects by use of polarization in highlight. *Journal of the Optical Society of America*, 16(9):2286–2293, 1999.

[89] G. Saman and E.R. Hancock. Robust Computation of the polarisation image. In *Proceedings of the 10th International Conference on Pattern Recognition*, pages 971–974, 2010.

[90] G. Saman and E.R. Hancock. Refractive index estimation using polarisation and photometric stereo. In *Proceedings of International Conference on Computer Analysis of Images and Patterns*, volume 6855 of *Lecture Notes in Computer Science*, pages 548–554. Springer, 2011.

[91] Y. Sato, M.D. Wheeler, and K. Ikeuchi. Object shape and reflectance modeling from observation. In *Proceedings of the 24th Annual Conference on Computer Graphics and Interactive Techniques*, pages 379–387. ACM, 1997.

[92] J.M. Schmitt, G.X. Zhou, E.C. Walker, and R.T. Wall. Multilayer model of photon diffusion in skin. *Journal of the Optical Society of America A*, 7(11):2141–2153, 1990.

[93] S.A. Shafer. Using color to separate reflection components. *Color Research & Application*, 10(4):210–218, 1985.

[94] P.E. Shames, P.C. Sun, and Y. Fainman. Modeling of scattering and depolarizing electro-optic devices. i. characterization of lanthanum-modified lead zirconate titanate. *Applied Optics*, 37(17):3717–3725, 1998.

[95] D.F. Shanno. Conditioning of quasi-newton methods for function minimization. *Mathematics of Computation*, 24(111):647–656, 1970.

[96] C.E. Shannon. A mathematical theory of communication. *ACM SIGMOBILE Mobile Computing and Communications Review*, 5(1):3–55, 2001.

[97] J. Shotton, T. Sharp, A. Kipman, A. Fitzgibbon, M. Finocchio, A. Blake, M. Cook, and R. Moore. Real-time human pose recognition in parts from single depth images. *Communication of ACM*, 56(1):116–124, January 2013.

[98] W.A.P. Smith. *Statistical Methods for Facial Shape-from-shading and Recognition*. PhD thesis, University of York, 2007.

[99] W.A.P. Smith and E.R. Hancock. Recovering face shape and reflectance properties from single images. In *Proceedings of the 8th International Conference on Automatic Face & Gesture Recognition*, pages 1–8, September 2008.

[100] A. Spizzichino and P. Beckmann. *The Scattering of Electromagnetic Waves from Rough Surfaces*. Artech House, 1963.

[101] B.J. Super and A.C. Bovik. Planar surface orientation from texture spatial frequencies. *Pattern Recognition*, 28(5):729–743, 1995.

[102] R.T. Tan and K. Ikeuchi. Separating reflection components of textured surfaces using a single image. *IEEE Transactions on Pattern Analysis and Machine Intelligence*, 27(2):178–193, 2005.

[103] P. Terrier and V. Devlaminck. A device to classify surface orientation from polarization images. In *Proceedings of International Conference on Image Processing*, volume 2, pages 495–498. IEEE, 2000.

[104] S. Tominaga and N. Tanaka. Estimating reflection parameters from a single color image. *Computer Graphics and Applications*, 20(5):58–66, 2000.

[105] S. Tominaga and N. Tanaka. Refractive index estimation and color image rendering. *Pattern Recognition Letters*, 24(11):1703–1713, 2003.

[106] K.E. Torrance and E.M. Sparrow. Theory for off-specular reflection from roughened surfaces. *Journal of the Optical Society of America*, 57(9):1105–1112, 1967.

[107] N. Tsumura, H. Haneishi, and Y. Miyake. Independent-component analysis of skin color image. *Journal of the Optical Society of America*, 16(9):2169–2176, 1999.

[108] N. Tsumura, N. Ojima, K. Sato, M. Shiraishi, H. Shimizu, H. Nabeshima, S. Akazaki, K. Hori, and Y. Miyake. Image-based skin color and texture analysis/synthesis by extracting hemoglobin and melanin information in the skin. *ACM Transactions on Graphics*, 22(3):770–779, 2003.

[109] N. Tsumura, K. Uetsuki, N. Ojima, and Y. Miyake. Correlation map analysis between appearance of japanese facial images and amount of melanin and hemoglobin components in the skin. In *Proceedings of SPIE: Human Vision and Electronic Imaging*, volume 6, pages 252–260, 2001.

[110] S. Umeyama and G. Godin. Separation of diffuse and specular components of surface reflection by use of polarization and statistical analysis of images. *IEEE Transactions on Pattern Analysis and Machine Intelligence*, 26(5):639–647, 2004.

[111] P. Viola and W.M. Wells III. Alignment by maximization of mutual information. *International Journal of Computer vision*, 24(2):137–154, 1997.

[112] G.J. Ward. Measuring and modeling anisotropic reflection. In *Proceedings of the 19th Annual Conference on Computer Graphics and Interactive Techniques*, pages 265–272. ACM New York, NY, USA, 1992.

[113] S.H. Westin and Torrance K.E. A field guide to brdf models. Technical Report PCG-04-01, Program of Computer Graphics, Cornell University, January 2004.

[114] T. Weyrich, W. Matusik, H. Pfister, B. Bickel, C. Donner, C. Tu, J. McAndless, J. Lee, A. Ngan, H.W. Jensen, et al. Analysis of human faces using a measurement-based skin reflectance model. *ACM Transactions on Graphics*, 25(3):1013–1024, 2006.

[115] L.B. Wolff. Surface orientation from two camera stereo with polarizers. In *Proceedings of SPIE Conf. Optics, Illumination, Image Sensing for Machine Vision IV*, volume 1194, pages 287–297, 1989.

[116] L.B. Wolff. Polarization vision: a new sensory approach to image understanding. *Image and Vision Computing*, 15(2):81–93, 1997.

[117] L.B. Wolff and T.E. Boult. Constraining object features using a polarization reflectance model. *IEEE Transactions on Pattern Analysis and Machine Intelligence*, 13(7):635–657, 1991.

[118] R.P. Woods, S.R. Cherry, J.C. Mazziotta, et al. Rapid automated algorithm for aligning and reslicing pet images. *Journal of Computer Assisted Tomography*, 16(4):620, 1992.

[119] P.L. Worthington and E.R. Hancock. New constraints on data-closeness and needle map consistency for shape-from-shading. *IEEE Transactions on Pattern Analysis and Machine Intelligence*, 21(12):1250–1267, 2002.

[120] J. Wu, W.A.P. Smith, and E.R. Hancock. Gender discriminating models from facial surface normals. *Pattern Recognition*, 44(12):2871–2886, 2011.

[121] T.P. Wu and C.K. Tang. Separating specular, diffuse, and subsurface scattering reflectances from photometric images. In *Proceedings of European Conference on Computer Vision*, volume 3022 of *Lecture Notes in Computer Science*, pages 419–433. Springer, 2004.

[122] T.P. Wu, K.L. Tang, C.K. Tang, and T.T. Wong. Dense photometric stereo: A markov random field approach. *IEEE Transactions on Pattern Analysis and Machine Intelligence*, 28(11):1830–1846, 2006.

[123] L. Zhang and E.R. Hancock. Robust shape and polarisation estimation using blind source separation. In *Proceedings of International Conference on Computer Analysis of Images and Patterns*, volume 6854, pages 178–185. Springer, 2011.

[124] L. Zhang and E.R. Hancock. Robust estimation of shape and polarisation using blind source separation. *Pattern Recognition Letters*, 34(8):856–862, March 2013.

[125] L. Zhang, E.R. Hancock, and J. Wu. Estimating surface characteristics and extracting features from polarisation. In *Proceedings of Joint IAPR International Workshop, SSPR & SPR*, volume 7626 of *Lecture Notes in Computer Science*, pages 400–408, 2012.

[126] Q. Zheng and R. Chellappa. Estimation of illuminant direction, albedo, and shape from shading. *IEEE Transactions on Pattern Analysis and Machine Intelligence*, 13(7):680–702, 2002.